ULTRASOUND CONTRAST AGENTS

RESONANCES OF COATED BUBBLES

Samenstelling promotiecommissie

Prof. dr. ir. L. van Wijngaarden, voorzitter	Universiteit Twente, TNW
Prof. dr. rer. nat. D. Lohse, promotor	Universiteit Twente, TNW
Prof. dr. ir. N. de Jong, promotor	Universiteit Twente, TNW
Dr. A.M. Versluis, assistent-promotor	Universiteit Twente, TNW
Prof. dr. C.A. van Blitterswijk	Universiteit Twente, TNW
Dr. ir. M.R. Böhmer	Philips Research
Prof. dr. ir. N. Bom	Erasmus MC
Prof. dr. A.G.J.M. van Leeuwen	Universiteit Twente, TNW

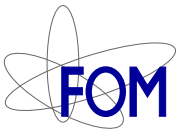

The research described in this thesis is part of the research program of the "Stichting voor Fundamenteel Onderzoek der Materie" (FOM), which is financially supported by the "Nederlandse Organisatie voor Wetenschappelijk Onderzoek" (NWO). It was carried out at the Physics of Fluids research group of the faculty of Science and Technology of the University of Twente.

Nederlandse titel:
Ultrageluid contrast vloeistoffen — Resonanties van gecoate bellen

Publisher:
Sander van der Meer, Physics of Fluids, University of Twente,
P.O. Box 217, 7500 AE Enschede, The Netherlands
http://pof.tnw.utwente.nl

Cover design: Sander van der Meer
Print: Gildeprint B.V., Enschede

ISBN: 978-90-365-2548-0

ULTRASOUND CONTRAST AGENTS

RESONANCES OF COATED BUBBLES

PROEFSCHRIFT

ter verkrijging van
de graad van doctor aan de Universiteit Twente,
op gezag van de rector magnificus,
prof. dr. W. H. M. Zijm,
volgens besluit van het College voor Promoties
in het openbaar te verdedigen
op donderdag 13 september 2007 om 15.00 uur

door

Sander Martijn van der Meer

geboren op 11 januari 1978

te Assen

Dit proefschrift is goedgekeurd door de promotoren:

prof. dr. rer. nat. Detlef Lohse
prof. dr. ir. Nico de Jong

en de assistent-promotor:

dr. Michel Versluis

Contents

1 Introduction

1.1 Historic overview of ultrasound imaging

Robert Hooke (1635–1703), the eminent English scientist responsible for the theory of elasticity, foresaw the use of sound for diagnosis when he wrote [1]:

> *"It may be possible to discover the motions of the internal parts of bodies, whether animal, vegetable, or mineral, by the sound they make; that one may discover the works performed in the several offices and shops of a man's body, and thereby discover what instrument of engine is out of order, what works are going on at several times, and lie still at others, and the like."*

The key principle of diagnostic ultrasound imaging is the use of echo–location. Echo–location is the use of reflections of sound to locate objects. Many animals in the natural world, such as bats (see Fig. 1.1) and dolphins, use this principle. In 1794 L. Spallanzani investigated this principle by observing the movements of bats in the dark. He theorized that they detected obstacles using sound waves rather than light. The connection between echo–location and the medial application of sound, however, was not made until the science of underwater exploration matured.

Figure 1.1: Echo location by animals

The beginnings of sonar and ultrasound for medical imaging can be traced to the sinking of the Titanic. Within a month of the Titanic tragedy, British scientist L.F. Richardson [3] filed patents to detect icebergs with underwater echo ranging. But in 1913, there were no practical ways to

implement his ideas. However, the discovery of piezoelectricity (the property by which electrical charge is created by the mechanical deformation of a crystal) by the Curie brothers in 1880 and the invention of the triode amplifier tube by Lee De Forest in 1907 set the stage for further advances in pulse–echo range measurement. The Curie brothers also showed that the reverse piezoelectric effect (voltages applied to certain crystals cause them to deform) could be used to transform piezoelectric materials into resonating transducers.

By the end of World War I, C. Chilowsky and P. Langevin [4] took the technologies to realize practical echo ranging in the water. Their high–power echo–ranging systems were successfully used to detect submarines. During transmissions however, they observed schools of dead fish that floated to the water surface. Langevin also observed that pain was induced in the hand, when it was placed inside a water tank that was insonated with the high–intensity ultrasound. This shows that scientists were aware of the potential for ultrasound–induced bioeffects from the early days of ultrasound research [5].

After World War II, with sonar and radars as models, a few medical practitioners saw the possibilities of using pulse–echo techniques to probe the human body for medical purposes. In the 1950s a single piezoelectric crystal was first employed in contact with skin to launch an acoustic wave into human tissue. The wave consisted of several cycles at a frequency of 20 kHz, beyond the capacity of human hearing. A series of reflections returned to the crystal at different times because of mismatches of acoustic impedance (density $\times$ sound speed) between organs and bone.

The 1960s saw the development of commercial ultrasound systems that exploited the mass production of cathode–ray tubes. Widespread use of ultrasound followed.

Modern ultrasound scanners use the linear superposition of spherical or cylindrical wavefronts of tiny piezoelectric crystals. Those crystals are arrayed to produce waveforms that can be steered or focused based upon the timing of the crystal's excitations.

1.2 Ultrasound imaging

Medical ultrasound (US) imaging is based on transmitting and receiving sound waves with frequencies ranging from 1–50 MHz. The waves are generated by a transducer consisting of piezo–electric crystals which

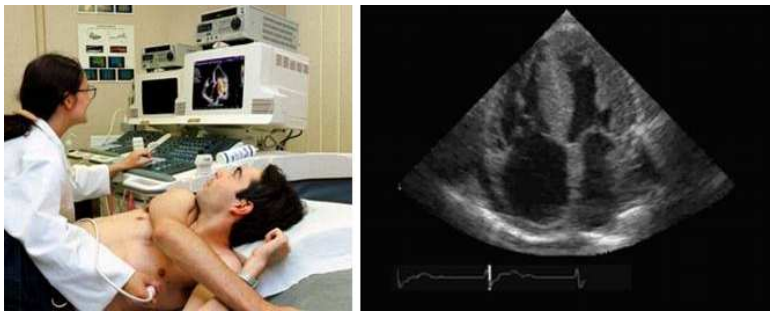

Figure 1.2: Echocardiography being performed in a hospital (left). A typical echocardiogram (right).

convert electric signals into ultrasonic pulses [6]. The transmitted waves propagate through a medium until they hit reflecting or scattering objects, and the reflected waves are received by the same transducer. The time between transmission and reception is directly related to the distance from the source to the reflecting object by the assumption that the speed of propagation is constant in the medium. Ultrasound can travel through water and soft tissue, and is therefore a suitable technique for non–invasive imaging of structures inside the human body (see Fig. 1.2 for a cardiogram).

The scatter and reflection of sound from inhomogeneities in the tissue [7] are being exploited in ultrasound imaging. The scatter from blood however is much weaker than the scatter from tissue. To increase the scattering properties from the blood pool, an ultrasound contrast agent (UCA) is introduced in the blood.

1.3 Ultrasound contrast agents

Ultrasound contrast agents were proposed nearly four decades ago, when it was accidentally discovered that air bubbles could be detected in the bloodstream after injections of agitated aqueous solutions [8]. An UCA is a liquid, containing small encapsulated microbubbles, which very efficiently scatter ultrasound [9–11] (see Fig. 1.3 for a scanning electron microscopy picture and an optical microscopy picture). In this way, it is possible to visualize and quantify the perfusion of tissue, like for instance the heart muscle, liver or kidney.

The commercial development of contrast agents began in the 1980s

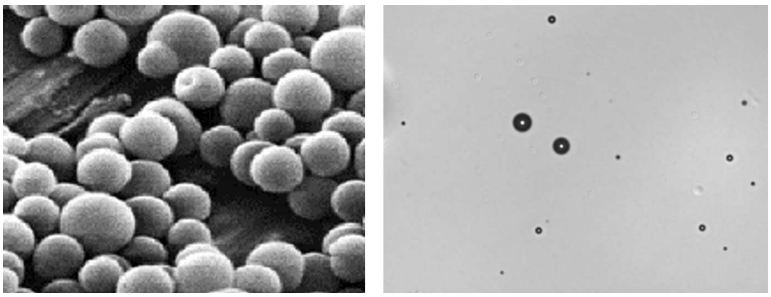

Figure 1.3: A scanning electron microscopy picture of contrast bubbles (left). A typical optical microscopy picture of contrast bubbles in a solution (right).

with observations that led to the stabilization and miniaturization of the microbubble. Carroll *et al.* [12] demonstrated that gelatin–encapsulated nitrogen bubbles were stable enough to be used for US enhancement. Then, Feinstein *et al.* [13] showed that microbubbles sonicated from human serum albumin were small and stable enough to traverse the pulmonary circulation and to opacify the left ventricle. These findings led to significant interest in the development of a commercially available US contrast agent by pharmaceutical companies. Several programs were initiated to develop an easy to use and clinically useful contrast agent for ultrasound. Schering AG (Berlin, Germany) was the first company to be successful. Their first agent was Echovist® (1982), which enabled enhancement of the right ventricle only, followed by Levovist® (1985), which achieved enhancement of the left ventricle. Schering's agents are approved in Europe, Japan and Canada. Molecular Biosystems Inc. (MBI; San Diego, CA) developed Albunex®, the first agent approved by the US Food and Drug Administration (FDA) in 1994 for USA distribution. The agent was based on technology utilizing sonicated human serum albumin to encapsulate and stabilize the air microbubble. Both Albunex® and Levovist® utilize air as the gas component of the microbubble. This resulted in reduced longevity in vivo and limited the commercial success of these agents.

The use of various types of perfluorocarbon (PFC) gas to increase the persistence of the microbubble was first introduced in the early 1990s. Many agents under development incorporated PFC technology into their formulations. These products include reformulation of the Albunex® technology utilizing a PFC gas. This product was named Optison® (MBI). Additional agents have been developed that utilize PFC

gas and vary the constituents in the shell that encapsulate the gas, like Definity® (2001) distributed by Bristol Myers Squibb (New York, NY) and Imagent® (2002), distributed by IMCOR (IMCOR, San Diego, CA), a division of Photogen Technologies Inc. Another agent, SonoVue® (Bracco International B.V., Amsterdam, The Netherlands), utilizes sulfur hexafluoride, a low–solubility fluorinated gas. These development activities have resulted in smaller, more stable microbubble agents, which, coupled with improvements in ultrasound equipment technology, have resulted in the extension of contrast enhancement from cavity opacification to perfusion.

To summarize, contrast agents are nowadays used in various medical investigations, e.g. in obtaining diagnostic information from the volume, shape and movement of the heart ventricles, or to quantify the perfusion of various organs, like liver or kidney.

In general, the microbubbles consist of air or an inert gas and they are coated with a protein, lipid or polymer layer. This prevents the bubbles to either dissolve in the blood or to coalesce to form larger bubbles. When subjected to ultrasound a microbubble will start to oscillate at the frequency of the ultrasound. At higher ultrasound intensity the oscillations become more extreme and nonlinear behavior will start to appear. The bubble will produce higher harmonics (e.g. at twice or three times the fundamental frequency). It could also become unstable and could collapse. These interesting effects are tested and implemented in new diagnostic and therapeutic ultrasound applications.

The fundamental understanding of the dynamics of contrast bubbles is a field of ongoing research. For example, the quantification of the response of contrast bubbles to ultrasound is an important research aspect. Until now, bubbles are characterized mainly by studying acoustically a representative sample of the UCA, containing many microbubbles [14–16]. From this data the overall resonance behavior of the sample can be deduced. Ideal contrast agents would be monodisperse in size, but in practice they have a size distribution which can be measured with, e.g., a Coulter counter, resulting in a mean size and size range [17]. For SonoVue® and also for BR-14 (Bracco Research S.A., Geneva, Switzerland), e.g., the mean radius is 1.5 μm, with 95% of the bubbles smaller than 5 μm. The polydispersity of the microbubbles makes it difficult to extract information on the physical properties of single bubbles, since the acoustical response of a bubble strongly depends on its size [17]. Furthermore, the acoustic pressure signal emitted by the bubbles is distorted by frequency–dependent scattering and attenuation. On the other hand,

measuring the acoustic response of a single individual contrast bubble is a complicated task [18]. First, it is difficult to isolate a single bubble in the focal region of a transducer, which would require at least 1 mm of distance between the bubbles. Second, extracting the absolute pressure emitted by the bubble from the measured response requires an accurate calibration of the transducer transfer function.

1.4 Imaging

To overcome the difficulties associated with acoustical characterization, optical methods have been proposed [19–23]. Such methods are based on the direct measurement of the bubble radius, which, unlike the acoustical response, is not subject to distortion and in principle does not require difficult calibration. Furthermore, the interaction between bubbles (secondary Bjerknes forces) decays as the inverse square of their distance, fast enough to consider different bubbles to oscillate independently as soon as they are separated by a few (roughly ten) bubble radii. Isolating the response of a single bubble optically is thus less constraining than for acoustical measurements. However, optical methods exhibit other drawbacks: very high frame rates are required to resolve microbubble oscillations at several MHz, and the resolution is limited, since the microbubble size is just a little higher than the optical resolution.

Cameras that record at these high speeds exist, however their recording capability is limited to a total number of 8 frames only. The ultrasound typically lasts for 10 cycles during which the response of the microbubbles can be highly non–linear. The number of frames should be sufficient to record the complete bubble response, therefore, more than 100 frames are desirable.

Rotating mirror cameras produce frame records up to 25 million frames per second. They record up to 130 frames on a negative film track. The exposed image is relayed to the film by associated lenses and a fast rotating mirror (1.2 million rpm). The most important disadvantage of using negative film is its poor light sensitivity which is limited to 3200 ASA, highly insufficient for the short exposure times in our microscopic application.

1.5 Brandaris 128

The Physics of Fluids group of the University of Twente and the Biomedical Engineering group of the Erasmus MC have constructed a digital camera system [24]. The negative film track of the rotating mirror camera was replaced by highly sensitive CCD cameras, and an ultra high–speed camera is constructed that records 128 digital frames at a speed of up to 25 million frames per second (40 nanoseconds interframe time). This way it is possible to capture the dynamics of oscillating contrast bubbles.

The sweeping light beam within a rotating mirror camera resembles that of the optical principle of a light house, therefore the camera Brandaris 128 was named after the Netherlands' most famous lighthouse on the island of Terschelling (see Fig. 1.4).

Figure 1.4: The Brandaris light house on the island of Terschelling, The Netherlands, which was built in 1594.

Brandaris 128, illustrated in Fig. 1.5, is developed upon the Cordin 119 (Cordin Scientific Imaging, Salt Lake City, Utah) camera frame. The system combines the flexibility and sensitivity of electronic CCD detectors with the high frame rate and high number of frames available in rotating mirror cameras. In front of the camera different lenses can be mounted to suit the needs of the experiment, for example, Fig. 1.5 shows a high resolution microscope mounted. Generally, a suitable field lens is needed to couple the objective to the Brandaris. A set of relay lenses projects an image of the target subject onto a mirror prism. A gas turbine spins the three–faced mirror prism at high speed and redirects the incoming light through a lens bank to the CCD detectors. The maximum turbine speed is 20 000 rotations per second, resulting in a frame rate of 25 Mfps. The image is recorded on 128 un–intensified high sensitivity CCD chips mounted on an image arc. Thirty–two CCD Controller Cards (C3) control the 128 CCDs and transfer the images to a personal computer (PC) via standard universal serial bus (USB) hubs. The C3 hosts buffer memory that allows six full recordings to be stored on board. An infrared laser photodiode pair mounted at 30° below the optical axis generates three mirror pulses per prism rotation. The mirror pulses provide accurate measurement of the instantaneous mirror rotation rate. A mass flow controller (MFC), itself controlled by a PC via a flow and timing controller,

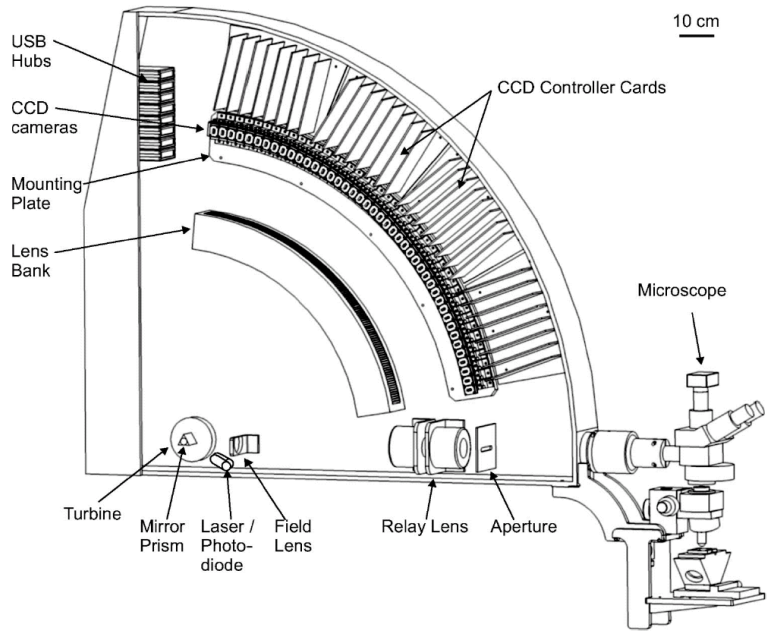

Figure 1.5: A schematic view of the interior of the Brandaris 128 high speed camera

regulates the gas flow (in general, helium is used) to the turbine and thereby determines the mirror rotation speed and thus imaging frame rate. The mirror pulses are also used as a master to control the experiment including the timing of the CCDs and the flash illumination source. The camera frame is filled with helium to minimize drag on the rotating mirror.

The six memory places of the 128 CCDs allow 768 images to be recorded in a single run. When the camera is operated in a segmented mode, these 768 images can be reorganized as required. For instance, instead of six movies of 128 frames, we can also record twelve movies of 64 frames, or twenty–four movies of 32 frames. The segmented mode principle is used in the experiments described in Ch. 3.

The Brandaris high speed camera makes it possible to study dynamics of oscillating bubbles. It also enables studies of bubble–wall interaction, bubble–bubble interaction and bubble–cell interaction. It was also used to study cavitation bubbles, bubbles in ink channels in printheads, and jetting bubbles.

The work presented here focusses on the response of contrast bubbles to ultrasound. A bubble responds differently if it is insonified with

frequencies lower than, at, or above the resonance frequency. Therefore, the resonance frequency of a contrast bubble plays a big role in the response.

1.6 Resonance

Resonance is a very common phenomenon which occurs in many types of physical systems. A familiar example is pushing a child on a swing. You can make the swing go higher and higher with relatively little effort if you time your push just right. The swing has a natural frequency of vibration and pushing "just right" means you are putting energy into it at a frequency known as the resonance frequency. The system is said to be in resonance and the amplitude of the motion increases rapidly.

There are also many examples of resonance in every day life. There is acoustic resonance in musical instruments, resonance in electrical circuits, but also large buildings or bridges can, if carelessly designed, oscillate in resonance.

1.7 Guide through the thesis

Since echoscopy using ultrasound contrast agents is a relatively new field, many improvements are still achieved in imaging and detection. The key to improving and optimizing is to fundamentally understand the bubble dynamics.

A first step to understanding the behavior of the coated microbubbles, is to set up a model which describes the dynamics of the microbubbles. Over the years, several theoretical models have been proposed. First of all, in 1917, Lord Rayleigh [25] studied cavitation bubbles around ship propellers. Minnaert [26] in 1933 performed a theoretical study of the sound emission of bubbles. Combined with some experiments, he explained the characteristic resonance frequency. In the early 1950s Plesset [27] and Noltingk [28] and Neppiras [29] introduced more sophisticated models for oscillating bubbles, followed by refinements in the late 1950s (Keller [30], Gilmore [31], Herring [32], Trilling [33]) and the 1980s by Keller and Miksis [34] and Prosperetti [35]. Encapsulated microbubbles were first modeled by De Jong *et al.* [36] in 1992 and De Jong and Hoff [37] in 1993, incorporating experimentally determined elasticity and friction parameters into the Rayleigh–Plesset model. Church [38] used linear

visco–elastic constitutive equations to describe the shell. In Ch. 2 a new model is introduced. In this model an effective surface tension was introduced which depends on the bubble radius, incorporating the effect of the phospholipidic monolayer coating of contrast agents.

The Brandaris 128 high speed camera enables optical recording of the dynamics of ultrasound contrast agents. Analyzing the behavior of individual contrast agents under influence of ultrasound is therefore also a completely new possibility. Some general properties of contrast agents are the resonance frequency, shell damping and shell viscosity. A method to measure these properties, termed microbubble spectroscopy, was developed and the results of this study are reported in Ch.3.

Both coated microbubbles and free microbubbles can start to oscillate non–spherically. The non–spherical behavior starts as a parametric instability which grows over time. After a few oscillation cycles, surface mode oscillations can appear. The results of a study of free microbubbles are described in Ch. 4. The behavior of coated bubbles is reported in Ch. 5.

At higher oscillation amplitudes, the frequency with maximum oscillation amplitude appeared to decrease. This shift of the peak frequency away from the eigenfrequency of the bubble, was investigated in Ch. 6 by introducing a new fast method that derived this peak frequency. The method used chirp frequency sweeps, allowing the method to characterize the bubble even faster than with microbubble spectroscopy. It was also observed that a bubble behaves differently to a chirp up sweep and a chirp down sweep, which is of potential interest for contrast imaging techniques.

Finally, all conclusions of the thesis are summarized in Ch. 7.

References

[1] J. TYNDALL, *Sound*, London: Longmans, Green and Co., (1875).

[2] R. EISENBERG, *Radiology: an illustrated history*, St. Louis: Mosby, (1992).

[3] L. F. RICHARDSON, British Patent No. 12, Filed May 10, 1912, issued March 27, 1913.

[4] P. BIQUARD, "Paul Langevin", Ultrasonics **10**, 213–214 (1972).

[5] W. D. O'BRIEN, "Assessing the risks for modern diagnostic ultrasound imaging", Jap. J. of Appl. Phys. **37**(1), 2781–2788 (1998).

[6] P. N. T. WELLS, *Biomedical Ultrasonics*. London: Academic Press, (1977).

[7] T. SZABO, *Diagnostic Ultrasound Imaging: Inside Out*, London: Academic Press (2004).

[8] R. GRAMIAK, P. SHAH, D. KRAMER, "Ultrasound cardiography: contrast studies in anatomy and function", Radiology **92**(5), 939–948 (1969).

[9] N. DE JONG, *Acoustic properties of ultrasound contrast agents*, Ph.D thesis, Erasmus University Rotterdam (1993).

[10] L. HOFF, *Acoustic Characterization of Contrast Agents for Medical Ultrasound Imaging*, Kluwer Academic Publishers, Dordrecht (2001).

[11] A. L. KLIBANOV, "Ultrasound contrast agents: Development of the field and current status", Top. Curr. Chem. **222**, 73–106 (2002).

[12] B. A. CARROLL, R. J. TURNER, E. G. TICKNER, D. B. BOYLE, S. W. YOUNG, "Gelatin encapsulated nitrogen microbubbles as ultrasonic contrast agents", Invest. Radiol. **15**, 260–266, (1980).

[13] S. B. FEINSTEIN, P. M. SHAH, R. J. BING, S. MEERBAUM, E. CORDAY, B. L. CHANG, G. SANTILLAN, Y. FUJIBAYASHI, Microbubble dynamics visualized in the intact capillary circulation, J. Am. Coll. Cardiol. **4**, 595–600, (1984).

[14] P. J. A. FRINKING, N. DE JONG, "Acoustic modeling of shell-encapsulated gas bubbles", Ultras. Med. Biol. **24**(4), 523–533 (1998).

[15] P. J. A. FRINKING, N. DE JONG, E. I. CÉSPEDES, "Scattering properties of encapsulated gas bubbles at high ultrasound pressures", J. Acoust. Soc. Am. **105**(3), 1989–1996 (1999).

[16] W. T. SHI, F. FORSBERG, "Ultrasonic characterization of the nonlinear properties of contrast microbubbles", Ultrasound Med. Biol. **26**, 93–104 (2000).

[17] J. M. GORCE, M. ARDITI, M. SCHNEIDER, "Influence of bubble size distribution on the echogenicity of ultrasound contrast agents. A study of SonoVue(TM)", Investigative Radiology **35**(11), 661–671 (2000).

[18] S. H. BLOCH, R. E. SHORT, K. W. FERRARA, E. R. WISNER, "The effect of size on the acoustic response of polymer-shelled contrast agents", Ultrasound Med. Biol. **31**, 439–444 (2005).

[19] J. E. CHOMAS, P. A. DAYTON, D. MAY, J. ALLEN, A. L. KLIBANOV, K. W. FERRARA, "Optical observation of contrast agent destruction", Appl. Phys. Lett. **77**, 1056–1058 (2000).

[20] N. DE JONG, P. J. A. FRINKING, A. BOUAKAZ, M. GOORDEN, T. SCHOURMANS, J. P. XU, F. MASTIK, "Optical imaging of contrast agent microbubbles in an ultrasound field with a 100-MHz camera", Ultrasound Med. Biol. **26**, 487–492 (2000).

[21] Y. SUN, D. E. KRUSE, P. A. DAYTON, K. W. FERRARA, "High-frequency dynamics of ultrasound contrast agents", IEEE Trans. Ultrason. Ferroelec. Freq. Contr. **52**, 1981–1991 (2005).

[22] K. E. MORGAN, J. S. ALLEN, P. A. DAYTON, J. E. CHOMAS, A. L. KLIBANOV, K. W. FERRARA, "Experimental and Theoretical Evaluation of Microbubble Behavior: Effect of Transmitted Phase and Bubble Size", IEEE Trans. Ultrason. Ferroelectr. Freq. Control **47**, 1494–1508 (2000).

[23] P. A. DAYTON, J. S. ALLEN, K. W. FERRARA, "The magnitude of radiation force on ultrasound contrast agents", J. Acoust. Soc. Am. **112**, 2183–2192 (2002).

[24] C. T. CHIN, C. LANCÉE, J. BORSBOOM, F. MASTIK, M. E. FRIJLINK, N. DE JONG, M. VERSLUIS, D. LOHSE, "Brandaris 128: A digital 25 million frames per second camera with 128 highly sensitive frames", Rev. Sci. Instrum., **74**(12), 5026–5034 (2003).

[25] LORD RAYLEIGH, "On the pressure developed in a liquid during the collapse of a spherical cavity", Phil. Mag. **34**, 94–98 (1917).

[26] M. MINNAERT, "On musical air-bubbles and the sounds of running water", Phil. Mag. **16**, 235–248 (1933).

[27] M.S. PLESSET, "The dynamics of cavitation bubbles", J. Appl. Mech. **16**, 277–282 (1949).

[28] B.E. NOLTINGK, E.A. NEPPIRAS, "Cavitation produced by ultrasonics", Proc. Phys. Soc. **B63**, 674–685 (1950).

[29] E.A. NEPPIRAS, B.E. NOLTINGK, "Cavitation produced by ultrasonics: theoretical conditions for the onset of cavitation", Proc. Phys. Soc. **B64**, 1032–1038 (1951).

[30] J.B. KELLER AND I.I. KOLODNER, J. Appl. Phys. **27**, 1152 (1956).

[31] F.R. GILMORE, "The growth or collapse of a spherical bubble in a viscous compressible liquid", Hydrodynamics Laboratory Report **26–4**, California Institute of Technology (1952).

[32] C. HERRING, "Theory of the pulsations of the gas bubble produced by an underwater explosion", OSRD Rep. No. **236** (1941).

[33] L. TRILLING, "The collapse and rebound of a gas bubble", J. Appl. Phys. **23**, 14 (1952).

[34] J. B. KELLER, M. MIKSIS, "Bubble oscillations of large amplitude", J. Acoust. Soc. Am. **68**(2), 628–633 (1980).

[35] A. PROSPERETTI, L.A. CRUM, K.W. COMMANDER, "Nonlinear bubble dynamics", J. Acoust. Soc. Am. **83**, 502–514, (1986).

[36] N. DE JONG, L. HOFF, T. SKOTLAND, N. BOM, "Absorption and scatter of encapsulated gas filled microspheres: theoretical considerations and some measurements", Ultrasonics **30**, 95–103, (1992).

[37] N. DE JONG, L. HOFF, "Ultrasound scattering properties of Albunex microspheres", Ultrasonics **31**(3), 75–181, (1993).

[38] C. C. CHURCH, "The effects of an elastic solid surface layer on the radial pulsations of gas bubbles", J. Acoust. Soc. Am. **97**, 1510–1521, (1995).

2

A model for large amplitude oscillations of coated bubbles accounting for buckling and rupture[§]

We present a model applicable to ultrasound contrast agent bubbles that takes into account the physical properties of a lipid monolayer coating on a gas microbubble. Three parameters describe the properties of the shell: a buckling radius, the compressibility of the shell and a break-up shell tension. The model presents an original non-linear behavior at large amplitude oscillations, termed compression-only, induced by the buckling of the lipid monolayer. This prediction is validated by experimental recordings with the high-speed camera Brandaris 128, operated at several millions of frames per second. The effect of aging, or the resultant of repeated acoustic pressure pulses on bubbles, is predicted by the model. It corrects a flaw in the shell elasticity term previously used in the dynamical equation for coated bubbles. The break-up is modeled by a critical shell tension above which gas is directly exposed to water.

2.1 Introduction

To enhance ultrasound echographic imaging, micrometer sized coated bubbles are used as contrast agents. Coating materials include lipid monolayers, polymer shells, or thick solid shells. The coating stabilizes the bubbles and prevents their coalescence. Pulmonary alveoli in the lungs have a lipidic coating for the same reason [1]. The coating modifies

[§]Based on: Philippe Marmottant, Sander van der Meer, Marcia Emmer, Michel Versluis, Nico de Jong, Sascha Hilgenfeldt, Detlef Lohse, "A model for large amplitude oscillations of coated bubbles accounting for buckling and rupture", J. Acoust. Soc. Am. **118**(6), 3499-3505 (2005)

the effective surface tension. Since surface tension plays a crucial role in the dynamics of small bubbles, when the capillary pressure term is of the order of the static ambient pressure, the coating is expected to strongly influence the dynamics.

All current models developed to describe coated bubble oscillations implicitly assume small deformations of the bubble surface: however, in practice, insonifying contrast agent bubbles produces oscillations with large variations in the surface area. We will present in this manuscript a model designed to incorporate the effect of a coating on the microbubble response to ultrasound, and to specifically capture the high-amplitude dynamics.

We focus on phospholipidic monolayer coatings, used in several contrast agent bubbles [2]. The phospholipid molecules naturally adsorb to the interface [3] and shield the water from the air, reducing the surface tension σ to a value lower than that of pure water (73 mN/m). Surface tension can be measured in a flat monolayer with the Langmuir-Blodgett balance, or on centimeter sized bubbles [4], showing its dependence on the surface concentration of molecules.

The compression of the monolayer decreases the area available per molecule. When this area reaches that covered by the lipid molecules (typically 0.4 nm^2 for phospholipids in the trans configuration normal to the interface), the effective surface tension decreases sharply, see Fig. 2.1. The variation of surface tension with the area A is expressed with the elastic compression modulus defined by $\chi = A\frac{d\sigma}{dA}$ (of order 0.2 N/m for a slow compression, as derived from the steepest slopes of Fig. 2.1). Further compression leads to an unstable situation where the monolayer buckles out of plane, while the surface tension nearly vanishes. A spectacular demonstration of the buckling is the appearance of wrinkles on coated bubbles when their gas dissolves out [8]. Buckling can be reversible [9, 10]. Vanishing surface tensions were revealed by the microscopic observation of bubbles with a monolayer lipid coating in a solid state: these bubbles could assume a steady non spherical shape [11] when deformed with a micropipette, and dissolution was greatly reduced by the absence of the capillary overpressure [12].

In contrast, a slow expansion separates molecules from each other: surface tension rises. A monolayer made from pure lipid (one species only) will show phase changes from a 2D solid state, to a liquid and eventually gaseous state, where surface tension is close to that of water. With a mixture of lipid molecules the phase changes are not necessarily present, and a 2D solid can rupture during expansion, leaving rafts of solid

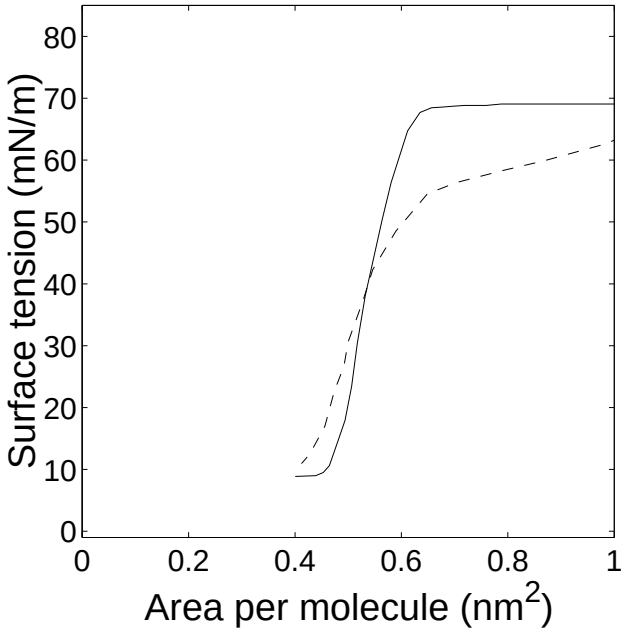

Figure 2.1: Effective surface tension versus area per molecule at the interface for two phopholipids (both present in the contrast agent SonoVue® [5]) under slow compression *at a few % per minute: distearoylphosphatidylcholine (DSPC), solid line; and dipalmytoylphosphatidylglycerol (DPPG), broken line. Curves redrawn from [6, 7].*

phospholipid molecules separated by clean interfaces [13].

Most previous existing experimental data on phospholipidic monolayers were collected at very slow compression/expansion rates, when molecules at the interface could equilibrate. Only a few experiments tackled the high-frequency and thus out-of equilibrium trends: the buckling surface tension comes closer to zero and the elastic modulus becomes higher (see reported experiments [1] with pulmonary surfactant compressed within 0.2s). These findings give some hint to the extrapolation of surface properties to the realm of high frequency oscillations, the one we are going to explore with oscillating contrast agent bubbles.

2.2 Model

2.2.1 Effective surface tension of a bubble during its oscillation

At high frequencies, we propose to model the effective surface tension σ of the lipidic monolayer of a bubble along three linear regimes inspired by the low frequency observations. The regimes depend on the bubble area $A = 4\pi R^2$, with R the bubble radius (see Fig. 2.2). This simplified model is designed to capture the coated bubble dynamics with a minimum of parameters.

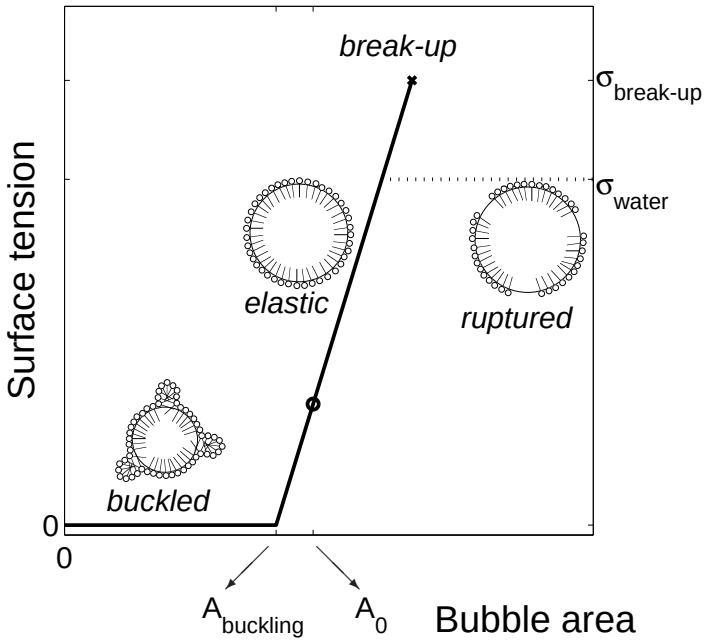

Figure 2.2: Model for the dynamic surface tension of a monolayer coated bubble (continuous line). The coating has a fixed number of lipid molecules, which corresponds to a monolayer at equilibrium (when area is A_0). The tension saturates to the water value σ_{water} (broken line) after the break-up tension has been reached ($\sigma_{\text{break-up}} > \sigma_{\text{water}}$, see main text).

The model has three parameters only to describe the surface tension: the buckling area of the bubble A_{buckling} below which the surface buckles,

an elastic modulus χ that gives the slope of the elastic regime. The third parameter is incorporated to describe the moment of rupture: the elastic regime holds until a critical break-up tension called $\sigma_{\text{break-up}}$. When this limit has been reached the maximum surface tension saturates at σ_{water}.

We motivate here the modeling of the three states:

- Buckled state, $\sigma = 0$.
  Consistent with experimental findings on the fast compression of pulmonary phospholipid monolayers, we assume a near vanishing surface tension in the buckled state [1]. The buckling area of the bubble depends on the number n of lipid molecules at the interface and on the molecular area at buckling a_{buckling}, with $A_{\text{buckling}} = n\, a_{\text{buckling}}$, with a_{buckling} typically of the order of 0.4 nm^2, see previous section. Note that a first compression of the bubble might *expel* in bulk some molecules into the bulk [14], decreasing the number n. After this transient expulsion, and for moderate driving amplitudes and short exposures, we expect the number of molecules to remain constant, as phospholipids with long carbon chains are poorly soluble.

- Elastic state, $\sigma = \chi\left(\frac{A}{A_{\text{buckling}}} - 1\right)$.
  The shell is elastic only in a narrow area range. The lower limit is A_{buckling} for the area, or equivalently R_{buckling} for the radius. The upper limit radius is fixed by the maximum surface tension, which is $\sigma_{\text{break-up}}$ before rupture of the shell giving $R_{\text{break-up}} = R_{\text{buckling}}(1 + \sigma_{\text{break-up}}/\chi)^{1/2}$, or σ_{water} after rupture giving $R_{\text{ruptured}} = R_{\text{buckling}}(1 + \sigma_{\text{water}}/\chi)^{1/2}$. The elastic regime holds only in a narrow range of radii, since χ is usually large compared to $\sigma_{\text{break-up}}$ or σ_{water}. The value of the elastic modulus can also incorporate the presence of any solid-like shell material that sustains tensile stress (such as the polyethyleneglycol polymer in SonoVue® contrast agent bubbles [5]). We assign a constant elastic modulus in this state, slightly caricaturing the quasi-static profiles of Fig. 2.1, a simplification of the model to facilitate calculation.

  Within this regime the surface tension is a linear function of the area, or of the square of the radius, and for small variations around a given radius R_0, it can be written as:

$$\sigma(R) = \sigma(R_0) + \chi\left(\frac{R^2}{R_0^2} - 1\right) \simeq \sigma(R_0) + 2\chi\left(\frac{R}{R_0} - 1\right) \quad \text{when} \quad |R - R_0| \ll R_0. \tag{2.1}$$

The lipid monolayer behaves as if composed of a thin solid and elastic material, see the appendix for the derivation of the tension of a thin elastic shell.

- Ruptured state, $\sigma = \sigma_{\text{water}}$.
  A fast expansion, such as the one triggered on a bubble by an ultrasonic pressure pulse, does not allow much time for any phase change and the monolayer is likely to break at a critical tension $\sigma_{\text{break-up}}$, exposing bare gas interfaces to the liquid. The bare interface has a tension value of σ_{water}. The break-up tension can be higher than σ_{water}, since any polymer component confers more cohesion to the shell, and shifts the break-up to higher tensions. The introduction of a high tension break-up was motivated by the observation of resistant bubbles, as will be exposed further.

  After break-up we assume that surface tension relaxes to σ_{water}. Even if the phospholipid monolayer rafts are likely to display non-isotropic tensions and shear stresses (being solid), the expansion is uniform before rupture, and the stress is likely to remain close to uniformity on average. The average tension value is settled in this case by the local mechanical equilibrium between the solid rafts and the bare interfaces, the latter pulling with the tension σ_{water}.

2.2.2 Dynamics of the coated bubble

During the oscillation, the dynamical surface tension will vary, since it is a function of the bubble area and therefore of the bubble radius. We therefore write the effective surface tension $\sigma(R)$ to emphasize this dependence. In motion, the balance of normal stresses at the interface reads

$$P_g(t) - P_l(t) = \frac{2\sigma(R)}{R} + 4\mu\frac{\dot{R}}{R} + 4\kappa_s\frac{\dot{R}}{R^2}, \tag{2.2}$$

with P_g the gas pressure in the bubble, P_l the liquid pressure, μ the surrounding liquid viscosity and κ_s the surface dilatational viscosity from

the monolayer. The first term on right-hand side is the capillary pressure term, while the second is the stress arising from the frictions in the liquid and the third from frictions in the shell. The last term was initially derived for a layer of finite and constant thickness ϵ ($\epsilon \ll R$) by Morgan *et al.* [15], the dilatational viscosity writing $\kappa_s = 3\epsilon\mu_{\text{lipid}}$, with μ_{lipid} the bulk lipid viscosity. Here we use only κ_s to describe the monolayer shell surface viscosity, following Chatterjee and Sarkar [16]. In this model κ_s does not depend on the surface area, nor does it exhibit any hysteresis. Note that the shear viscosity of the surface does not come into play in the present situation, because of the radial motion of the bubble.

The Laplace capillary pressure term writes $\frac{2\sigma(R)}{R}$ including the effective surface tension, *without any additional terms*, contrary to a previous statement in an article by Glazman [17], who expressed the capillary pressure by the erroneous expression $\frac{2\sigma}{R} + \frac{\partial\sigma}{\partial R} = \frac{2}{R}(\sigma + \chi(\frac{R_0}{R})^2)$. We demonstrate here why: the capillary overpressure derives from the mechanical equilibrium of all forces acting on the interface (of vanishing mass), that is the infinitesimal work δW of the forces cancels out for small bubble radius variation. By definition, the work associated with a variation dA of the area is σdA [18], while the pressure work from a variation dV of the volume is $-(P_g - P_l)dV$. Owing to the mechanical equilibrium of the interface, the sum of these works vanishes, and we obtain the static capillary term of equation (2.2). In the analysis by Glazman, the surface work is expressed incorrectly by $\sigma dA + Ad\sigma$ (instead of σdA) from the differentiation of a surface potential energy $E = \sigma A$: actually this last expression of the surface potential energy ($E = \int \delta W_{surface}$ by definition) is valid only when σ is constant.

The popular model of Morgan *et al.* [15] for coated microbubbles improves the description of viscous frictions, but is based on the analysis of Glazman for the elasticity of the lipid shell, equivalent to the introduction of an effective surface tension $\sigma(R) = \sigma_0 + \chi(\frac{R_0}{R})^2$ that fails to describe a coated bubble. Physically it would mean that surface tension always decreases when the bubble is inflated, in contrast with the behavior of lipid monolayers or elastic solid shells.

The hydrodynamics of the liquid motion around the bubble is modeled by the (modified) Rayleigh–Plesset equation $\rho_l(R\ddot{R} + \frac{3}{2}\dot{R}^2) = P_l(t) - P_0 - P_{ac}(t) - \frac{R}{c}\frac{dP_g(t)}{dt}$, with P_0 the ambient pressure, $P_{ac}(t)$ the acoustic pressure, and c the velocity of sound in the liquid. This equation proved to be accurate and robust even in the extreme conditions of sonoluminescence [19]. We choose an ideal polytropic ideal gas law $P_g \propto R^{-3\kappa}$, with κ

the polytropic gas exponent. It is 1 for bubbles behaving isothermally, and equal to the ratio of specific heats for bubbles behaving adiabatically [20] (close to 1.095 for SF_6). In the following, the thermal diffusion length in the gas during a period being small compared to the radius, we use the adiabatic version.

Combining the Rayleigh–Plesset equation and the polytropic gas law with the boundary condition (2.2) we obtain the model for the bubble dynamics:

$$\begin{aligned}\rho_l\left(R\ddot{R}+\frac{3}{2}\dot{R}^2\right) = \left(P_0+\frac{2\sigma(R_0)}{R_0}\right)\left(\frac{R}{R_0}\right)^{-3\kappa}\left(1-\frac{3\kappa}{c}\dot{R}\right)\\ -P_0-\frac{2\sigma(R)}{R}-\frac{4\mu\dot{R}}{R}-\frac{4\kappa_s\dot{R}}{R^2}-P_{ac}(t),\end{aligned} \tag{2.3}$$

with R_0 the equilibrium radius of the bubble. This equation is identical to a free gas bubble equation, except from the effective surface tension $\sigma(R)$ term and the shell viscosity term. The tension expressed in our monolayer model described above, and expressed here in terms of the bubble radius writes:

$$\sigma(R)=\begin{cases}0 & \text{if } R\le R_{\text{buckling}}\\ \chi\left(\frac{R^2}{R^2_{\text{buckling}}}-1\right) & \text{if } R_{\text{buckling}}\le R\le R_{\text{break-up}}\\ \sigma_{\text{water}} & \text{if ruptured and } R\ge R_{\text{ruptured}}\end{cases} \tag{2.4}$$

The third regime appears after rupture of the shell, when $\sigma_{\text{break-up}}$ has been reached (see broken line of fig. 2.2).

For small vibration amplitudes within the tensed elastic state, the surface tension can be linearized around a constant value, with $\sigma(R)\simeq\sigma(R_0)+2\chi\,(R/R_0-1)$, from equation (2.1). Implemented in the dynamical equation its yields the same pressure term $-2\sigma(R)/R=-2\sigma(R_0)/R-4\chi(1/R_0-1/R)$ as in the model proposed by de Jong *et al.* [21] for thin elastic shells. The shell stiffness coefficient S_p they introduced is simply related to the present shell elasticity by $S_p=2\chi$, while their shell friction coefficient writes $S_f=12\pi\kappa_s$. We stress here again that the model by de Jong *et al.* [21] is limited to small amplitudes of vibration (for effective tensions bounded between 0 and σ_{water}, or for R in between R_{buckling} and R_{collapse}), while the present model extends the oscillation to unbounded, large amplitudes.

2.2.3 Implications of the model: bubble compressibility

The effective tension model drastically changes the compressibility of the bubble. For slow variations of the ambient pressure P, at frequencies small compared to the resonance frequency, we can compute the equilibrium radius response, see Fig. 2.3, setting $\dot{R} = 0$ in equations (2.3) and (2.4).

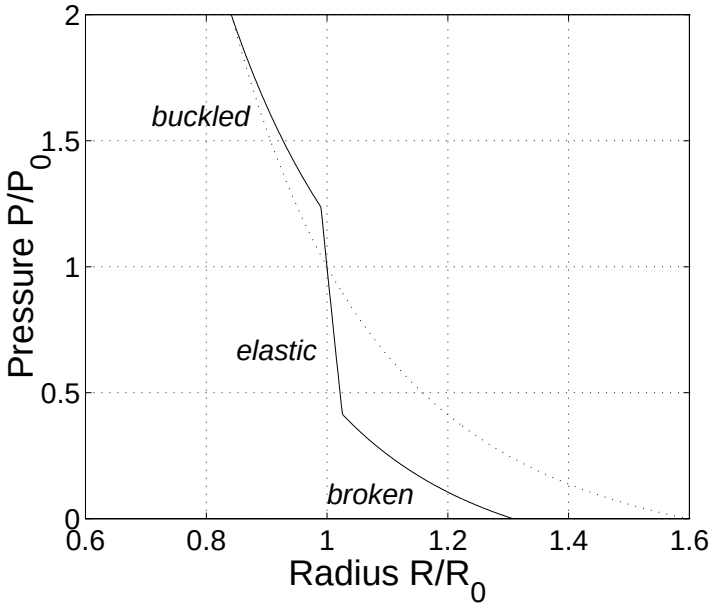

Figure 2.3: Ambient pressure versus equilibrium radius for a coated bubble (continuous line) and a free gas bubble (dotted line). At atmospheric pressure, the bubble radius is $R_0 = 2\,\mu m$. The coated bubble is initially in the elastic state ($R_{\text{buckling}} = 1.98\,\mu m$, $\chi = 1$ N/m.)

From the equilibrium, we also derive the compression modulus of the bubble, K_V, with:

$$K_V = -V\left(\frac{dP}{dV}\right) = \begin{cases} \kappa P & \text{for the buckled state} \\ \kappa P + \frac{4}{3}\frac{\chi}{R} & \text{for the elastic state} \\ \kappa P + \frac{3\kappa-1}{3}\frac{2\sigma_{\text{water}}}{R} & \text{for the free bubble/broken shell state} \end{cases} \tag{2.5}$$

with V the bubble volume, a polytropic exponent κ close to 1 for slow and isothermal compressions, and in the limit of $\chi \gg \sigma_{\text{water}}$ (usual for phospholipids). The compression modulus is much higher when the bubble is in the elastic state: this is reflected in the much steeper slope of the curve of Fig. 2.3. When the pressure is increased enough the bubble buckles, and becomes very compressible, even more than an uncoated free gas bubble of the same radius (whose internal pressure is increased by capillarity).

The change in compressibility is reflected on the dynamics of small amplitude oscillations as well. The linearization of the equations, setting $R(t) = R_0(1 + x(t))$, provides a damped oscillator equation $\ddot{x} + 2\gamma\dot{x} + \omega_0^2 x = -P_{ac}(t)/\rho_l R_0^2$, with a damping coefficient $\gamma = 2\mu/\rho_l R_0^2 + 2\kappa_s/\rho_l R_0^3 + 3\kappa(P_0 + 2\sigma(R_0)/R_0)/2c\rho_l R_0$, and an eigenfrequency simply writing:

$$\omega_0^2 = \frac{3}{\rho_l R_0^2} K_V. \tag{2.6}$$

In the free bubble state, this equation provides the Minnaert frequency as expected. It can be concluded that bubbles in the elastic state have a much higher resonance frequency than free or buckled bubbles, because their compression modulus is higher, consistently with the derivation of de Jong [21].

2.3 Results

2.3.1 Compression-only behavior

At small acoustic amplitudes, the model presented above provides a linear radius response to the pressure similar to other Rayleigh–Plesset models with constant surface tension.

Under large pressure amplitudes, the bubble will experience an original non-linear response. It will likely buckle in its compression phase, which cancels out any surface tension. On the other hand the surface tension rapidly rises during the expansion phase, and this asymmetry in surface tension provides an asymmetry in capillary pressure, especially strong for small bubbles. The radius response curve displays this asymmetry by a 'compression-only' behavior.

Recent experiments, realized with the high-speed camera Brandaris 128 [22], reveal the existence of such asymmetric oscillations of bub-

bles. The experiment was conducted as follows: SonoVue® and BR14 contrast bubbles, supplied by Bracco Research S.A., Geneva, Switzerland, were prepared in the vial about 24 hours prior to the recording of their dynamics. Both types of bubbles present a phospholipidic coating, SonoVue® containing SF_6 gas [5], while BR14 contains the even less soluble C_4F_{10} gas [23]. The contrast bubbles were led through a capillary fiber inside a small water-filled container. An Olympus microscope with a $60\times$ high resolution water immersed objective and a $2\times$ magnifier produced an image of the contrast bubbles. The image was then relayed to the high speed framing camera Brandaris 128. A broadband single element transducer was mounted at 75 mm from the capillary. A Tektronix AWG 520 arbitrary waveform generator provided a signal amplified by an ENI A-500 amplifier. The bubble response was investigated with sequential ultrasound bursts of 8 cycles at frequencies ranging from 1.5 MHz to 5 MHz. The camera was operated at a framing rate of 15 million frames per second, resolving the insonified microbubble dynamics. From the images (see Fig. 2.4) the radius versus time curves for each individual bubble were extracted (Fig. 2.5A), from which the compression-only behavior is apparent.

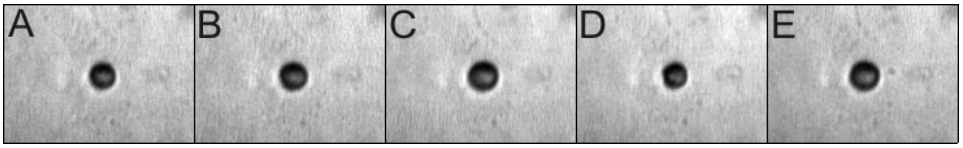

Figure 2.4: Consecutive images of a contrast agent bubble from the high speed camera Brandaris operated at 14.3 million frames per second (time intervals between images are thus 69.8 ns), during one ultrasound cycle, of frequency 2.6 MHz. The bubble radius is initially 1.95 μm, and frame D shows the bubble compression.

This phenomenon is very well modeled with our effective surface tension model, see Fig. 2.5B, assuming the bubble to be initially in a tensionless state ($R_{\text{buckling}} = R_0$), and allowing the shell to support elevated tensions. Note that the fitted elastic modulus and shell viscosity of this shell are of the same order of magnitude than the average ones from attenuation measurements on bubble populations by Gorce *et al.* [24], who deduced an average shell elasticity $\chi = S_p/2 = 0.55$ N/m and shell friction $\kappa_s = S_f/12\pi = 7.2\times10^{-9}$ kg/s.

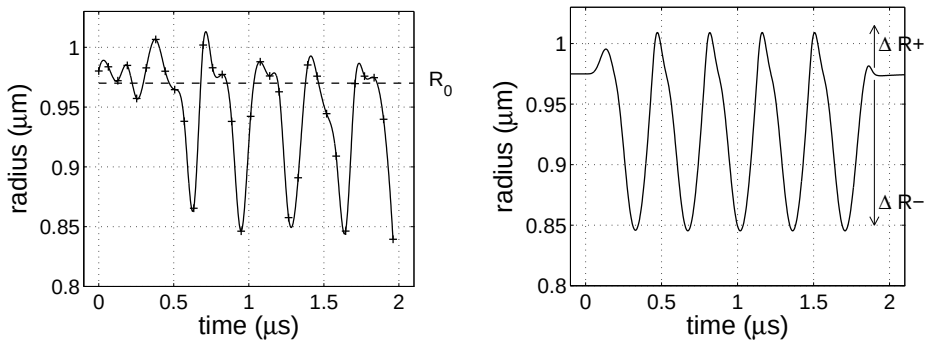

(A) Experimental recording (B) Simulation

Figure 2.5: (A) Experimental recording of the radius of a SonoVue® bubble versus time, with the fast framing camera Brandaris (beginning of a 2.9 MHz pulse with an acoustic pressure of 130 kPa). (B) Simulation. The fitted shell parameters are $R_{\text{buckling}} = R_0 = 0.975\ \mu m$, $\chi = 1$ *N/m,* $\kappa_s = 15 \times 10^{-9}$ *kg/s and* $\sigma_{\text{break-up}} > 1$ *N/m (resistant shell). The liquid properties are* $\rho_l = 10^3$ *kg/m*^{3}, μ *= 0.001 Pa.s, c = 1480 m/s, and the polytropic gas exponent is* κ *= 1.095.*

2.3.2 Aging of micro-bubbles: effect on the oscillation response

The initial effective tension of the monolayer depends on the history of the bubble. During their formation in the vial, lipid molecules are adsorbed at the interface, which reduces the effective surface tension, in proportion to the surface concentration n/A of adsorbed lipid molecules. The bubble is initiated in the tensed elastic state, its area being above the buckling area, $A_{\text{buckling}} = n * a_{\text{buckling}}$.

Dissolution of the gas in the surrounding liquid will 'deflate' the bubble and reduce its area towards a tension-less state (like the deflation of a rubber balloon), below which the bubble will buckle. In the tension-less state dissolution is much slower, since the capillary overpressure (typically an atmospheric pressure for micrometer sized bubbles) vanishes and the rate of radius decrease is proportional to inside pressure (which determines the dissolution concentration in the liquid according to Henry's law). Bubbles therefore *spontaneously tend to their buckling radius*, and then shrink much more slowly, compared to bubbles of constant surface tension. The reduction of surface tension is the main mechanism to account for increased longevity from the coating, since the gas permeability of 16 and 18-carbons phospholipids coatings is high [8].

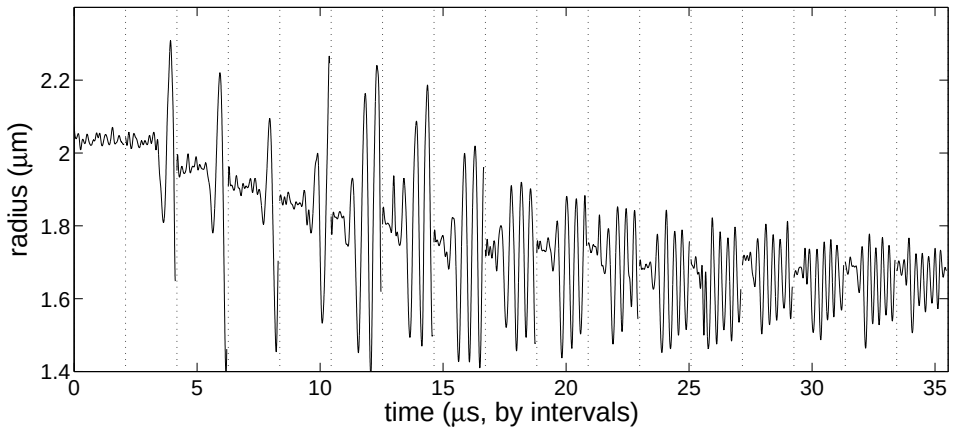

Figure 2.6: Experimental recordings of repeated acoustic pulses of 100 kPa on a single bubble, separated by 50 ms (break of time at vertical lines). The oscillation asymmetry increases pulse after pulse. (Frequency is increasing from 1.5 to 4 MHz, inducing amplitude changes).

Experiments show that asymmetric oscillations become more pronounced in the course of dissolution, see Fig. 2.6. Our interpretation is that the bubble reaches the tension-less state, where buckling occurs. According to the present model, the asymmetry is the signature of the variation in surface tension during each cycle, and this variation is the highest near buckling.

The asymmetry can be monitored by the ratio $\Delta R^+/\Delta R^-$ of the positive and negative radius excursions (defined by $\Delta R^+ = \max(R) - R_0$ and $\Delta R^- = R_0 - \min(R)$, both materialized on Fig. 2.5B). Simulations demonstrate indeed that the compression-only asymmetry ($\Delta R^+/\Delta R^- < 1$), is the more pronounced when $R_0/R_{\text{buckling}} \sim 1$ (see Fig. 2.7), the tension asymmetry during the oscillation being maximal.

This behavior is to be contrasted with the large amplitude oscillation of bubbles with a constant surface tension, which tends to produce higher positive excursions. It is seen on the same figure when the bubble radius is well above R_{buckling} (free bubble state, $\sigma = \sigma_{\text{water}}$) or well below R_{buckling} (tension-less state, $\sigma = 0$). The response curve slightly depends on frequency: varying the frequency between 1 and 4 MHz changes $\Delta R^+/\Delta R^-$ by about 10%.

Repeated pulses on a bubble accelerate the gas dissolution, as ev-

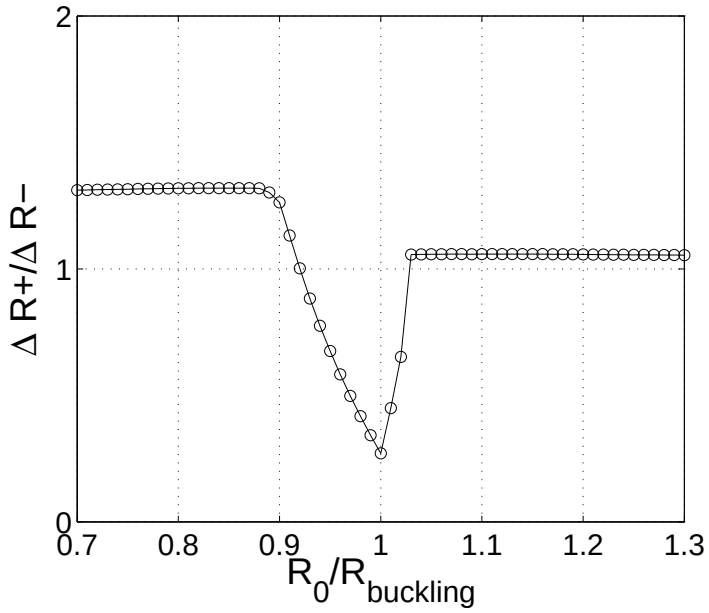

Figure 2.7: Simulated asymmetry of the oscillation for varying starting radii. Acoustic pulse and shell properties: same as Fig. 2.5.

idenced on Fig. 2.6 by the sudden decrease after the first pulse and the subsequent pulses. Two mechanisms could account for this effect. First, the initial pulses may expel some lipid molecules and reduce the buckling radius, to which the bubble will relax. Another explanation would be an 'inverse' rectified-diffusion generated by compression-only behaviors. The gas pressure increases during the compression phase, while it remains close to the pressure at rest during expansion (a symmetric oscillation would alternately compress and expand the gas). The concentration of gas in the liquid near the interface being proportional to gas pressure (Henry's law), the asymmetry, even small, tends to force more gas out of the bubble. This 'inverted' rectified-diffusion would be the opposite of the usual rectified-diffusion effect that counteracts dissolution for free gas bubbles [25].

A quantitative evaluation of this effect follows from the expression of the rate of dissolution of an oscillating bubble [25, 26]

$$\frac{d}{dt}\overline{R(t)} = \frac{Dc_0}{\rho_g \overline{R(t)}^2}\left(\frac{c_\infty}{c_0} - \frac{\overline{P_g(t)R(t)^4}}{P_0\overline{R(t)^4}}\right)\left(\int_0^\infty \frac{dh'}{\overline{(3h'+R(t)^3)^{4/3}}}\right)^{-1}, \tag{2.7}$$

where the overline is the average over one period, this equation being valid for an evolution slow at the scale of the period. The diffusivity of the gas is D, its volumic mass ρ_g, its saturation concentration c_0 and its concentration far from the bubble c_∞. The last factor containing an integration along the variable h' does not changes sign, and tends to R^4 for small amplitude oscillations. A compression-only signal produces a stronger 'averaged' pressure term $\overline{P_g(t)R(t)^4}/\overline{R(t)^4}$ (for instance it amounts to $1.2P_0$ from the simulation of Fig. 2.5B), which accelerates dissolution. Even at $R_{buckling}$, where the capillary overpressure vanishes, inverted rectified diffusion can force dissolution in a fully saturated liquid with $c_\infty/c_0 = 1$.

2.3.3 Rupture of the shell

The shell can withstand finite tensions only in its shell: starting from a compression-only signal and increasing the acoustic pressure step by step shows that a strong positive radius excursion suddenly appears above a critical pressure (see Fig. 2.8A). In this new state, the bubble oscillates as a free bubble: we interpret this behavior as the effect of the shell rupture.

To model the rupture, we assume that above a critical tension, $\sigma_{\text{break-up}}$, the shell breaks up and that part of the bubble surface is uncovered. Once this threshold has been reached, the surface tension upper bound will be the surface tension of water, σ_{water}. We can therefore simulate the effect of an increasing acoustic pressure on a bubble (see Fig. 2.8B).

The compression-only behavior ($\Delta R^+/\Delta R^- < 1$) is interrupted by the break-up of the shell: the non-linear behavior then favors positive excursions of the radius, as seen in experiment, as for standard large pressure Rayleigh–Plesset dynamics (see Fig. 2.9).

2.4 Conclusions

We presented a simple model for the dynamical properties of coated contrast agents bubbles, with three parameters: a buckling surface radius, a shell compressibility and a break-up shell tension. It predicts a

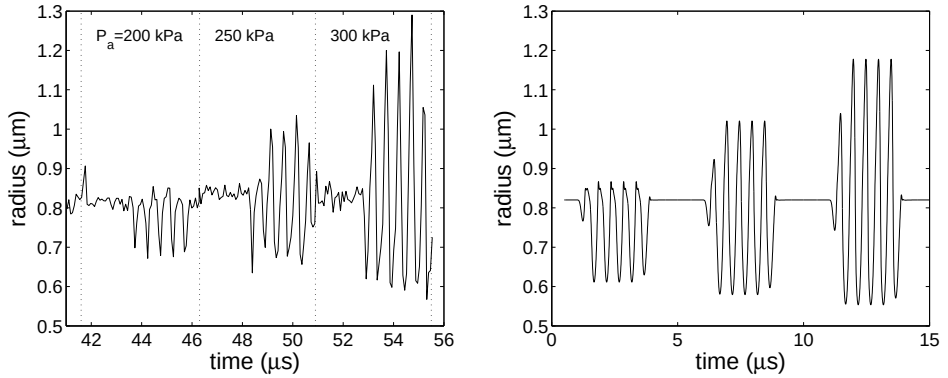

(A) Experimental recording (B) Simulation

Figure 2.8: (A) Experimental recordings of a BR14 bubble response to repeated 2 MHz pulses separated by 60 ms, with an increasing acoustic pressure. (B) Simulation with the same acoustic pressures. The fitted shell parameters are $R_{\text{buckling}} = R_0 = 0.82\ \mu m$, $\chi = 1$ *N/m*, $\kappa_s = 7.2 \times 10^{-9}$ *kg/s, while the critical break-up is* $\sigma_{\text{break-up}} = 0.13$ *N/m.*

compression-only behavior of the bubble, a highly non-linear response. It occurs when its radius is close to the buckling radius, a state that naturally occurs with dissolution of gas, or that can be accelerated by repeated pulses. High-frequency image recordings with lipid coated microbubbles reveal the existence of such asymmetric oscillations, and validate the model. The break-up of the shell is modeled by a third parameter, a finite tension of the bubble shell above which bare interfaces are created, with a corresponding change in bubble dynamics.

Possible applications of the model include: the characterization of coated microbubbles, the description of acoustic echoes and their use in non-linear or pulse-inversion imaging, and the prediction of the effect of repeated pulses or of long-term experiments.

2.5 Appendix: Comparison with the elasticity of a solid shell layer

Like monolayer coatings, the elasticity of a thin solid shell of thickness $\epsilon \ll R$ is characterized by a two-dimensional compression modulus $\chi = A\frac{d\sigma}{dA}$, where σ is the isotropic in-plane tension (shear of the surface does

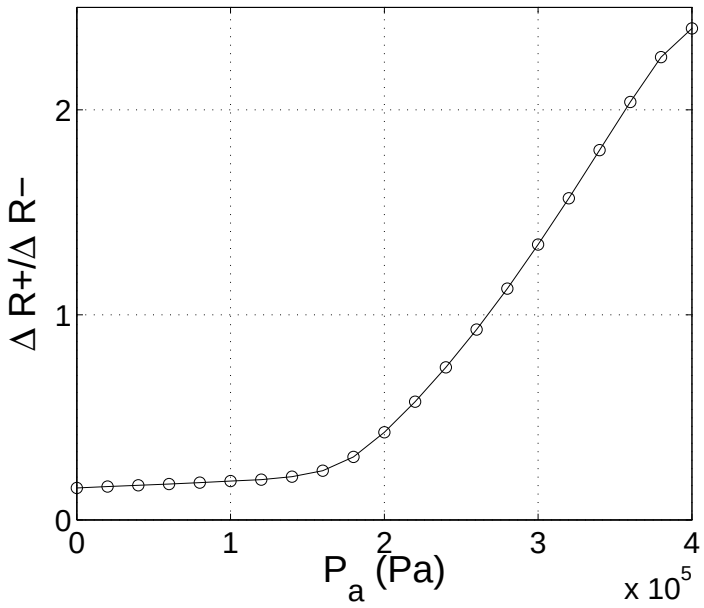

Figure 2.9: Effect of an increasing acoustic pressure on the asymmetry of the response (same parameters as in Fig. 2.8B).

not occur with a radial expansion, and bending is neglected assuming an initial curvature close to the spontaneous curvature). Additionally, the solid shell has two interfaces, with a surface tension σ_1 for the inner interface and σ_2 for the outer interface. The mechanical equilibrium balance for any small change in bubble area around the tensionless shell area A_0 reads $\delta W = \chi(A/A_0 - 1)dA + \sigma_1 dA + \sigma_2 dA - (P_g - P_l)dV = 0$, from which we obtain the pressure jump at the liquid-gas interface $P_g - P_l = 2(\sigma_1 + \sigma_2 + \chi(A/A_0 - 1))/R$. The effective surface tension of the shell thus reads:

$$\sigma = \sigma_1 + \sigma_2 + \chi\left(\frac{R^2}{R_0^2} - 1\right), \tag{2.8}$$

it is a linear function of the bubble area, like in the lipid *monolayer* coated bubble model (Eq. (2.1) for the elastic state, with $\sigma(R_0) = \sigma_1 + \sigma_2$).

The model for a thick elastic shell by Church [27] provides the same effective surface tension law when the shell thickness ϵ tends to be small compared to the radius. In this model the shell has a bulk shear modulus G_s and is incompressible in volume (the thickness thus varies around

its equilibrium value during the oscillation). From the Church model at small thicknesses we find that the shell contribution can be expressed with an effective tension law as in equation (2.8), using a two-dimensional elastic modulus $\chi = 3G_s\epsilon$, which is a classical result of the elasticity of thin plates [28].

References

[1] J. M. CRANE AND S. B. HALL, "Rapid compression transforms interfacial monolayers of pulmonary surfactant", Biophys. J. **80**(4), 1863–1872 (2001).

[2] A. L. KLIBANOV, "Ultrasound contrast agents: Development of the field and current status", Top. Curr. Chem. **222**, 73–106 (2002).

[3] S. LEE, D. H. KIM, AND D. NEEDHAM, "Equilibrium and dynamic interfacial tension measurements at microscopic interfaces using a micropipet technique. 2: Dynamics of phospholipid monolayer formation and equilibrium tensions at the water-air interface", Langmuir **17**(18), 5544–5550 (2001).

[4] J. M. CRANE, G. PUTZ, AND S. B. HALL, "Persistence of phase coexistence in disaturated phosphatidylcholine monolayers at high surface pressures", Biophys. J. **77**(6), 3134–3143 (1999).

[5] M. SCHNEIDER, M. ARDITI, M.-B. BARRAU, J. BROCHOT, A. BROILLET, R. VENTRONE, AND F. YAN, "BR1: A new ultrasonic contrast agent based on sulfur hexafluoride-filled microbubbles", Invest. Radiol. **30**(8), 451–457 (1995).

[6] F. PÉTRIAT, E. ROUX, J.-C. LEROUX, AND S. GIASSON, "Study of molecular interactions between a phospholipidic layer and a pH-sensitive polymer using the langmuir balance technique", Langmuir **20**(4), 1393–1400 (2004).

[7] M. I. SÁNDEZ, A. SUÁREZ, AND A. GIL, "Surface pressure-area isotherms and fluorescent behavior of phospholipids containing labeled pyrene", J. Colloid Interface Sci. **250**(1), 128–133 (2002).

[8] M. A. BORDEN AND M. L. LONGO, "Dissolution behavior of lipid monolayer-coated, air-filled microbubbles: Effect of lipid hydrophobic chain length", Langmuir **18**(24), 9225–9233 (2002).

[9] A. SAINT-JALMES, F. GRANER, F. GALLET, AND B. HOUCHMANDZADEH, "Buckling of a bidimensional solid", Europhys. Lett. **28**, 565–571 (1994).

[10] A. SAINT-JALMES AND F. GALLET, "Buckling in a solid langmuir monolayer: light scattering measurements and elastic model", Eur. Phys. J. B. **2**(4), 489–494 (1998).

[11] D. H. KIM, M. J. COSTELLO, P. B. DUNCAN, AND D. NEEDHAM, "Mechanical properties and microstructure of polycrystalline phospholipid monolayer shells: Novel solid microparticles", Langmuir **19**(20), 8455–8466, (2003).

[12] P. B. DUNCAN, AND D. NEEDHAM, "Test of the Epstein-Plesset Model for Gas Microparticle Dissolution in Aqueous Media: Effect of Surface Tension and Gas Undersaturation in Solution Duncan Needham", Langmuir **20**(7), 2567–2578 (2004).

[13] F. GRANER, S. PEREZ-OYARZUN, A. SAINT-JALMES, C. FLAMENT, AND F. GALLET, "Phospholipidic monolayers on formamide", J. Phys. II France **5**, 313–322 (1995).

[14] G. GAINES AND L. GEORGE, *Insoluble monolayers at liquid-gas interfaces*, Interscience Publishers, New York, 1966.

[15] K. E. MORGAN, J. S. ALLEN, P. A. DAYTON, J. E. CHOMAS, A. L. KLIBANOV, K. W. FERRARA, "Experimental and Theoretical Evaluation of Microbubble Behavior: Effect of Transmitted Phase and Bubble Size", IEEE Trans. Ultrason. Ferroelectr. Freq. Control, **47**, 1494–1508 (2000).

[16] D. CHATTERJEE AND K. SARKAR, "A newtonian rheological model for the interface of microbubble contrast agents", Ultrasound in Med. & Biol. **29**(12), 1749–1757 (2003).

[17] R. E. GLAZMAN, "Effects of adsorbed films on gas bubble radial oscillations", J. Acoust. Soc. Am. **74**(3), 980–986 (1983).

[18] P.-G. DE GENNES, F. BROCHARD-WYART, AND D. QUÉRÉ, *Capillarity and wetting phenomena: drops, bubbles, pearls, waves*, Springer, 2004.

[19] M. P. BRENNER, S. HILGENFELDT, AND D. LOHSE, "Single-bubble sonoluminescence", Rev. Mod. Phys. **74**(2), 425–484 (2002).

[20] A. PROSPERETTI, "Bubble phenomena in sound fields: part one", Ultrasonics **22**(2), 69–77 (1984).

[21] N. DE JONG, R. CORNET, AND C. LANCÉE, "Higher harmonics of vibration gas-filled microspheres. Part one: simulations", Ultrasonics **32**(6), 447–453 (1994).

[22] C. T. CHIN, C. LANCÉE, J. BORSBOOM, F. MASTIK, M. FRIJLINK, N. DE JONG, M. VERSLUIS, AND D. LOHSE, "Brandaris 128: A digital 25 million frames per second camera with 128 highly sensitive frames", Rev. Sci. Instrum. **74**(12), 5026–5034 (2003).

[23] M. SCHNEIDER, A. BROILLET, P. BUSSAT, N. GIESSINGER, J. PUGINIER, R. VENTRONE, AND F. YAN, "Gray-scale liver enhancement in VX2 tumor-bearing rabbits using BR14, a new ultrasonographic contrast agent", Invest. Radiol. **32**(7), 410–417 (1997).

[24] J. M. GORCE, M. ARDITI, AND M. SCHNEIDER, "Influence of bubble size distribution on the echogenicity of ultrasound contrast agents: A study of SonoVue(TM)", Invest. Radiol. **35**(11), 661–671 (2000).

[25] S. HILGENFELDT, D. LOHSE, AND M. P. BRENNER, "Phase diagrams for sonoluminescing bubbles", Phys. Fluids **8**(11), 2808–2826 (1996).

[26] M. FYRILLAS AND A. J. SZERI, "Dissolution or growth of soluble spherical oscillating bubbles", J. Fluid Mech. **277**, 381–407 (1994).

[27] C. C. CHURCH, "The effects of an elastic solid surface layer on the radial pulsations of gas bubbles", J. Acoust. Soc. Am. **97**(3), 1510–1521 (1995).

[28] D. BOAL, *Mechanics of the cell*, Cambridge University Press, Cambridge, (2002).

3

Microbubble spectroscopy of ultrasound contrast agents[§]

We present a new optical characterization of the behavior of single ultrasound contrast bubbles. The method consists of insonifying individual bubbles several times successively sweeping the applied frequency, and to record movies of the bubble response up to 25 million frames per second with an ultra-high speed camera operated in a segmented mode. The method, termed microbubble spectroscopy, enables to reconstruct a resonance curve in a single run. We analyze the data through a linearized model for coated bubbles. The results confirm the significant influence of the shell on the bubble dynamics: shell elasticity increases the resonance frequency by about 50%, and shell viscosity is responsible for about 70% of the total damping. The obtained value for shell elasticity is in quantitative agreement with previously reported values. The shell viscosity increases significantly with the radius, revealing a new nonlinear behavior of the phospholipid coating.

3.1 Introduction

Medical ultrasound imaging is based on scatter and reflection of sound from inhomogeneities in the tissue [1]. The scatter from blood is much weaker than the scatter from tissue. To increase the scattering properties from the blood pool, an ultrasound contrast agent (UCA) is introduced in the blood. An UCA is a liquid, containing small encapsulated microbubbles, which very efficiently scatter ultrasound [2–4]. In this way, it is

[§]Based on: Sander M. van der Meer, Benjamin Dollet, Marco M. Voormolen, Chien Ting Chin, Ayache Bouakaz, Nico de Jong, Michel Versluis, Detlef Lohse, "Microbubble spectroscopy of ultrasound contrast agents", J. Acoust. Soc. Am. **121**(1), 648-656 (2007)

possible to visualize and quantify the perfusion of tissue, like for instance the heart muscle, liver or kidney. Contrast agents are nowadays used in various medical investigations, e.g. in obtaining diagnostic information from the volume and shape of the heart ventricles, or to quantify the perfusion of various organs, like liver or kidney.

The fundamental understanding of the dynamics of contrast bubbles is a field of ongoing research. For example, the quantification of the response of contrast bubbles to ultrasound is an important research aspect. Until now, bubbles are characterized mainly by studying acoustically a representative sample of the UCA, containing many microbubbles [5–7]. From this data the overall resonance behavior of the sample can be deduced. Ideal contrast agents would be monodisperse in size, but in practice they have a size distribution which can be measured with, e.g., a Coulter counter, resulting in a mean size and size range [8]. For SonoVue® and also for BR-14 (Bracco Research S.A., Geneva, Switzerland), e.g., the mean radius is 1.5 μm, with 95% of the bubbles smaller than 10 μm. The polydispersity of the microbubbles makes it difficult to extract information on the physical properties of single bubbles, since the acoustical response of a bubble strongly depends on its size [8]. Furthermore, the acoustic pressure signal emitted by the bubbles is distorted by frequency dependent scattering and attenuation. On the other hand, measuring the acoustic response of a single individual contrast bubble is a difficult task [9]. First, it is difficult to isolate a single bubble in the focal region of a transducer: this would require at least 1 mm of distance between the bubbles. Second, extracting the absolute pressure emitted by the bubble from the measured response requires an accurate calibration of the transducer transfer function.

To overcome the difficulties associated with acoustical characterization, optical methods have been proposed [10–14]. Such methods are based on the direct measurement of the bubble radius, which, unlike the acoustical response, is not subject to distortion and in principle does not require difficult calibration. Furthermore, the interaction between bubbles (secondary Bjerknes forces) decays as the inverse square of their distance, fast enough to consider different bubbles to oscillate independently as soon as they are separated by a few (roughly ten) bubble radii. Isolating the response of a single bubble optically is thus less constraining than for acoustical measurements. However, optical methods exhibit other drawbacks: very high frame rates are required to resolve microbubble oscillations at several MHz, and the resolution is limited, since the microbubble size is just a little higher than the optical

resolution.

Here, we present a new optical method, that we term bubble spectroscopy, to characterize individual contrast bubbles. To resolve the oscillations of such bubbles, we use the ultra-high speed camera Brandaris [15], used in a segmented mode described in detail in Sec. 3.2: we scan the insonation frequency to reconstruct a resonance curve, from which we extract the resonance frequency and the total damping coefficient. The experimental methods are detailed in Sec. 3.3. In Sec. 3.4, we present the main results: we quantify the change of the resonance frequency with the radius, and discuss the influence of shell elasticity. We also quantify damping and show the influence of shell viscosity. We further discuss the accuracy of the proposed method in Sec. 3.5.

3.2 Bubble spectroscopy

3.2.1 The microbubble as a linear oscillator

For small enough acoustic forcing, it is well known [16, 17] that a bubble behaves as a linear oscillator; its relative radial excursion x, defined as $R = R_0(1+x)$, obeys the equation:

$$\ddot{x} + \omega_0 \delta \dot{x} + \omega_0^2 x = F(t), \tag{3.1}$$

with $f_0 = \omega_0/2\pi$ the eigenfrequency of the system and δ its (linear) dimensionless damping coefficient (equivalently, one can define the quality factor $Q = 1/\delta$), and F is the forcing term.

The amplitude of the radial variation of the bubble depends of the driving frequency $f = \omega/2\pi$. Writing $F(t) = F_0 \sin \omega t$ and $x(t) = x_0 \sin(\omega t + \varphi)$, one gets from Eq. (3.1):

$$x_0(\omega) = \frac{F_0}{\sqrt{(\omega_0^2 - \omega^2)^2 + (\delta\omega\omega_0)^2}}. \tag{3.2}$$

This equation defines the resonance curve, displaying a maximum at the resonance frequency:

$$f_{\text{res}} = f_0 \sqrt{1 - \frac{\delta^2}{2}}, \tag{3.3}$$

which is lower than the eigenfrequency in the presence of damping. Strictly speaking, Eq. (3.3) holds only if the damping coefficient δ is independent of ω. The main objective of our bubble spectroscopy method is

to fully characterize the linear response of single bubbles, by constructing its resonance curve and extracting from that the eigenfrequency and the damping coefficient. We show this on a simulation example in the following Subsection, and on experiments in Sec. 3.3.

3.2.2 Simulation example: power spectrum and resonance curve

As an example, we derive the resonance frequency and the damping coefficient from a numerical simulation. We compute the time evolution of the radius of a coated bubble subjected to an acoustic pressure, using the following model, adapted from Marmottant *et al.* [18]:

$$\begin{aligned}\rho_l\left(R\ddot{R}+\frac{3}{2}\dot{R}^2\right) &= \left[P_0+\frac{2\sigma_w}{R_0}\right]\left(\frac{R}{R_0}\right)^{-3\gamma}\left(1-\frac{3\gamma}{c}\dot{R}\right)\\ &\quad -P_0-\frac{2\sigma_w}{R}-4\chi\left(\frac{1}{R_0}-\frac{1}{R}\right)\\ &\quad -\frac{4\mu\dot{R}}{R}-\frac{4\kappa_s\dot{R}}{R^2}-P(t),\end{aligned} \tag{3.4}$$

where R, $\dot{R}$ and $\ddot{R}$ represent the radius, velocity and acceleration of the bubble wall (R_0 being the equilibrium radius), $\rho_l = 10^3$ kg/m^3 the volumetric mass of water, $P_0 = 10^5$ Pa is the ambient pressure and $P(t)$ the driving acoustic pressure, and γ the polytropic exponent; since the oscillations are fast, $\mathrm{Pe} = R_0^2\omega/D_{th} \gg 1$ [18] for bubbles of several microns in size in the MHz regime (here, $D_{th} = 2\times10^{-6}$ m^2/s is the thermal diffusivity of C_4F_{10}), we assume that this exponent equals the ratio of specific heats, $\gamma = 1.07$ for C_4F_{10}. Furthermore, $c = 1.5\cdot10^3$ m/s is the speed of sound in the fluid, $\sigma_w = 0.072$ N/m the surface tension, μ the dynamic viscosity and $P(t)$ is the acoustic pressure. Eq. (3.4) is based on the Rayleigh–Plesset equation, commonly used to model the behavior of bubbles (see Refs. [19–21] for general reviews on this subject) with two additional parameters to model the shell: an elasticity parameter χ (in N/m), and a shell viscosity κ_s (in kg/s) [27]. Various models including the shell properties in the Rayleigh–Plesset equation have already been proposed to model contrast agent bubbles [13, 18, 22–26]. Most of these models [13, 23–25] consider a shell of finite thickness, modeled as a 3D continuous medium, which may not be satisfactory for a monolayer shell. This is why Eq. (3.4) is inspired from models considering the shell as a 2D viscoelastic medium [18, 26]. More precisely, Eq. (3.4) is closely related to the model of Marmottant *et al.* [18], who suggested to model shell

elasticity through a radius-dependent surface tension over a certain range of radii (elastic range), below which the bubble buckles and above which the shell breaks. Basically, Eq. (3.4) would correspond to an infinite elastic range, which is relevant in this study, since we use low enough acoustic pressures to avoid both buckling (associated to nonspherical oscillations) and rupture (which would lead to fast bubble dissolution). Eq. (3.4) is also related to the model of De Jong *et al.* [22] by a more physical description of radiation and viscous damping. For the sake of simplicity, we account in this model for thermal damping as an effective viscosity, taking $\mu = 2 \times 10^{-3}$ Pa s, thus twice that of water.

Linearization of Eq. (3.4) yields the following eigenfrequency in the elastic regime:

$$f_0 = \frac{1}{2\pi}\sqrt{\frac{1}{\rho R_0^2}\left[3\gamma P_0 + \frac{2(3\gamma-1)\sigma_w}{R_0} + \frac{4\chi}{R_0}\right]}. \tag{3.5}$$

This eigenfrequency has two contributions: the Minnaert frequency [28],

$$f_M = \frac{1}{2\pi}\sqrt{\frac{1}{\rho R_0^2}\left[3\gamma P_0 + \frac{2(3\gamma-1)\sigma_w}{R_0}\right]}, \tag{3.6}$$

i.e., the eigenfrequency of an uncoated bubble, and a shell contribution which increases the eigenfrequency.

The linearization of Eq. (3.4) gives also the expression of the total damping coefficient: $\delta_{\text{tot}} = \delta_{\text{rad}} + \delta_{\text{vis}} + \delta_{\text{shell}}$, with a contribution coming from the sound re-radiated by the bubble, which writes at $\omega = \omega_0$ [16]:

$$\delta_{\text{rad}} = \frac{\omega_0 R_0}{c}, \tag{3.7}$$

a viscous contribution:

$$\delta_{\text{vis}} = \frac{4\mu}{R_0^2 \rho \omega_0}, \tag{3.8}$$

and a shell viscosity contribution:

$$\delta_{\text{shell}} = \frac{4\kappa_s}{R_0^3 \rho \omega_0}. \tag{3.9}$$

To be rigorous, a direct derivation from Eq. (3.4) gives an expression of δ_{rad} slightly different that the classical expression (3.7), but the order of magnitude remains the same, and we will see in Sec. 3.4.2 that radiation

is a secondary contribution to the total damping. We will thus keep the expression (3.7) for the radiation damping.

We compute Eq. (3.4) with a bubble of ambient radius R_0 = 2.8 μm. We numerically solve the bubble response $R(t)$ to an ultrasound burst of 8 cycles, whose two first and two last cycles are modulated by a Gaussian envelope, as in experiments. The acoustic amplitude is $P_a = 1$ kPa to minimize nonlinear effects, and the frequency range was chosen around the estimated resonance frequency, from 1.5 MHz to 2.5 MHz. Next, we apply a FFT algorithm on each $R(t)$-curve to compute its Fourier transform, and we take the square of this quantity: we get thus the power spectrum P_R of the radius-time curve. Typical $R(t)$-curves and their corresponding power spectra are shown in Fig. 3.1. At resonance, more energy goes into the oscillation than off-resonance. We quantify this effect by taking the area in the power spectrum in a band of Δf = 175 kHz around the maximum frequency f_{max}, which we term the response:

$$Re = \int_{f_{max}-\frac{1}{2}\Delta f}^{f_{max}+\frac{1}{2}\Delta f} P_R \mathrm{d}f.$$

The choice for a value of 175 kHz was found to be a suitable bandwidth for our data analysis. The total area in the power spectrum of the signal is an equivalent measure for the resonance, because nearly all the area in the power spectrum of the signal is located in the fundamental peak. We decided to take the area in a band around the peak, and we verified that the results are indeed in accordance.

We now redetermine the eigenfrequency and the total damping out of the resonance curve, in order to establish and verify the method we want to apply to the experimental data of Sec. 3.3. To do so, we fit the data points to the response of a harmonic oscillator (Eq. (3.2), which we rewrite as

$$Re(f) = \frac{Re_0}{(1 - f^2/f_0^2)^2 + (\delta f/f_0)^2}. \tag{3.10}$$

From the best fit of the data points (shown in Fig. 3.2 for our simulation example), we extract the eigenfrequency $f_0^{\mathrm{fit}} = 2.07$ MHz and the damping coefficient $\delta_{\mathrm{tot}}^{\mathrm{fit}} = 0.24$. We will motivate why we analyze the power spectrum, and not directly the radial oscillations, in Sec. 3.3.2.

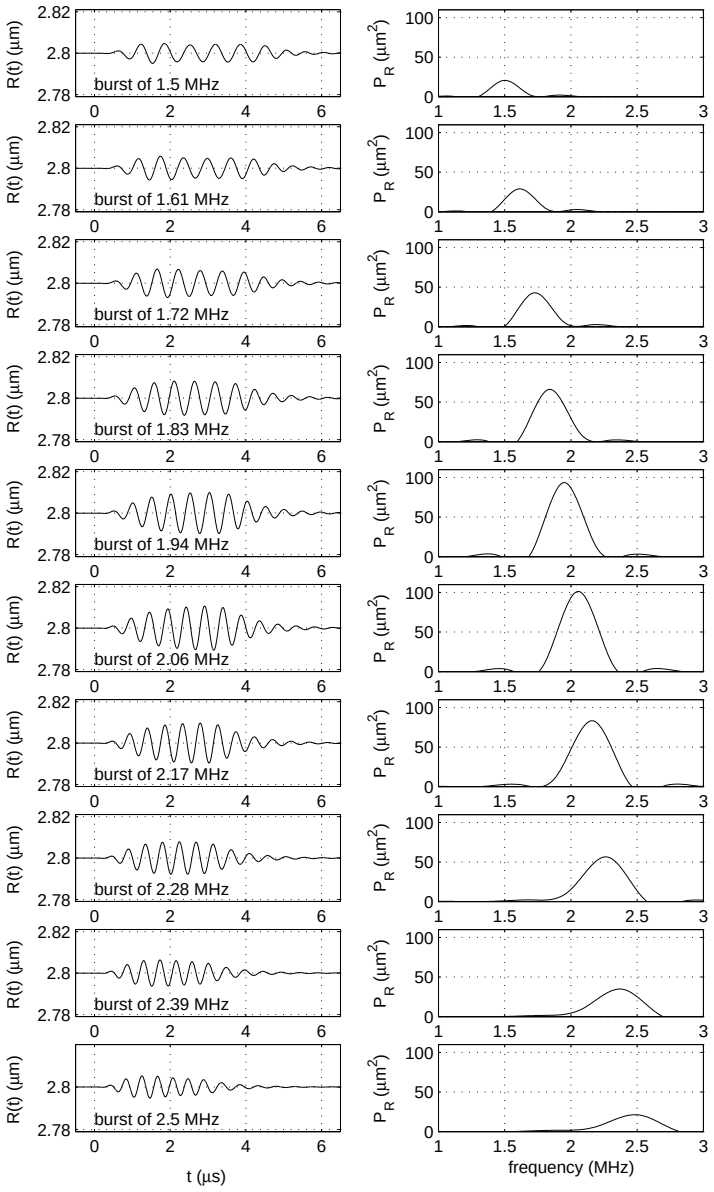

Figure 3.1: Simulated response of a bubble of initial radius $R_0 = 2.8\ \mu m$ to an ultrasound wave of 1 kPa of different frequencies. Left: radius-time response; right: power spectrum. The resonance frequency is at 2.07 MHz.

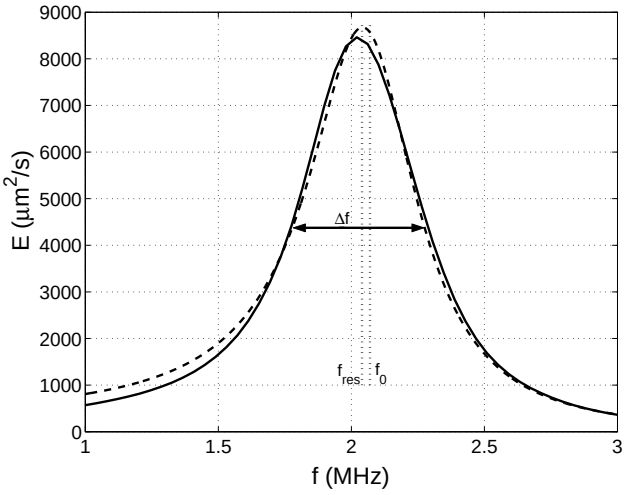

Figure 3.2: The simulated response (solid line) of a free 2.8 μm gas bubble on ultrasound bursts of 1 kPa, ranging in frequency from 1 to 3 MHz. The dashed curve is the fit to a harmonic oscillator (Eq. (3.10)) giving $f_0^{\text{fit}} = 2.07$ MHz and $\delta_{\text{tot}}^{\text{fit}} = 0.24$.

3.2.3 Analysis of the resonance curve

From the resonance curve obtained in the simulation example, we can determine the position where the amplitude of the oscillation is maximum, i.e. the resonance frequency: $f_{\text{res}}^{\text{curve}} = 2.02$ MHz. The best fit curve to the simulation data displays a resonance frequency compatible within 1% error: $f_{\text{res}}^{\text{fit}} = 2.04$ MHz. The resonance frequency is lower than the eigenfrequency $f_0^{\text{fit}} = 2.07$ MHz because of damping, but the shift remains very small. The resonance frequencies $f_{\text{res}}^{\text{curve}}$ and $f_{\text{res}}^{\text{fit}}$ fully agree with the theoretical estimate (Tab. 3.1). Second, the peak width is directly related to the total damping of the system δ_{tot}. A sharp peak indicates low damping, whereas a broad peak indicates high damping. More precisely, the width Δf of the response peak at half the maximum amplitude obeys: $\Delta f / f_0 = \delta_{\text{tot}}$. Measuring the width of the peak in Fig. 3.2 gives the following value for the damping coefficient: $\delta_{\text{tot}}^{\text{curve}} = 0.25$, in excellent agreement with the theoretical value: $\delta_{\text{tot}}^{\text{th}} = 0.24$ and the value obtained from fit: $\delta_{\text{tot}}^{\text{fit}} = 0.24$. This excellent agreement between the theory, the simulation curve and the fitting curve (Tab. 3.1) shows that our fitting procedure on the oscillation response is an accurate method to

	f_0 (MHz)	δ_{tot}	f_{res} (MHz)
Theory	2.06	0.24	2.03
Simulation curve	—	0.25	2.02
Fitting curve	2.07	0.24	2.04

Table 3.1: Comparison of the eigenfrequency f_0, the damping coefficient δ_{tot} and the resonance frequency f_{res} (related through Eq. (3.3)), from the theory (Eqs. (3.5) to (3.9)), the simulation curve and its fitting curve (Fig. 3.2).

extract both the eigenfrequency and the damping coefficient.

For a linear oscillator, the phase lag φ between the forcing term and the oscillator response is, according to Eq. (3.1):

$$\tan\varphi = \frac{\delta_{\text{tot}}}{\frac{f_0}{f} - \frac{f}{f_0}}. \tag{3.11}$$

If the oscillator is driven at frequencies well below resonance, it is in phase with the driving force ($\varphi = 0$). As the frequency is increased towards resonance, the displacement tends to lag behind the driving, so that at resonance the displacement has a phase shift of $\pi/2$. When the oscillator is driven at frequencies much greater than resonance, the displacement is in antiphase with the driving force ($\varphi = \pi$). In principle, measuring also the phase difference between ultrasound driving and bubble response could be used to determine the resonance frequency of contrast bubbles from experimental data. However, this requires precise timing. Therefore, presently we focus on the oscillation response.

3.3 Experiments

3.3.1 The setup

The experimental setup is schematically drawn in Fig 5.1. A dilute solution of individual BR-14 contrast bubbles (Bracco Research S.A., Geneva, Switzerland) is prepared and injected through a capillary fiber of diameter 200 μm immersed in water. The bubbles are illuminated from below with an optical fiber and an image is produced by an Olympus microscope with a 100$\times$ water-immersed objective and a 2$\times$ magnifier. We carefully check that only single bubbles are present in the field of view of the microscope. The image is relayed onto a CCD camera for orientation and size estimation, and simultaneously onto the Brandaris

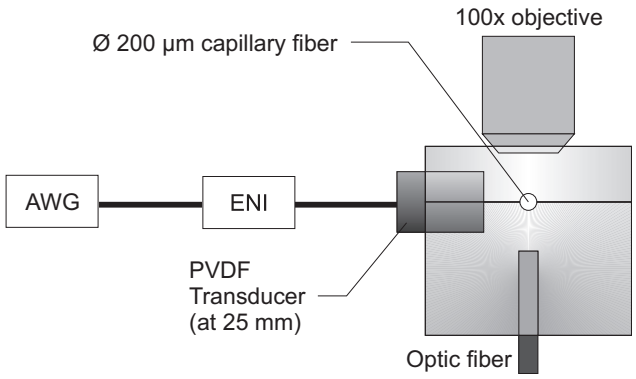

Figure 3.3: The experimental setup: an arbitrary waveform generator produces ultrasound signals that are amplified by an amplifier and led to a transducer. Contrast bubbles are injected through a 200 μm capillary fiber perpendicular to the plane of the figure. The contrast bubbles are imaged from the top through a 100$\times$ objective and illumination is provided from the bottom.

high-speed camera [15]. The camera can record six movies of 128 frames at up to 25 million frames per second. Furthermore, the camera was designed to operate in a segmented mode, in fact specifically to accommodate microbubble spectroscopy. In practice, the conventional single acquisition of 128 frames was replaced by recording two segments of 64 frames each, or four segments of 32 frames each. The camera houses memory space for six conventional acquisitions of 128 frames, before the images are transferred to the PC. Using two segments, this procedure results in the recording of 12 sets of 64 frames. Using four segments has the advantage of an increased frequency resolution (24 instead of 12), but reduces the sampling of the movies from 64 to 32 frames. The camera is operated at a framing rate of 15 million frames per second. The segmented mode allows us to construct a resonance curve of the bubble in a single acquisition, in less than one second.

The experiments described here were always done within 6 hours after the preparation of the contrast bubbles, to rule out potential changes in bubble behavior due to aging. The bubbles were introduced through the capillary fiber in the focus of the microscope. Once we identified a single bubble, we estimated its radius from the images of the CCD camera, and estimated its approximate resonance frequency through the Minnaert equation (3.6), taking into account that the shell elasticity shifts the resonance frequency up. The bubble was then subjected to a scan

of 12 (or 24) different frequencies, in a range of roughly 1 MHz below and above the expected resonance frequency. The contrast bubbles were insonified from the side by a broadband single element transducer (Precision Acoustics, PA081) with a center frequency of 1.7 MHz and a calibrated range of frequencies from 0.7 to 6 MHz. An arbitrary waveform generator (AWG), a Tabor 8026, connected to a PC, was used to produce the required waveforms, which were then amplified by an ENI 350L amplifier. The length of the ultrasound waveforms was 8 cycles, of which the first two and the last two were tapered taking a Gaussian envelope. The bubbles were investigated with sequential bursts of the ultrasound waveforms, with an acoustic pressure kept as low as possible to minimize nonlinear responses. In this paper, we present only results at driving pressures lower than 40 kPa. This prevented us from studying bubbles smaller than 1.5 μm in radius, since these bubbles do not oscillate significantly at these small pressures [40]. The pressures generated by the broadband single element transducer was calibrated with a 0.2 mm needle hydrophone (Precision Acoustics, SN1033). To maintain a constant pressure in the focus, we compensated for the frequency-dependent response of the transducer by adjusting the amplitude of the waveforms of different frequencies. The programming of the waveforms was done in Matlab. The waveforms were transferred to the AWG via a general purpose interface bus (GPIB).

3.3.2 Radius-time curves determination

From the images, we extract the radius-time information. The radius-time curves of individual bubbles were measured using a so-called dynamic programming algorithm [29]. The center of the bubble of interest is annotated in the first frame of the recording. This center point was then used to radially resample the bubble and its direct surrounding. The resulting image was used as an input to the algorithm to find the optimal path along the contour of the bubble. After transforming the contour back into the recorded frame the average bubble radius and corresponding center are determined. This center point is then used to repeat the above procedure for the next frame. After running through all frames the radius-time curve of the bubble is obtained. Through a calibration grid the conversion between pixels and micrometers is performed.

To quantify the amplitude of oscillations of a bubble, the simplest method would be to find the maximum and minimum radial excursion during the insonation. However, in experiments, this proved not to be the most accurate measurement for several reasons. First of all, due to

the finite sampling frequency of the signal, there is a difference between the recorded extrema and their actual values. Furthermore, the extrema need to be determined from only a few cycles of the bubble oscillation. Second, in experiments an off-resonance oscillating bubble often shows an amplitude overshoot in the first few cycles. Although we tried to minimize this by using a Gaussian envelope, it is somehow arbitrary to choose which of the extrema shows the real amplitude for that particular frequency and pressure. For all these reasons, we rather work on the Fourier transform of the radius-time curve. It also presents a maximum amplitude at resonance, and since it is an integrated quantity over the full $R(t)$ signal, it is much less sensitive to the sampling rate and to the short transients and overshoots of the $R(t)$ curve. In the following Section we describe the subsequent analysis.

3.3.3 Data processing

From the images, the radius-time curves for each individual bubble were measured for each frequency component. An example of such a curve is shown in Fig. 3.4.

We treat the radius-time curves as in Sec. 3.2.2: for each scanned frequency, we calculate the area in the power spectrum in a band around the maximum frequency, as the quantifier of the amplitude of bubble oscillation (Fig. 3.4). Plotting the results yields an experimental resonance curve which we fit to the linear oscillator expression (Eq. (3.10)). Three examples of such resonances curves are displayed in Fig. 3.5. We then record for each experiment the two following fitting parameters of Eq. (3.10): the eigenfrequency f_0 and the damping coefficient δ_{tot}. After careful selection (correct pressure, no significant shrinking of the bubble by loss of gas during insonation), we present 22 experimental data points.

3.4 Results

3.4.1 Eigenfrequency

In Fig. 3.6, we report the eigenfrequency $f_0 = \omega_0/2\pi$, obtained as explained in Sec. 3.3.3, for 22 experiments. As expected, the measured eigenfrequencies decrease with the bubble radius. They are also significantly higher than the Minnaert frequency (Eq. (3.6)), which confirms the influence of the shell. To quantify this influence, we fit the data points

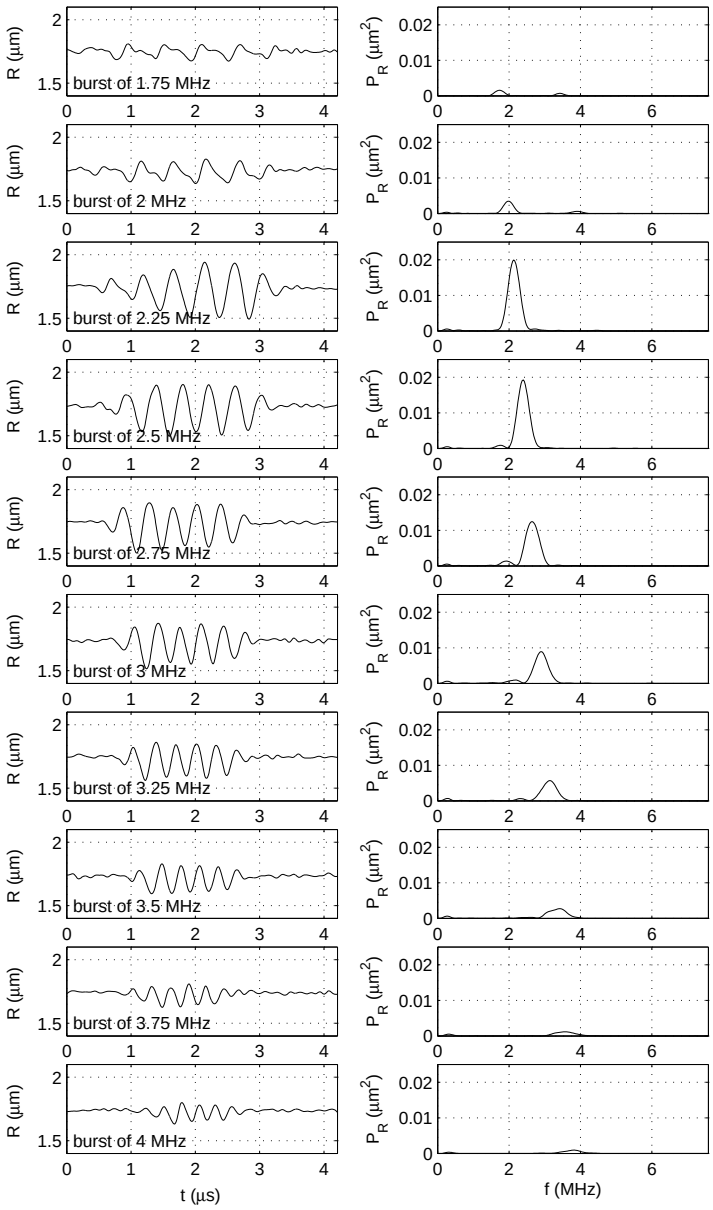

Figure 3.4: Experimental radius-time curves (left column), and corresponding power spectra (right column), for a bubble with an ambient radius of 1.7 μm during a scan of insonifying frequencies.

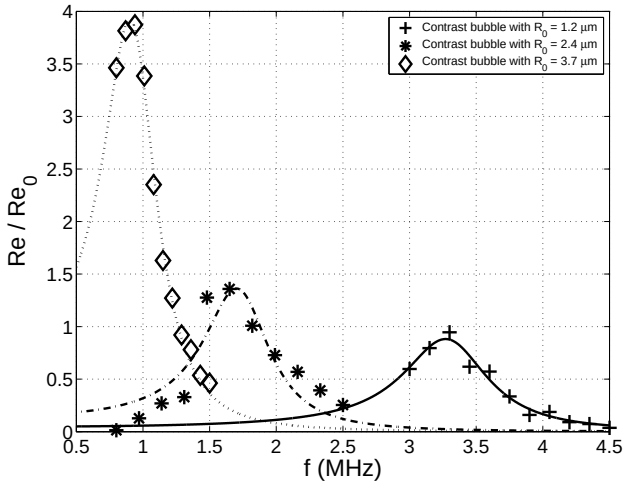

Figure 3.5: Experimental resonance curves for three different bubbles, and the corresponding fits by Eq. (3.10).

to Eq. (3.5). The best fit yields the following value of the shell elasticity parameter: $\chi = 0.54 \pm 0.10$ N/m, the error bar coming from the dispersion of the experimental data.

The value of χ is fully compatible with the previously reported values for SonoVue®. Using the model of De Jong *et al.* [22], which is similar to the model of Marmottant *et al.* [18] used here in the linear regime, Gorce *et al.* [8] gave a value of $\chi = 0.55$ N/m based on four analyzed samples. Marmottant *et al.* derived from their model a value of $\chi = 1$ N/m on a single example for the shell elasticity.

3.4.2 Damping

We now consider the damping coefficient, which is derived from the experimental data points by fitting to Eq. (3.10) (see Fig. 3.5). The damping coefficient is determined as a function of the bubble radius. The variation in the datapoints is not clearly correlated to the radius, so we rather present a typical example for a bubble of resting radius $R_0 = 1.9$ μm, see Fig. 3.7.

Damping arises from various sources: re-radiation of sound by the bubbles, thermal diffusion, bulk and shell viscosity. In the example of Fig. 3.7, we compute from Eqs. (3.7) and (3.8) $\delta_{\text{vis}} = 0.032$ and $\delta_{\text{rad}} = 0.022$,

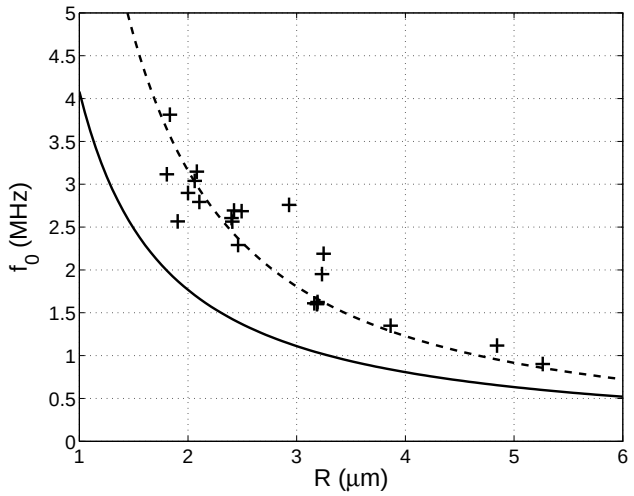

Figure 3.6: Experimentally determined eigenfrequency, plotted versus bubble radius. The solid curve shows the Minnaert frequency (Eq. (3.6)). The dashed curve shows the resonance frequency including shell elasticity. The best fit with Eq. (3.5) yields the following value for shell elasticity: $\chi = 0.54 \pm 0.10$ *N/m.*

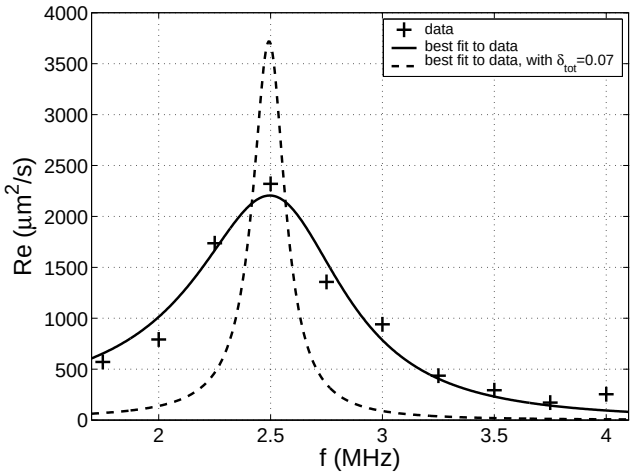

Figure 3.7: Example of an experimental resonance curve for a bubble with a resting radius $R_0 = 1.9\ \mu m$*. The solid curve is the fit to Eq. (3.10), giving* $f_0 = 2.56$ *MHz and* $\delta_{\text{tot}} = 0.26$*. The dashed line shows the fit to Eq. (3.10) with an imposed damping coefficient* $\delta_{\text{tot}} = 0.07$ *(see text) without shell damping.*

given the radius R_0 = 1.9 μm and the eigenfrequency $f_0 = 2.56$ MHz. Thermal damping is more difficult to express; from [30] and the value of the thermal diffusivity for C_4F_{10}, we get $\delta_{\text{th}} = 0.02$. These three sources give a contribution of 0.07 for the damping coefficient. We plot the resonance curve corresponding to this value in Fig. 3.7: clearly, this curve is too sharp to fit correctly the data, showing the significance of a fourth source of damping, arising from shell viscosity. More precisely, the fit to Eq. (3.10) with all free parameters gives a significantly higher value of the total damping coefficient, namely $\delta_{\text{tot}} = 0.26$. This implies a value of $\delta_{\text{shell}} = 0.19$ for the extra damping through the shell: in this example, shell viscous damping is thus responsible for 73% of the total damping; in average, this proportion is 68%: the shell is therefore the major source of damping. This result confirms existing studies [31], which showed the significant influence of the shell viscosity on the resonance properties of contrast bubbles. For the total set of 22 data points the value of the shell damping ranged from 0.05 to 0.4. The shell damping shows no clear dependence with the radius, see Fig. 3.8(A).

From δ_{shell} we can easily calculate the shell viscosity κ_s, see Eq. (3.9). In the example of Fig. 3.7, this gives $\kappa_s = 2.3 \cdot 10^{-8}$ kg/s. Analyzing all data points, we find a significant increase of the shell viscosity with the radius of the bubble (see Fig. 3.8(B)), as already reported in [13]. However, plotting κ_s as a function of the dilatation rate of the shell offers a more physical picture in terms of surface rheology. We estimate the dilatation rate as: $\dot{R}/R \approx \omega\Delta R/R_0 \approx 2\pi f_0 \Delta R/R_0$, where ΔR is the maximum amplitude of the radial oscillations. We plot κ_s versus the estimated dilatation rate in Fig. 3.8(C). The plot shows a clear decrease of the shell viscosity with the dilatation rate, which may be the signature of a rheological thinning behavior of the phospholipid monolayer shell. Such a behavior has already been observed for monolayers of myristic acid [32] and of poly(vinylacetate) [33]. Furthermore, the order of magnitude of the shell viscosity is 10^{-8} kg/s, which is compatible with previously reported values of $0.72 \cdot 10^{-8}$ kg/s [8] and $1.5 \cdot 10^{-8}$ kg/s [18].

3.5 Discussion and conclusions

3.5.1 Accuracy of the measurements

We discuss here various sources of bias of the measurements: shrinking of bubbles, compression-only behavior, and uncertainty on the measured

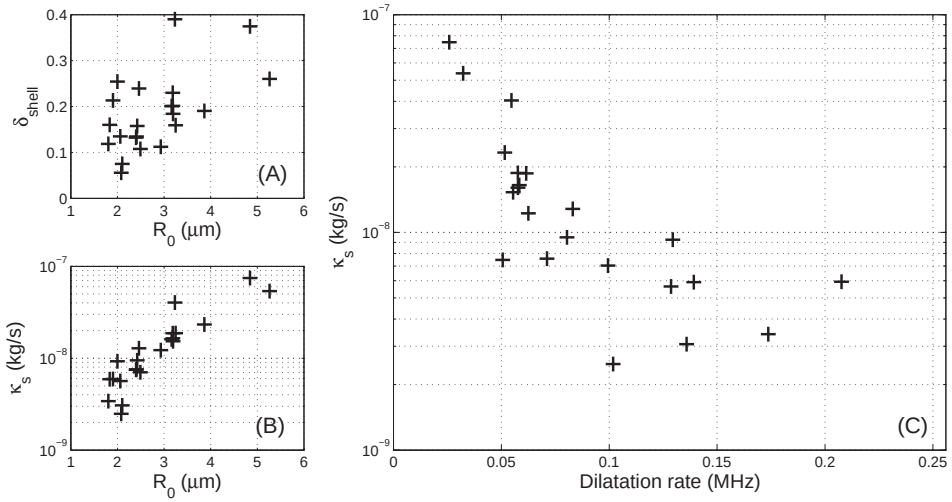

Figure 3.8: (A) Experimentally determined shell damping δ_{shell}, plotted versus the ambient bubble radius R_0. (B) Experimentally determined shell viscosity κ_s, plotted versus the ambient bubble radius R_0. (C) Plot of the shell viscosity as a function of the estimate of the dilatation rate $2\pi f_0 \Delta R / R_0$.

radius.

After each burst of ultrasound, some gas may escape from the bubble, reducing the resting radius of the contrast bubble. This unwanted effect is minimized by keeping the ultrasound pressure as low as possible, yet high enough to be able to distinguish the oscillation of the contrast bubble at different frequencies. Great care was taken to verify that the initial resting radius was equal to the final resting radius. In our experiments, we only considered oscillations with a relative decrease in radius less than 10%, hence we assume that the properties of the bubble do not change significantly during the insonation cycle. There is also no difference seen in an ascending or a descending frequency sweep.

Another difficulty is a nonlinear phenomenon referred to as "compression-only" behavior [34], due to the shell mechanical properties [18]. In the data analysis we included only data for which the ratio between the maximal extension and compression from the equilibrium radius is higher than 0.9: compression-only is then negligible.

There is also an uncertainty in the resting radius: since it equals only a few microns, bubbles behave like Mie scatterers [35], hence they create a complicated combination of diffraction and scattering in the focal plane

of the camera. This leads to some uncertainty in the image analysis, since the transition in contrast between bubble and background is gradual. The edge detection, described in Sec. 3.3.2, at the dark-bright interface at the edge of the bubble will in many cases not give the correct initial bubble radius. Only in the case of in-focus, on-axis, incoherent illumination with a sufficiently high imaging resolution the lowest cost at the dark-bright interface will give the correct bubble radius estimation. In all other cases, the cost needs to be slightly different, depending on the imaging system characteristics like system coherency, objective NA, and abberations (like focus error). In our case we estimate the error we make in the radius estimation at around 10%.

3.5.2 Nonlinear pressure and wall effects

The frame rate of 15 million frames per second that was used in the experiments enabled us to resolve the oscillations of the bubbles, to get precise power spectra (Fig. 3.4), and resonance curves (Fig. 3.5). We extract a resonance frequency by fitting the observed resonance curves with a linear oscillator response, neglecting the nonlinear influence of the acoustic amplitude, which may be questionable: numerical calculations for uncoated bubbles show that resonance curves become asymmetrical (skewed), and the maximum shifts to a lower frequency. For a driving pressure of 40 kPa the relative decrease of the resonance frequency has been reported to be as large as 10% [36, 37]. To address this question for coated bubbles, we perform the same simulation as in Sec. 3.2.2 with $P_a = 40$ kPa, which is the maximum value used in experiments, and compare the resonance curve with the one of Fig. 3.2 (see Fig. 3.9). We find no significant difference, neither in eigenfrequency nor in damping coefficient: the shell elasticity seems to counterbalance the nonlinear effect of pressure.

The presence of the top capillary wall, against which the bubbles rest because of buoyancy, is also expected to affect the resonance frequency [38, 41]. As a first approximation, the wall can be modeled as an image bubble, which yields the following prediction of the eigenfrequency of a bubble in contact with a wall: $f_{wall} = f_0\sqrt{2/3} \simeq 0.82 f_0$ [39]. More precisely, we compare the bubble response to an acoustic pressure of amplitude 1 kPa with and without wall in the same figure, Fig. 3.9. It shows indeed that the eigenfrequency is lowered in the presence of the wall by this factor 0.82. Therefore, the wall tends to lower the resonance frequency; this means that the shell elasticity, 0.54 N/m, that

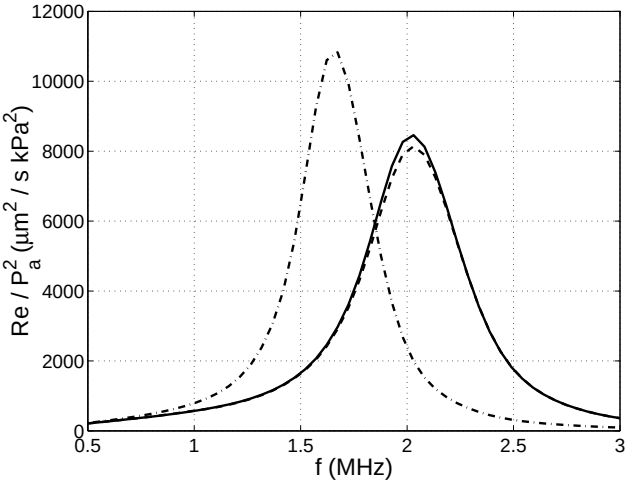

Figure 3.9: Resonance curves computed from Eq. (3.4) for an acoustic amplitude $P_a = 1$ kPa (solid line, same curve as Fig. 3.2) and 40 kPa (dashed line). Here, the response has been rescaled by P_a^2 to allow for comparison. For $P_a = 40$ kPa we find $f_0 = 2.07$ MHz and $\delta_{\text{tot}} = 0.24$. The third line is a simulation with wall present (dash-dotted line, Eq. (3.4) computed with an additional term modeling the wall as an image bubble [39]). With wall, we find $f_0 = 1.69$ MHz and $\delta_{\text{tot}} = 0.21$.

we measured by fitting the experimental data (Fig. 3.6), is underestimated.

3.5.3 Conclusions

We have presented a new, optical method to determine the resonance frequency of individual ultrasound contrast agents bubbles. This method relies on the use of an ultra-high speed camera, fast enough to resolve bubble oscillations at several Mfps. We operate the camera in a segmented mode, and scan the frequency over the bubble resonance. The bubble response is then recorded at each frequency, and analyzed to construct its resonance curve, from which a resonance frequency as well as a damping coefficient are extracted. The results confirm the influence of the viscoelastic properties of the shell on bubble behavior: The shell elasticity increases the resonance frequency compared to the uncoated bubble case and the shell viscosity proves to be a significant source of damping. Moreover, we showed that the shell viscosity increases with the bubble radius and suggested an explanation in terms of surface rheology.

The measured value of the shell elasticity, 0.54 N/m, and the order of

magnitude of the shell viscosity, 10^{-8} kg/s, are in good agreement with previous, independent measurements, giving confidence in this method as an efficient probe of bubble shell properties.

References

[1] T. SZABO, *Diagnostic Ultrasound Imaging: Inside Out*, Academic Press (2004).

[2] N. DE JONG, *Acoustic properties of ultrasound contrast agents*, Ph.D thesis, Erasmus University Rotterdam (1993).

[3] L. HOFF, *Acoustic Characterization of Contrast Agents for Medical Ultrasound Imaging*, Kluwer Academic Publishers, Dordrecht (2001).

[4] A. L. KLIBANOV, "Ultrasound contrast agents: Development of the field and current status", Top. Curr. Chem. **222**, 73–106 (2002).

[5] P. J. A. FRINKING, N. DE JONG, "Acoustic modeling of shell-encapsulated gas bubbles", Ultrasound Med. Biol., **24**(4), 523–533 (1998).

[6] P. J. A. FRINKING, N. DE JONG, E. I. CÉSPEDES, "Scattering properties of encapsulated gas bubbles at high ultrasound pressures", J. Acoust. Soc. Am., **105**(3), 1989–1996 (1999).

[7] W. T. SHI, F. FORSBERG, "Ultrasonic characterization of the nonlinear properties of contrast microbubbles", Ultrasound Med. Biol. **26**, 93–104 (2000).

[8] J. M. GORCE, M. ARDITI, M. SCHNEIDER, "Influence of bubble size distribution on the echogenicity of ultrasound contrast agents. A study of SonoVue(TM)", Investigative Radiology, **35**(11), 661–671 (2000).

[9] S. H. BLOCH, R. E. SHORT, K. W. FERRARA, E. R. WISNER, "The effect of size on the acoustic response of polymer-shelled contrast agents", Ultrasound Med. Biol. **31**, 439–444 (2005).

[10] J. E. CHOMAS, P. A. DAYTON, D. MAY, J. ALLEN, A. L. KLIBANOV, K. W. FERRARA, "Optical observation of contrast agent destruction", Appl. Phys. Lett. **77**, 1056–1058 (2000).

[11] N. DE JONG, P. J. A. FRINKING, A. BOUAKAZ, M. GOORDEN, T. SCHOURMANS, J. P. XU, F. MASTIK, "Optical imaging of contrast agent microbubbles in an ultrasound field with a 100-MHz camera", Ultrasound Med. Biol. **26**, 487–492 (2000).

[12] Y. SUN, D. E. KRUSE, P. A. DAYTON, K. W. FERRARA, "High-frequency dynamics of ultrasound contrast agents", IEEE Trans. Ultrason. Ferroelec. Freq. Contr. **52**, 1981–1991 (2005).

[13] K. E. MORGAN, J. S. ALLEN, P. A. DAYTON, J. E. CHOMAS, A. L. KLIBANOV, K. W. FERRARA, "Experimental and Theoretical Evaluation of Microbubble Behavior: Effect of Transmitted Phase and Bubble Size", IEEE Trans. Ultrason. Ferroelectr. Freq. Control, **47**, 1494–1508 (2000).

[14] P. A. DAYTON, J. S. ALLEN, K. W. FERRARA, "The magnitude of radiation force on ultrasound contrast agents", J. Acoust. Soc. Am., **112**, 2183–2192 (2002).

[15] C. T. CHIN, C. LANCÉE, J. BORSBOOM, F. MASTIK, M. E. FRIJLINK, N. DE JONG, M. VERSLUIS, D. LOHSE, "Brandaris 128: A digital 25 million frames per second camera with 128 highly sensitive frames", Rev. Sci. Instrum., **74**(12), 5026–5034 (2003).

[16] T.G. LEIGHTON, *The Acoustic Bubble*. London: Academic, (1994).

[17] S. HILGENFELDT, D. LOHSE, AND M. ZOMACK, "Response of bubbles to diagnostic ultrasound: a unifying theoretical approach", Eur. Phys. J. B, **4**, 247–255 (1998).

[18] P. MARMOTTANT, S. M. VAN DER MEER, M. EMMER, M. VERSLUIS, N. DE JONG, S. HILGENFELDT, D. LOHSE, "A model for large amplitude oscillations of coated bubbles accounting for buckling and rupture.", J. Acoust. Soc. Am., **118**(6), 3499–3505 (2005).

[19] M. S. PLESSET, A. PROSPERETTI, "Bubble Dynamics and Cavitation", Annu. Rev. Fluid. Mech. **9**, 145–185 (1977).

[20] C. E. BRENNEN, *Cavitation and Bubble Dynamics*, (Oxford University Press), Oxford, (1995).

[21] M. BRENNER, S. HILGENFELDT, D. LOHSE, "Single bubble sonoluminescence", Rev. of Mod. Phys., **74**(2), 425–484 (2002).

[22] N. DE JONG, R. CORNET, C.T. LANCÉE, "Higher harmonics of vibrating gas-filled microspheres. Part one: simulations." Ultrasonics, **32**(6), 447–453 (1994).

[23] C. C. CHURCH, "The effects of an elastic solid surface layer on the radial pulsarions of gas bubble", J. Acoust. Soc. Am. **97**, 1510–1521, (1995).

[24] L. HOFF, P. C. SONTUM, J. M. HOVEM, "Oscillations of polymeric microbubbles: Effect of the encapsulating shell", J. Acoust. Soc. Am. **107**, 2272–2280 (2000).

[25] D. B. KHISMATULLIN, A. NADIM, "Radial oscillations of encapsulated microbubbles in viscoelastic liquids", Phys. Fluids **14**, 3534–3557 (2002).

[26] K. SARKAR, W.T. SHI, D. CHATTERJEE, AND F. FORSBERG, "Characterization of ultrasound contrast microbubbles using in vitro experiments and viscous and viscoelastic interface models for encapsulation", J. Acoust. Soc. Am. **118**(1), 539–550 (2005).

[27] We thank Charles C. Church for pointing out a typo in Ref. [18]. The dilatational viscosity κ_s is expressed in units of kg/s.

[28] M. MINNAERT, "On musical air-bubbles and the sounds of running water." Phil. Mag., **16**, 235–248 (1933).

[29] M. SONKA, V. HLAVAC, R. BOYLE, *Image processing, analysis, and machine vision*, 2nd ed. Pacific Grove, CA: PWS Pub., (1999).

[30] A. PROSPERETTI, "Thermal effects and damping mechanisms in the forced radial oscillations of gas bubbles in liquids", J. Acoust. Soc. Am. **61**, 17–27 (1977).

[31] D. B. KHISMATULLIN, "Resonance frequency of microbubbles: Effect of viscosity", J. Acoust. Soc. Am. **116**, 1463–1473 (2004).

[32] C. LEMAIRE, D. LANGEVIN, "Longitudinal surface waves at liquid interfaces. Measurement of monolayer viscoelasticity", Colloids Surf. **65**, 101–110 (1992).

[33] F. MONROY, F. ORTEGA, R.G. RUBIO, "Dilatational rheology of insoluble polymer monolayers: Poly(vinylacetate)", Phys. Rev. E **58**(6), 7629–7641 (1998).

[34] N. DE JONG, M. EMMER, C. T. CHIN, A. BOUAKAZ, F. MASTIK, D. LOHSE, M. VERSLUIS, "'Compression-only' behavior of phospholipid-coated contrast bubbles", Ultrasound Med. Biol. **33**, 653–656 (2007).

[35] C. F. BOHREN, D. R. HUFFMAN, *Absorption and Scattering of Light by Small Particles*, Wiley, New York (1983).

[36] W. LAUTERBORN, "Nonlinear oscillations of gas bubbles", J.Acoust.Soc.Am. **59**(2), 283-293 (1976).

[37] A. PROSPERETTI, "Bubble phenomena in sound fields: part two", Ultrasonics, **22**, 115-124 (1984).

[38] E. M. B. PAYNE, S. ILLESINGHE, A. OOI, R. MANASSEH, "Symmetric mode resonance of bubbles attached to a rigid boundary", J. Acoust. Soc. Am. **118**, 2841-2849 (2005).

[39] M. STRASBERG, "The pulsation frequency of nonspherical gas bubbles in liquids", J. Acoust. Soc. Am. **25**, 536-537 (1953).

[40] J.S. ALLEN, D.E. KRUSE, P.A. DAYTON, AND K.W. FERRARA, "Effect of coupled oscillations on microbubble behavior", J. Acoust. Soc. Am. **118**(3), 1678-1690 (2003).

[41] M. EMMER, A. VAN WAMEL, D.E. GOERTZ, N. DE JONG, "The onset of microbubble vibration", Ultrasound Med. Biol. **33**, 941–949 (2007).

4

Microbubble shape oscillations excited through an ultrasound-driven parametric instability §

An air bubble driven by ultrasound can become shape-unstable through a parametric instability. Here we report time resolved optical observations of shape oscillations (mode n = 2 to 6) of micron sized single air bubbles for a range of acoustic pressures. The observed mode number n was found to be linearly related to the resting radius of the bubble. Above the critical driving pressure threshold for shape oscillations, which as expected is minimum at the resonance of the volumetric radial mode, the observed mode number n is independent of the forcing pressure amplitude. The microbubble shape oscillations were also analyzed theoretically by introducing a small non-spherical linear perturbation into a Rayleigh–Plesset-type equation, capturing the experimental observations in great detail.

4.1 Introduction

Bubbles insonified by ultrasound will generally exhibit a radial oscillation mode. In addition, surface waves can be generated through instabilities at the interface of the liquid medium and the gaseous content of the bubble. These surface modes have been studied extensively for droplets [1–4] and millimeter-sized bubbles [5, 6]. Surface mode vibrations for bubbles were first analyzed theoretically by Plesset [7] and later by Neppiras [8], Eller and Crum [9] and Prosperetti [10]. The overwhelming interest in sonoluminescing bubbles in the nineties lead to investigations into

§Based on: Michel Versluis, Peggy Palanchon, Dave Goertz, Ivo Heitman, Sander van der Meer, Benjamin Dollet, Nico de Jong, Detlef Lohse, "Microbubble shape oscillations excited through an ultrasound-driven parametric instability", in preparation.

surface mode oscillations for micron-sized bubbles by several groups, see e.g. [11–18]. Under sonoluminescing conditions the microbubbles are driven far away from their volumetric resonance frequency under relatively high acoustic pressures between 110 and 140 kPa. The fast timescales under which transients of shape oscillations occur have hitherto limited the observations to either photographic snapshots of the mode vibrations or to a stroboscopic multi-pulsing approach [17].

Here we overcome the difficulties of the observations of the surface modes through the use of ultra fast imaging. We conducted a set of controlled measurements for a variety of bubble diameters (radius between 10 and 50 μm), while investigating the onset of microbubble shape vibrations, fully resolved in time through the use of ultra high-speed imaging at 1 million frames per second. The bubbles are driven near their volumetric resonance frequency at mild acoustic pressures as to allow the surface modes to build up during insonation through a parametric instability.

4.2 Experiments

Single air bubbles with a radius ranging from 10 μm to 45 μm were generated in a regulated co-flow micropipette injector [19]. The injector allowed for a controlled production of microbubbles, both in radius and in separation distance. The bubbles were left to rise to the test section at a downstream distance of 4 cm from the injector. The bubbles were then insonified with an ultrasound pulse from an unfocused single element piezoelectric transducer (aperture of 31 mm) consisting of a burst of 10 cycles at a frequency of 130 kHz. Both the first two and the last two cycles were tapered with a Gaussian envelope. The dynamics of the free air bubbles was recorded with the Brandaris ultra high-speed camera [20]. The rotating mirror of the camera sweeps the incoming image along a quarter arc containing 128 highly sensitive CCDs. With a mirror rotation speed of 20 000 Hz a frame rate of 25 million frames per second can be achieved. The camera data controller system allows for the recording of six consecutive recordings of 128 frames each. This functionality was used to insonify the very same bubble at increasing acoustic pressures in six incremental steps from zero to 50 kPa for the smaller microbubbles ($R_0 <$ 25 μm) and from zero to 150 kPa for the larger ones. A frame rate of 1.25 million frames per second was used in all experiments.

Figure 4.1A shows a selection of high-speed recordings displaying the

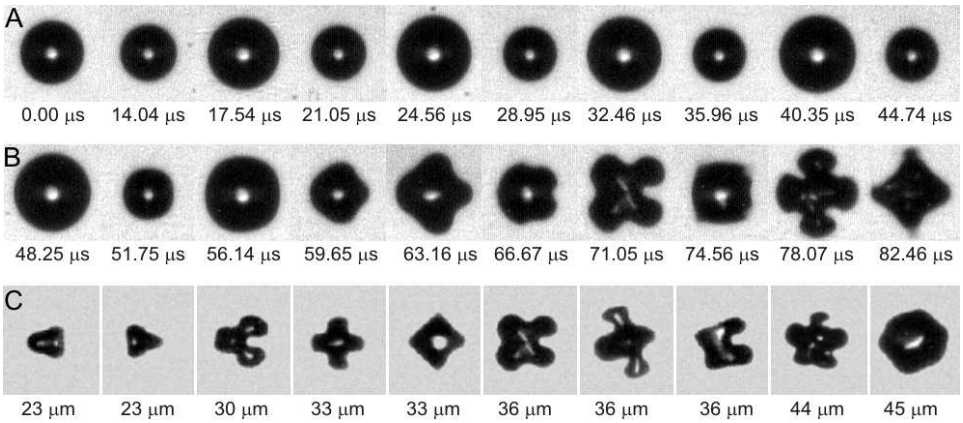

Figure 4.1: Growth of a surface mode vibration on a bubble with a radius of 36 μm as captured with the Brandaris high-speed imaging facility. The bubble is driven by a 10-cycle ultrasound pulse at a frequency of 130 kHz at an acoustic pressure of 120 kPa. First, the bubble oscillates in a purely volumetric radial mode (A), then after 4 cycles of ultrasound (B) the bubble becomes shape-unstable and a surface mode $n = 4$ is formed. (C) A selection of surface modes observed for air-filled microbubbles with a radius ranging from 23 to 45 μm. The bubble radius is shown below the images.

dynamics of a 36 μm radius bubble driven at an acoustic pressure of 120 kPa. The first frame shows the bubble at rest; the next nine frames show how the bubble oscillates radially in a spherical volumetric mode. Figure 4.1B shows the situation after 5 cycles of ultrasound (40 μs after ultrasound arrival) where the bubble develops a surface mode vibration, here with a mode number $n = 4$. When the acoustic driving stops, the surface mode vibration decays quickly and the bubble recovers its spherical shape. Many types of surface wave vibration were observed in the course of the experiments and a compilation of these is given in Fig. 4.1C.

4.3 Experimental analysis

In Fig. 4.2 the experimental analysis is illustrated. A bubble with a radius of 33 μm is insonified with a driving pressure of 120 kPa and a frequency of 130 kHz (Fig. 4.2A), and recorded with a frame rate of 1.13 Mfps. The high-speed recordings were processed through a dynamic programming

contour tracing algorithm [21]. This resulted in the position of the center of mass of the bubble as a function of time and the radius $R(\theta,t)$ of the bubble as a function of angle θ and time t (Fig. 4.2B), and the ambient radius of the bubble R_0 (Fig. 4.2C). The radial excursion as a function of the angle θ at t=80 μs, is displayed in Fig. 4.2D. A Fourier analysis of the bubble surface distortions resulted in a power spectrum from which the surface wave mode number was determined (Fig. 4.2E). Figures 4.2F & G show the time evolution of the growth of the shape instability is shown, respectively in a linear-linear and a log-linear scale.

From the analysis it followed, first, that all bubbles initially oscillate in a radial purely volumetric mode n = 0. Second, we noticed that, beyond a critical threshold of the acoustic pressure, surface modes can be generated after several acoustic cycles. The threshold depends on the ambient bubble radius. The threshold is minimal for those bubbles close to the volumetric resonance size of 25.1 μm at 130 kHz driving. Third, it was observed that bubbles have a preferential surface wave mode number and that the preferred mode number increases with increasing bubble size. Finally, we found that the preferential surface wave mode number does not depend on the forcing pressure of the ultrasound burst, provided it is beyond the threshold.

4.4 Theoretical analysis

Following Lamb's classical expression [22] for the natural frequency of oscillation ω_n of the n-th surface mode vibration,

$$\omega_n^2 = (n-1)(n+1)(n+2)\frac{\sigma}{\rho R_0^3}, \tag{4.1}$$

which contains cubic terms for both the mode number n and the bubble radius R_0, one would expect a linear relationship between n and R_0. However, if we compare this equation with our data (see Fig. 4.3, in the box below), the correspondence is quite poor, because Eq. (4.1) in fact holds for unforced freely oscillating bubbles, while our bubbles are periodically driven by ultrasound.

The mode preference for acoustically driven bubbles can be calculated in a theory following the work of Francescutto and Nabergoj [23], which in turn is based on the spherical stability analysis by Prosperetti [10]. In [23] an expression is derived for the pulsation amplitude threshold for a surface mode n as a function of the bubble radius. For the full derivation

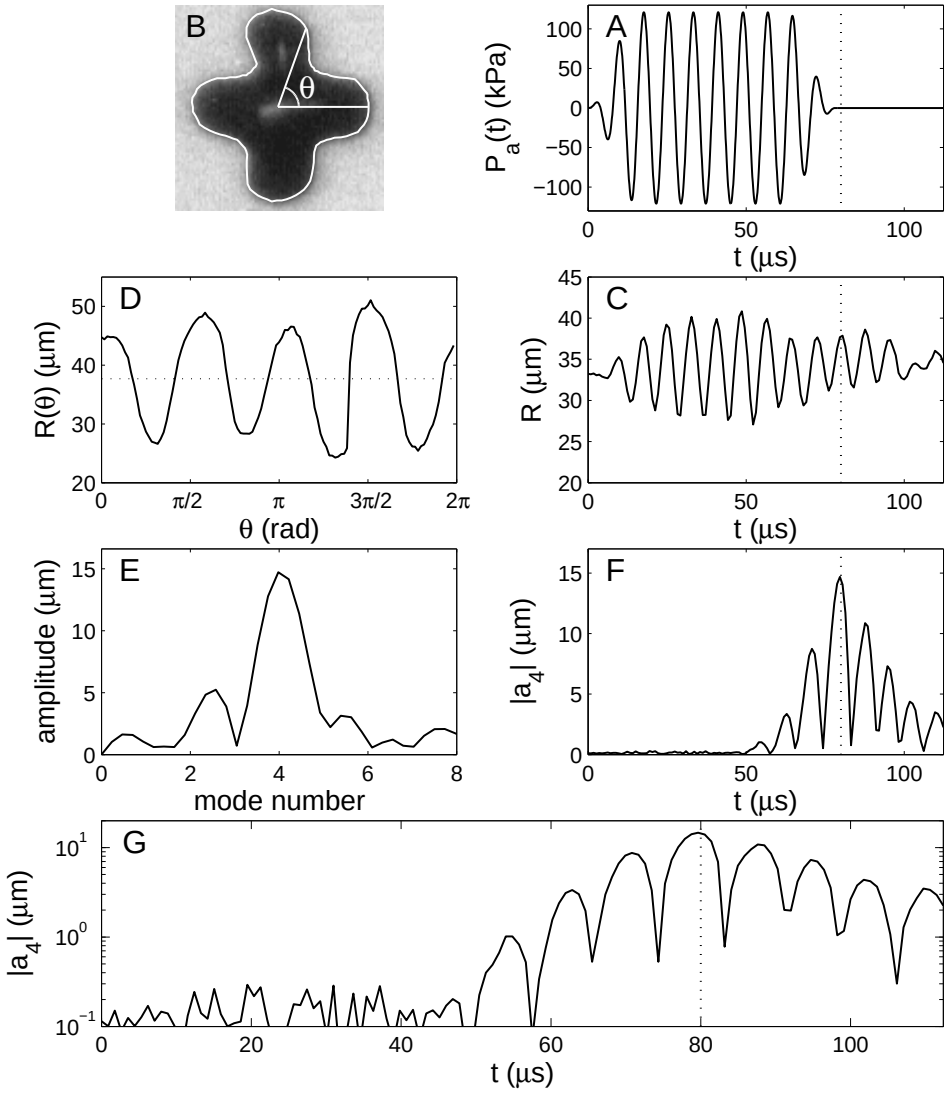

Figure 4.2: Experimental data. In (A) the driving pressure $P_a(t)$ is shown on a shape unstable bubble with an ambient radius of 33 μm is shown. (B) shows an image of the bubble at t=80 μs. Its contour is tracked by a contour tracing algorithm. (C) shows the radial oscillations of the bubble. (D) shows the radial excursion, plotted against the polar angle θ, at t=80 μs. (E) displays the mode number n which is derived from the Fourier transform of (D), and in both (F) and (G) the time evolution of the growth of the shape instability is shown, respectively in a linear-linear and a log-linear scale. The dotted lines in (A), (C), (F) and (G) indicate t = 80 μs.

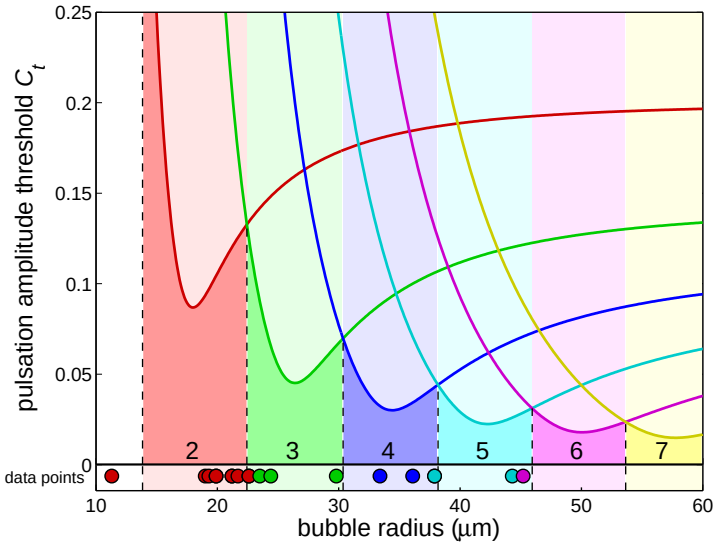

Figure 4.3: The solid lines represent the pulsation amplitude threshold following Francescutto and Nabergoj [23]. The color coding indicates the mode: red - mode 2, green - mode 3, blue - mode 4, turquoise - mode 5, magenta - mode 6, and yellow - mode 7. The dominant mode, using the same color coding, is indicated with a colored area. The experimental data points are included in the box below, using the same color coding.

we refer to ref. [23]. In short, the mode dynamics were expressed as a Mathieu equation, based on a linearized Rayleigh–Plesset equation. The analysis was limited to the sub-resonance oscillations. The separation line between shape stable and shape instable regions, which is also named pulsation amplitude threshold, can be calculated. The pulsation amplitude (defined as $C = (R_+ - R_-)/R_0$) threshold is given by the following expression:

$$C_t = \sqrt{\frac{(a-1)^2 + 4p}{(-\frac{3}{2}a + 2p + 2(n+\frac{1}{2}))^2 + q^2)}}, \tag{4.2}$$

where

$$a = \frac{4(n-1)(n+1)(n+2)\sigma}{\rho\omega^2 R_0^3} \tag{4.3}$$

$$p = \left(\frac{2(n+2)(2n+1)\mu}{\rho\omega R_0^2}\right)^2 \tag{4.4}$$

$$q = \frac{6(n+2)\mu}{\rho\omega R_0^2}, \tag{4.5}$$

with n the mode number, σ the surface tension, ρ the fluid density, and μ the dynamic viscosity of the fluid. For each mode, the pulsation amplitude threshold is plotted in Fig. 4.3. From the thresholds the dominant surface mode can be derived and this is indicated with a colored area in Fig. 4.3. The experimental data points are shown in a box below the pulsation amplitude threshold graph. There is a very good agreement with the calculated mode preferences.

We now look in more detail into the growth mechanism of the surface mode vibration. Three types of surface instabilities have been associated with oscillating bubbles [12, 18]: the parametric instability (over time scales of the oscillation period), for collapsing bubbles the afterbounce instability (over time scales of the bubble afterbounces) and for strongly collapsing bubbles the Rayleigh-Taylor instability (over time scales of the Rayleigh collapse, order ns). For the mildly oscillating bubbles studied here the most relevant one is the parametric instability. It exhibits maximal growth when the time scale of the forcing is of the order of the time scale of the natural volumetric oscillation frequency. Figure 4.2G indicates that the surface mode amplitude grows exponentially from cycle-to-cycle and therefore the bubble shape oscillations must be induced by such a parametric instability.

The parametric instability manifests itself in the growth of initially small perturbations on the spherical interface $R(t)$:

$$R(\theta,\phi,t) = R(t) + \varepsilon(\theta,\phi,t) = R(t) + a_n(t)Y_n(\theta,\phi), \tag{4.6}$$

where $Y_n(\theta,\phi)$ is the spherical harmonic of order n and $a_n(t)$ is the amplitude of the surface mode. $R(t)$ is solved from the Keller-Miksis

equation [24]:

$$\left(1-\frac{\dot{R}}{c}\right)R\ddot{R}+\frac{3}{2}\dot{R}^2\left(1-\frac{\dot{R}}{3c}\right) = \left(1+\frac{\dot{R}}{c}\right)\frac{1}{\rho}\left(p_g(t)-P_a(t)-P_0\right) + \frac{\dot{R}\dot{p}_g(t)}{\rho c}-\frac{4\nu\dot{R}}{R}-\frac{2\sigma}{\rho R}, \tag{4.7}$$

where R, $\dot{R}$, $\ddot{R}$ represent the radius, velocity, and acceleration of the bubble wall, $P_a(t)$ is the forcing pressure, P_0 is the ambient pressure, σ the surface tension, and ρ and ν the liquid density and kinematic viscosity, respectively, and c the speed of sound in water. Eq. (4.7) includes the important damping terms, such as radiation damping and viscous damping. While thermal damping is often empirically modeled by an increased viscous damping term [25, 26] in Eq. (4.7), we included thermal damping through the more physical picture introduced by Tögel and Lohse [27]. From their extended model we included the bubble hydrodynamics, the gas pressure, and the heat exchange between the gas core and the surrounding liquid. As the bubbles in our study are only weakly driven, we do not include chemical reactions of the gaseous species in the air bubble. In addition, we chose to model the gas interior to be comprised of nitrogen gas only. The internal gas pressure is given by [27]:

$$p_g(t)=\frac{NkT(t)}{V(t)-NB}-\frac{1}{2}\rho_g R\ddot{R}, \tag{4.8}$$

where N is the total number of molecules in the gas core, k is the Boltzmann constant, B is the molecular covolume. T is the temperature and V the volume of the bubble. ρ_g is the mean gas density.

Following [27] and [28], we now derive the equation for $\dot{T}(t)$ to close the set of ODE's. The global energy balance of the bubble's interior can be expressed as

$$\dot{E}=\dot{Q}-p_g\dot{V}. \tag{4.9}$$

Here $\dot{E}$ is the change of total energy, and $\dot{Q}$ is the conductive heat loss, given by

$$\dot{Q}=4\pi R^2\lambda_{mix}\frac{T_0-T}{l_{th}}. \tag{4.10}$$

Here, λ_{mix} is the heat conductivity, T_0 is the liquid temperature at the bubble wall and l_{th} is the thickness of thermal boundary layer, estimated by

$$l_{th}=\min\left(\sqrt{\frac{R\chi_{th}}{|\dot{R}|}},\frac{R}{\pi}\right), \tag{4.11}$$

where χ_{th} is the thermal diffusivity. The total energy E is

$$E = e_{th}N, \tag{4.12}$$

where e_{th} equals the thermal energy per molecule, which is

$$e_{th} = \frac{f}{2}kT + \frac{k\Theta}{\exp(\Theta/T) - 1}. \tag{4.13}$$

Here, f is the number of translational and rotational degrees of freedom (which is 5 for nitrogen), and Θ is the characteristic vibrational temperature (which is 3350 K for nitrogen).

Taking the time derivative of Eq. (4.12), inserting this together with Eq. (4.10) into Eq. (4.9) leads to the differential equation for the temperature:

$$\dot{T} = \frac{4\pi R^2 \lambda_{mix} \frac{T_0 - T}{l_{th}} - \left[\frac{NkT}{V - NB} - \frac{1}{2}\rho_g R\ddot{R}\right]}{\left[\frac{5}{2}k + \frac{k\Theta^2 \exp\left(\frac{\Theta}{T}\right)}{\left(\exp\left(\frac{\Theta}{T}\right) - 1\right)^2 T^2}\right] N}. \tag{4.14}$$

Equations (4.7), (4.8) and (4.14) lead to a system of four first order ordinary differential equations for R, $\dot{R}$, $\ddot{R}$ and T. This set of ODE's was then solved numerically with a stiff differential solver of variable order (Matlab ODE15s, The Mathworks).

Following the same spirit of the classical derivation of the Rayleigh–Plesset equation a dynamical equation for the distortion amplitude $a_n(t)$ can be derived [10, 12, 18]:

$$\ddot{a}_n + B_n(t)\dot{a}_n - A_n(t)a_n = 0, \tag{4.15}$$

with

$$A_n(t) = (n-1)\frac{\ddot{R}}{R} - \frac{\beta_n \sigma}{\rho R^3} + \frac{2\nu\dot{R}}{R^3}\left(-\beta_n + \frac{n(n-1)(n+2)}{1 + 2\delta/R}\right), \tag{4.16}$$

$$B_n(t) = \frac{3\dot{R}}{R} + \frac{2\nu}{R^2}\left(-\beta_n + 2\frac{n(n+2)^2}{1 + 2\delta/R}\right), \tag{4.17}$$

where $\beta_n = (n-1)(n+1)(n+2)$. Equations (4.16) and (4.17) follow from a simple boundary layer approximation, which assumes the vorticity to be localized in a thin region around the bubble, see [11, 12]. The size of the boundary layer thickness δ was taken as the minimum of the diffusive length scale and the wavelength of the shape oscillation $R/(2n)$. The ordinary differential equation (4.15) was then solved together with

Eq. (4.7) to give the distortion amplitude as a function $a_n(t)$ for each mode n. A small distortion was imposed to the differential equation of the shape oscillations as an initial condition. The initial distortion will decay if the system is driven below threshold. Vice versa, the surface mode will grow rapidly when driven above the threshold of the instability. In the calculations presented here the initial distortion was taken to be 1 nm, in the order of 10^{-4} of the ambient radius of the bubble. We note that the choice of the size of the initial distortion is arbitrary as we only consider a fully linear perturbation model for the shape instability. Therefore, without any knowledge of the initial condition, the absolute amplitude of the resulting shape deformation cannot be inferred from the model.

4.5 Results

The radial oscillations for a 30 μm radius bubble driven with a burst of 10 cycles of 130 kHz at a pressure of 80 kPa (see Fig. 4.4A) is given in Fig. 4.4B. The results of dynamical equations for the distortion amplitude is given in Fig. 4.4C. The graph displays the development over time of the shape oscillations for mode n = 2 to 7. Fig. 4.4D shows the growth of the shape oscillations in a log-linear scale. It is seen that the mode n = 3 grows exponentially while other modes are hardly excited. The finite length of the ultrasound pulse stops further growth. The surface modes then decay exponentially with a decrease proportional to the power n each at a surface mode natural frequency following Eq. (4.1). Two similar results are shown for bubbles of radius 35 μm and 45 μm, respectively. Fig. 4.4G shows the development of a single mode n = 4; also mode n = 3 is visible. Fig. 4.4K shows how a dominant mode n = 5 develops, while a mode n = 6 shows an onset of a possible instability, but not nearly as strong as the dominant mode.

Note the striking comparison between the simulations in Fig. 4.4H and the experimental recordings in Fig. 4.2G. The experiments were done on a bubble with a 33 μm radius, while the radius of the bubble in the simulations was 35 μm. In both cases, the mode number 4 was dominant. The growth and decay part of the curve is similar.

The above calculations are now repeated for a complete parameter range as a function of the ambient bubble radius R_0 and the forcing pressure P_a. The bubble radius was varied from 10 to 60 μm in 0.25 μm intervals; the pressure was varied from zero to 175 kPa in 1 kPa incremental steps. The results of these 35 000 calculations were then combined in

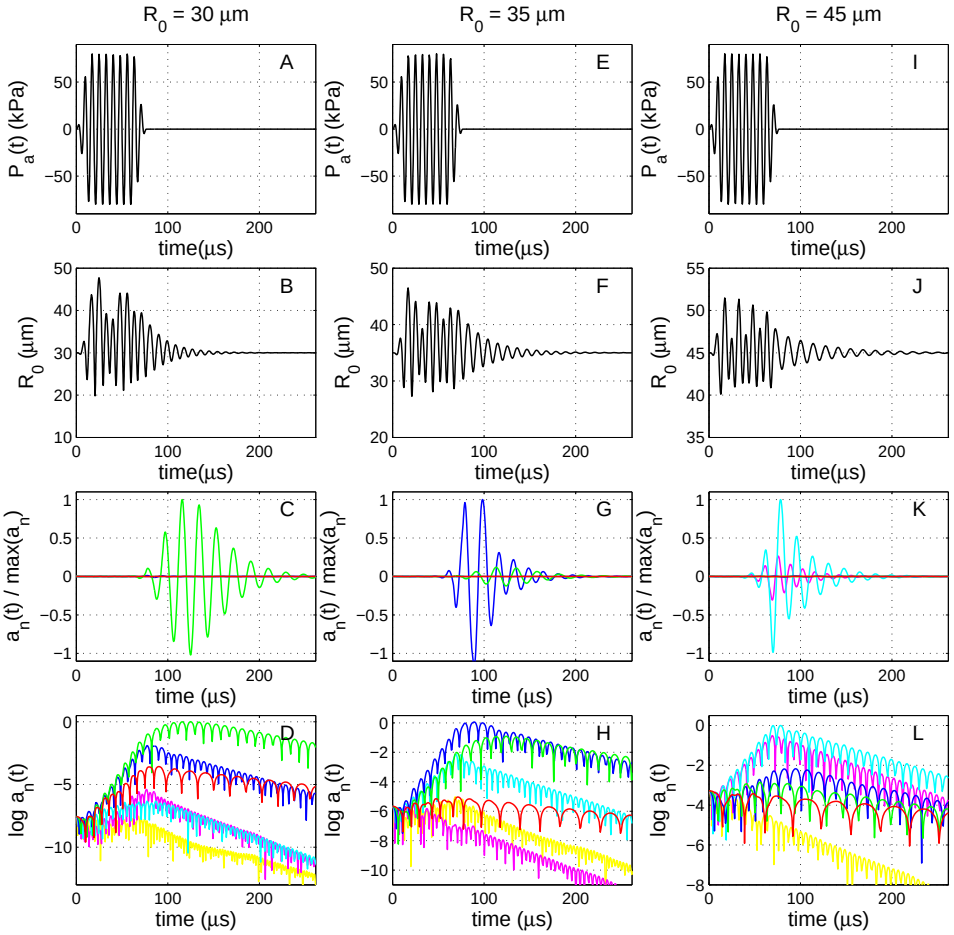

Figure 4.4: Numerical simulation of the onset of the shape oscillation. (A) An ultrasound pulse of 10 cycles of 130 kHz at a driving pressure of 80 kPa. (B) The radial response of a 30 μm bubble. (C) Mode amplitude a_n for $n = 2$ tot 7 as function of time t. The color coding indicates the mode: red - mode 2, green - mode 3, blue - mode 4, turquoise - mode 5, magenta - mode 6, and yellow - mode 7. The mode $n = 3$ is the most unstable one. (D) The same result plotted on a log-linear scale showing the growth of a single dominant mode. The growth stops as soon as the parametric driving stops, followed by an amplitude decrease and shape oscillation frequency characterized by the corresponding mode number n. Since the absolute amplitude of the resulting shape deformation cannot be inferred from the model, all mode amplitudes were normalized by the maximum value of all $a_n(t)$. E-H: Similar calculations for a 35 μm bubble, where $n = 4$ is the most unstable mode. I-L: Here R_0=45 μm. Now mode 5 is the most unstable one.

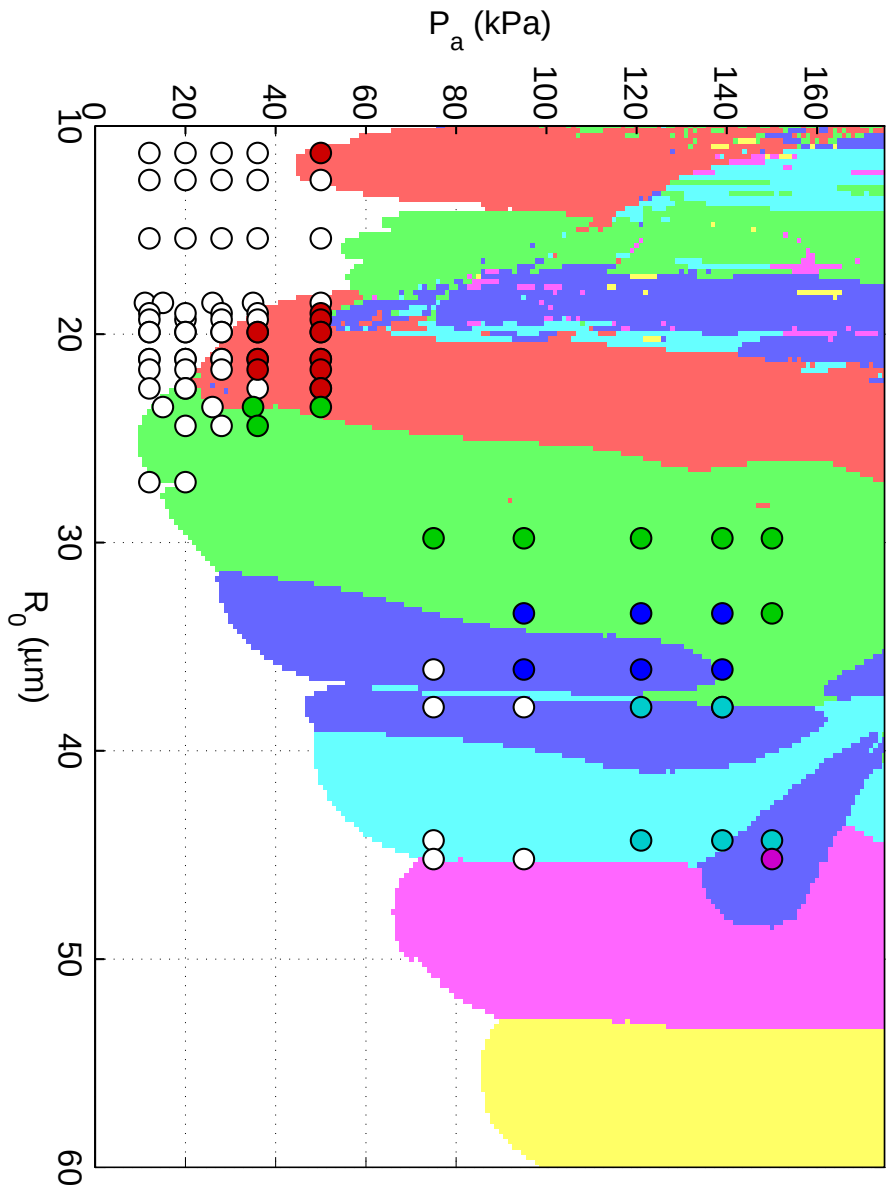

Figure 4.5: Numerical radius–pressure diagram. The threshold for surface mode vibrations is set to 10% of R_0. The color coding indicates a specific mode preference: white - below threshold, red - mode 2, green - mode 3, blue - mode 4, turquoise - mode 5, magenta - mode 6, and yellow - mode 7. Experimental data points are included using the same color coding.

a diagram of the complete parameter space (see Fig. 4.5) where the radius R_0 is plotted on the horizontal axis and the applied ultrasound pressure P_a on the vertical axis. The numerical data points are classified in color coding following their mode preference, i.e., the mode number with the dominant distortion.

We also include in Fig. 4.5 the experimental data on surface mode vibrations following the same color coding. We see that the correspondence is very good. In the fully linear model the choice for the threshold cannot be other than quite arbitrary. Bubbles that did not show a surface mode vibration in the experiments are indicated by a white dot. These data points were used to specify a threshold value for surface mode vibrations in the radius–pressure diagram, here at 10% of the ambient bubble radius. This means that the amplitude of the shape instability needs to grow by at least two orders of magnitude in order to be included in the radius–pressure diagram. We observe that the forcing pressure threshold for surface mode vibrations has its minimum value at an ambient radius of 25.1 μm, which, as expected, very well coincides with the resonance radius of the natural volumetric oscillation when driven at 130 kHz frequency following the classical expression by Minnaert [29]:

$$f_M = \frac{1}{2\pi}\sqrt{\frac{3\gamma P_0}{\rho R_0^2}}, \tag{4.18}$$

where γ is the polytropic exponent. We neglect the surface tension in this equation. We note that the pressure amplitude threshold for shape oscillations is for bubbles with a radius near the volumetric resonance radius less dependent on the choice of threshold value.

From the radius–pressure diagram it also follows that the mode preference for a given ambient bubble radius is hardly influenced by the forcing pressure. Furthermore, we observed that from the numerical simulations the instability can grow beyond the resting radius of the bubble. In the physical case such a bubble would split up, as observed in experiment. It is interesting to see that the number of initial fragments is directly related to the mode number. Fig. 4.6, for example, shows a bubble that exhibits a mode n = 3 surface mode vibration and splits up into three fragments. The fragmentation continues, theoretically following a cubic dependence of the mode number n [30], here into 27 fragments. In our setup the total number of bubble fragments cannot be tracked quantitatively as there is a fair amount of optical shielding.

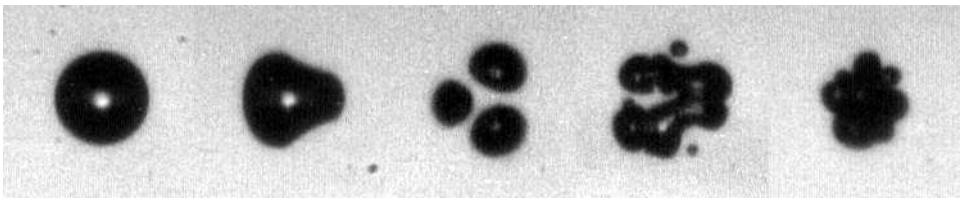

Figure 4.6: Splitting of a shape-unstable bubble in mode $n = 3$. Three fragments are split off.

4.6 Conclusions

In conclusion, we have seen that a bubble can become shape-unstable through a parametric instability. The experimental recordings of shape oscillating micrometer sized bubbles, ranging from 10 to 60 μm in radius, were supported by a model which introduced a small non-spherical linear perturbation into a Rayleigh–Plesset type equation. The observed mode number n (from 2 to 6) was found to be linearly dependent on the bubble radius R_0, and independent of the acoustic forcing pressure P_a. A driving pressure threshold for the occurence of the shape instability was found, which was minimum for the resonance radius of 25.1 μm, corresponding with the acoustic frequency of 130 kHz.

References

[1] P. L. MARSTON, S. G. GOOSBY, "Ultrasonically stimulated low-frequency oscillation and breakup of immiscible liquid drops: Photographs", Phys. Fluids **28**, 1233–1242 (1985).

[2] T. S. LUNDGREN, N. N. MANSOUR, "Oscillations of drops in zero gravity with weak viscous effects", J. Fluid Mech. **194**, 479–510 (1988).

[3] O. A. BASARAN, "Nonlinear oscillations of viscous liquid drops", J. Fluid Mech. **241**, 169–198 (1992).

[4] R. E. APFEL, Y. TIAN, J. JANKOVSKY, T. SHI, X. CHEN, R. GLYNN HOLT, E. TRINH, A. CROONQUIST, K. C. THORNTON, A. SACCO JR., C. COLEMAN, F. W. LESLIE, D. H. MATTHIESEN, "Free Oscillations and Surfactant Studies of Superdeformed Drops in Microgravity", Phys. Rev. Lett. **78**, 1912–1915 (1997).

[5] A. PROSPERETTI, "Free oscillations of drops and bubbles: the initial-value problem", J. Fluid Mech. **100**(2), 333–347 (1980).

[6] T. G. LEIGHTON, *The Acoustic Bubble*. London: Academic, (1994).

[7] M. S. PLESSET, "On the Stability of Fluid Flows with Spherical Symmetry", J. Appl. Phys. **25**(1), 96–98 (1954).

[8] E. A. NEPPIRAS, "Subharmonic and other low-frequency emission from bubbles in sound-irradiated liquids", J. Acoust. Soc. Am., **46**(3B), 587–601, (1969).

[9] A. ELLER AND L. A. CRUM, "Instability of the Motion of a Pulsating Bubble in a Sound Field", J. Acoust. Soc. Am. Suppl. **47**(3B), 762–767 (1970).

[10] A. PROSPERETTI, "Viscous effects on perturbed spherical flows", Quart. Appl. Math. **34**, 339–352 (1977).

[11] M. P. BRENNER, D. LOHSE, T. F. DUPONT, "Bubble Shape Oscillations and the Onset of Sonoluminescence", Phys. Rev. Lett. **75**, 954–957 (1995).

[12] S. HILGENFELDT, D. LOHSE, M. P. BRENNER, "Phase Diagrams for Sonoluminescing Bubbles", Phys. Fluids **8**, 2808–2826 (1996).

[13] Y. TIAN, J. A. KETTERLING, R. E. APFEL, "Direct observation of microbubble oscillations", J. Acoust. Soc. Am. **100**(6), 3976–3978 (1996).

[14] E. H. TRINH, D. B. THIESSEN, R. G. HOLT, "Driven and freely decaying nonlinear shape oscillations of drops and bubbles immersed in a liquid: experimental results", J. Fluid Mech. **364**, 253–272 (1998).

[15] Y. HAO, A. PROSPERETTI, "The effect of viscosity on the spherical stability of oscillating gas bubbles", Phys. Fluids **11**(6), 1309–1317 (1999).

[16] M. KAMEDA AND Y. MATSUMOTO, "Nonlinear oscillation of a spherical gas bubble in acoustic fields", J. Acoust. Soc. Am. **106**, 3156–3166 (1999).

[17] T. J. MATULA, "Inertial cavitation and single-bubble sonoluminescence", Phil. Trans. Roy. Soc. A **357**, 225–249 (1999).

[18] M. P. BRENNER, S. HILGENFELDT, D. LOHSE, "Single-bubble sonoluminescence", Rev. Mod. Phys. **74**, 425–484 (2002).

[19] P. PALANCHON, A. BOUAKAZ, J. KLEIN, N. DE JONG, "Subharmonic and ultraharmonic emissions for emboli detection and characterization", Ultrasound Med. Biol. **29**(3), 417–425 (2003).

[20] C. T. CHIN, C. LANCÉE, J. BORSBOOM, F. MASTIK, M. E. FRIJLINK, N. DE JONG, M. VERSLUIS, D. LOHSE, "Brandaris 128: A digital 25 million frames per second camera with 128 highly sensitive frames", Rev. Sci. Instrum., **74**(12), 5026–5034 (2003).

[21] M. SONKA, V. HLAVAC, R. BOYLE, *Image processing, analysis, and machine vision*, 2nd ed. Pacific Grove, CA: PWS Pub., (1999).

[22] H. LAMB, *Hydrodynamics*, 6th ed. Cambridge: Cambridge University Press, (1932).

[23] A. FRANCESCUTTO, R. NABERGOJ, "Pulsation amplitude threshold for surface waves on oscillating bubbles", Acoustica **41**, 215–220 (1978).

[24] J. B. KELLER, M. MIKSIS, "Bubble oscillations of large amplitude", J. Acoust. Soc. Am. **68**(2), 628–633 (1980).

[25] C. DEVIN JR., "Survey of Thermal, Radiation, and Viscous Damping of Pulsating Air Bubbles in Water", J. Acoust. Soc. Am. **31**(12), 1654–1667 (1959).

[26] H. MEDWIN, "Counting bubbles acoustically: a review", Ultrasonics **15**(1), 7–13 (1977).

[27] R. TOEGEL, D. LOHSE, "Phase diagrams for sonoluminescing bubbles: A comparison between experiment and theory", J. Chem. Phys. **118**(4), 1863–1875 (2003).

[28] R. TOEGEL, S. HILGENFELDT, D. LOHSE, "Suppressing Dissociation in Sonoluminescing Bubbles: The Effect of Excluded Volume", Phys. Rev. Lett. **88**(3), 034301 (2002).

[29] M. MINNAERT, "On musical air-bubbles and the sounds of running water." Phil. Mag., **16**, 235–248 (1933).

[30] C. E. BRENNEN, "Fission of collapsing cavitation bubbles", J. Fluid Mech. **472**, 153–166 (2002).

5

Nonspherical oscillations of ultrasound contrast agent microbubbles[§]

The occurrence of nonspherical oscillations (or surface modes) of coated microbubbles, used as ultrasound contrast agents in medical imaging, is investigated using ultra-high-speed optical imaging. Nonspherical oscillations appear as a parametric instability, and display subharmonic behavior: they oscillate at half the forcing frequency, which was fixed at 1.7 MHz in this study. With the definition of a single, dimensionless deformation parameter, the amplitude of nonspherical deformation is quantified as a function of the bubble radius (between 1.5 and 5 μm) and of the acoustic pressure (up to 400 kPa). Surface modes are shown to preferentially develop for a bubble radius close to the resonance of radial oscillations. Using optical tweezers designed to fully trap and micromanipulate single bubbles in 3D, the magnitude of nonspherical deformation is compared for free-floating bubbles and for bubbles in contact with a wall. In the studied range of acoustic pressures, the growth of surface modes saturates at a level far below bubble breakage. The medical relevance of these nonspherical oscillations, in relation with potential subharmonic acoustic emission, is discussed.

5.1 Introduction

Ultrasound Contrast Agents (UCA) are solutions of encapsulated bubbles of a few micron in radius. They are used in ultrasound imaging to enhance

[§]Based on: Benjamin Dollet, Sander van der Meer, Nico de Jong, Michel Versluis, Detlef Lohse, "Nonspherical oscillations of ultrasound contrast agent microbubbles", submitted to Ultrasound Med. Biol.

the contrast between the blood pool and the surrounding tissue, thanks to the very high echogenicity of the microbubbles [1]. Tissue reflects sound mainly at the fundamental frequency, therefore in practice ultrasound imaging modalities aim at using nonlinear backscattering properties of the microbubbles to enhance the contrast between blood and tissue [2, 3]. One of the simplest modalities consists in receiving higher harmonic ($2f$, $3f$, ... where f is the insonifying frequency), subharmonic ($f/2$), or ultraharmonic ($3f/2$) echoes from the bubbles. Among these nonlinear components, the subharmonic response offers several advantages. First, it displays a better blood-tissue contrast than the second harmonic [4–6]. Second, for high transmit frequency (typically 20 to 40 MHz), it gives a stronger signal than higher harmonics and ultraharmonics [7], and is less sensitive to attenuation and nonlinear propagation, which makes subharmonic imaging a promising modality for intravascular imaging [8]. However, the physical origin of the subharmonic component, and its dependence on the applied pressure and frequency remains unclear [5].

To understand the origin of the sound scattered by UCA microbubbles, all existing models have focused on describing the spherical oscillations of coated bubbles (see e.g. [9–14]). However, it is well known for uncoated bubbles of bigger size that spherical oscillations become unstable above a threshold in acoustic forcing. The onset of nonspherical deformation has been predicted by various theoretical studies [15–22] and directly observed for bubbles for radii between 10 μm and 1 cm [23–25]. As a salient feature, these nonspherical oscillations, or surface modes, display a strong subharmonic behavior with respect to the forcing frequency, which can be understood in terms of a parametric resonance.

Based on direct observations using high-speed imaging, there has been some evidence that UCA microbubbles can exhibit nonspherical shapes [26–28], and that they can display subharmonic behavior [26]. However, no systematic study of the nonspherical oscillations has yet been proposed. A major difficulty of such a study is that the bubbles stand against the top wall of the setup because of buoyancy, and the vicinity of a wall influences greatly the nonspherical oscillations of the bubbles [27, 28]. To overcome this difficulty, 3D micromanipulation using optical tweezers has recently been proposed. This technique has proven to be a very versatile tool to trap single or multiple UCA microbubbles and control precisely their position, revealing the great influence of the wall on their radial oscillations [29]. In this paper, we combine this 3D optical micromanipulation with ultra-high-speed imaging, to study the occurrence of nonspherical oscillations of UCA microbubbles.

5.2 Materials and methods

5.2.1 Experimental setup

The experimental setup (see Fig. 5.1) is similar as the one described in [29]. A solution of the experimental contrast agent BR-14 (Bracco Research S.A., Geneva, Switzerland), containing bubbles coated by a phospholipid monolayer, is prepared and injected through an optically and acoustically transparent chamber (OptiCell, BioCrystal, Inc.) immersed in water. The bubbles are illuminated from below with an optical fiber and an image is produced by an upright Olympus microscope with a $100\times$ water-immersed objective (LUMFPL, Olympus; NA = 1.0) and a $2\times$ magnifier. Bright-field transmission imaging is performed through the same objective. A Gaussian beam from a 1064 nm continuous wave Yb fiber laser (YLM, IPG Photonics) is converted into a Laguerre-Gaussian mode by a phase diffractive optical element (DOE) [30] implemented on a spatial light modulator (SLM) (X8267-11, Hamamatsu). This conversion enables us to trap particles of lower refractive index than the surrounding medium, like microbubbles in water [30, 31]. The beam is coupled into the microscope and focused on the OptiCell by the $100\times$ objective. The trapped bubble can be positioned at a prescribed distance from the wall using a micropositioning stage. The ultra-high-speed Brandaris camera [32] is directly connected to the imaging port of the microscope and records the bubble oscillations during ultrasonic insonation at 14 million frames per second.

The optical focus matches with the acoustical focus of a broadband single element transducer (PA081, Precision Acoustics, Dorchester, UK) with a center frequency of 1.7 MHz and a calibrated range of frequencies from 0.7 to 6 MHz. The transducer is mounted at an angle of 45° with respect to the optical axis. An arbitrary waveform generator (AWG), a Tabor 8026 (Tabor Electronics, Tel Hanan, Israel), connected to a PC, was used to produce waveforms, which were then amplified by an ENI 350L amplifier. The programming of the waveforms was performed in Matlab (The Mathworks). The waveforms were transferred to the AWG via a GPIB interface. The length of the ultrasound waveforms was 12 cycles at a fixed frequency $f = 1.7$ MHz, of which the first two and the last two were tapered with a Gaussian envelope.

5.2.2 Insonation protocol

We scan regions of the OptiCell not previously subjected to ultrasound with two horizontal micropositioning stages, to find single isolated bubbles. Due to buoyancy, the bubbles float against the top wall of the cell. Some bubbles adhere to the wall; we study only nonadherent bubbles, by checking that they are repelled by the outer circumference of the Laguerre-Gaussian laser beam. The bubble insonation protocol is as follows. First, without optical trap, the bubble is subjected to a scan of six different acoustic pressures, from 0 to $5P_0$ by regular steps of P_0, the first sequence being a reference without insonation to measure the equilibrium bubble radius. We used different step values P_0, from 40 to 80 kPa; the highest investigated pressure is thus 400 kPa. This corresponds to a maximal Mechanical Index M.I. $= 0.31$. During each pulse, the bubble oscillation is recorded with the ultra-high-speed Brandaris camera, which in these experiments records six movies of 128 frames each, with one movie per pressure level. Second, we trap the bubble, and position it at a distance of 50 ± 5 μm from the wall, which is sufficient for the wall influence on the bubble dynamics to be negligible: these bubbles are

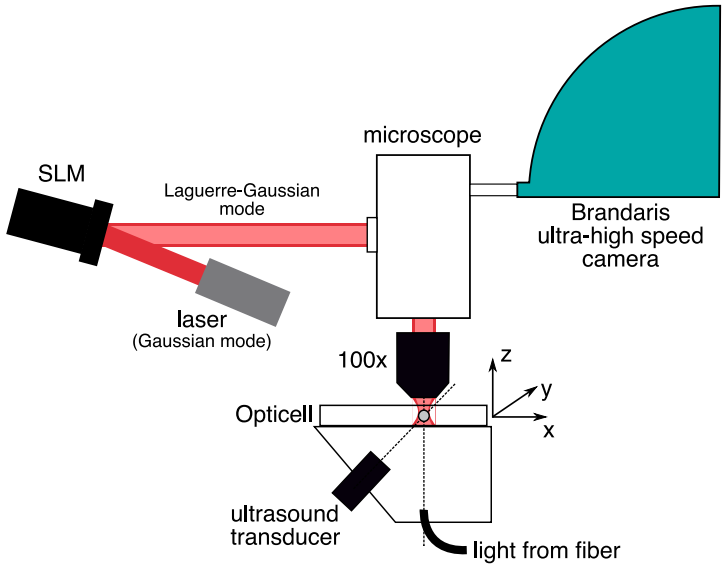

Figure 5.1: Overview of the experimental setup. The x, y, z arrows figure the 3D micropositioning stage.

freely floating. We then insonify the bubble as before, the optical trap being momentarily switched off during insonation to avoid any possible influence on the bubble oscillations. Third, we bring back the bubble in contact with the top wall of the cell, check again if it is non-adherent, and insonify it as before.

We discard the bubbles that break during insonation: the breakage of a bubble is followed by its progressive dissolution, which is easy to detect from its decreased radius. In total, we studied 40 bubbles. We do not present measurements for bubbles smaller than 1.9 μm: at the frequency of 1.7 MHz, we hardly observed oscillations for these bubbles, likely owing to the "thresholding" behavior previously reported for the same bubbles below resonance [33].

5.3 Results

Typical examples of the nonspherical shapes of the bubbles during insonation are displayed in Fig. 5.3. In two cases (Fig. 5.3A and B), the bubble shape shows a clear surface mode, characterized by regular "bumps", which number is called the mode number (mode 3 in Fig. 5.3A, mode 4 in Fig. 5.3B). On the other hand, Fig. 5.3C and D show more irregular shapes, combinations of different surface modes. We will now present a systematic study of these nonspherical shapes, first focusing on individual surface modes (Sec. 5.3.2 and 5.3.3) then on a global nonspherical deformation quantified by a single deformation parameter (Sec. 5.3.4).

5.3.1 Image analysis

The image analysis, entirely programmed with Matlab, is performed as illustrated in Fig. 5.3. First, we apply a threshold to the images (Fig. 5.3A) to identify the bubble contour. The threshold level was chosen as the average of the grey levels of the background and of the darkest grey level of the bubble; this choice reproduces the bubble contour with a precision on the radius better than 5% (Fig. 5.3B). We then identify the bubble center as the center of mass of the surface enclosed by the contour, and from this point we measure the angular dependence of the radius $R(\theta)$, and calculate its difference $\delta(\theta) = R(\theta) - R_{\text{mean}}$ with the mean radius $R_{\text{mean}} = \frac{1}{2\pi}\int_0^{2\pi} R(\theta)\mathrm{d}\theta$ (Fig. 5.3C). The bubble shows a nonspherical shape if the value of $\delta(\theta)$ deviates significantly from zero.

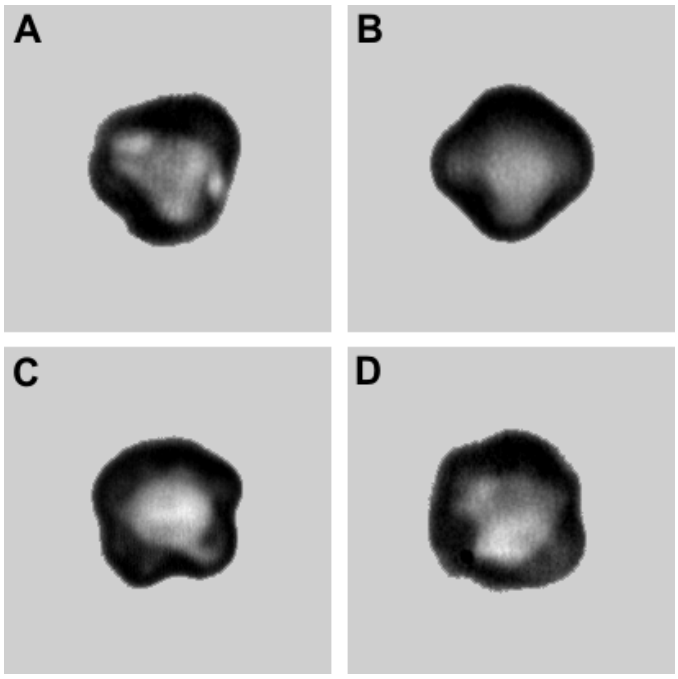

Figure 5.2: Snapshots of surface modes experienced by UCA microbubbles. A and B show clearly identifiable modes (3 and 4), whereas C and D display examples where nonspherical deformation is the result of a mixing of different modes.

A classical way to study nonspherical deformation is the decomposition into surface modes [34]. In the most common case where the bubble shape has an axis of symmetry, each surface mode is indexed by a single integer which quantifies the number of "bumps" along the bubble contour (Figs. 5.3A and B). To identify the amplitude and the number of the modes, we calculate the Fourier transform of $\delta(\theta)$:

$$\hat{\delta}(n) = \frac{1}{2\pi}\int_0^{2\pi} \delta(\theta) e^{in\theta} \mathrm{d}\theta,$$

using a Fast Fourier Transform (FFT) algorithm, and we then identify the value of the Fourier spectrum at each integer value of n as the absolute value of the amplitude of mode n: $|a_n| = \sqrt{\hat{\delta}(n)\hat{\delta}(n)^*}$, where $*$ stands for complex conjugation (Fig. 5.3D). Note that this 2D definition of the surface mode amplitude differs from the usual 3D definition, where the bubble surface is decomposed in Legendre polynomials: $R(\theta,t) =$

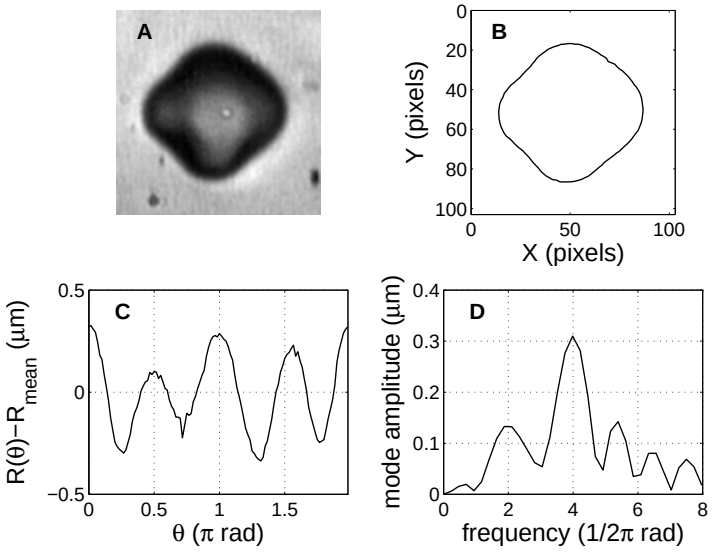

Figure 5.3: Procedure used for the data analysis. A: image of a bubble of radius 3.6 μm recorded with the camera. B: extracted profile of the bubble after thresholding image A. C: angular variation $\delta(\theta) = R(\theta) - R_{\text{mean}}$, difference between the distance from the bubble center to the interface and the mean bubble radius. D: Fourier spectrum (see text for details) of $\delta(\theta)$, used to determine the amplitude of the various modes.

$R_0(t) + \sum_{n=1}^{+\infty} a_n^{3D}(t) P_n(\cos\theta)$ (with the common assumption of axisymmetry around the axis $\theta = 0[\pi]$). We have chosen the 2D definition because we observed no preferential orientation for the deformation.

To compare the results on different bubbles, which will be done in Sec. 5.3.3 and 5.3.4, we subtracted for each mode the background noise level determined from the first images, when no oscillations have started yet, and we then performed time integration during the insonation pulse. Finally, although most of this paper focuses on nonspherical deformations, we will need to compare the magnitude of spherical and nonspherical oscillations in Sec. 5.4.1. For this, we define a relative radial amplitude as the standard deviation of R_{mean} during the ultrasonic pulse.

5.3.2 Subharmonic and saturation behaviors

A typical example of the driving pulse, the radial response of a bubble, and its single mode response, is shown in Fig. 5.4. This figure shows a major difference between radial and nonspherical oscillations: whereas

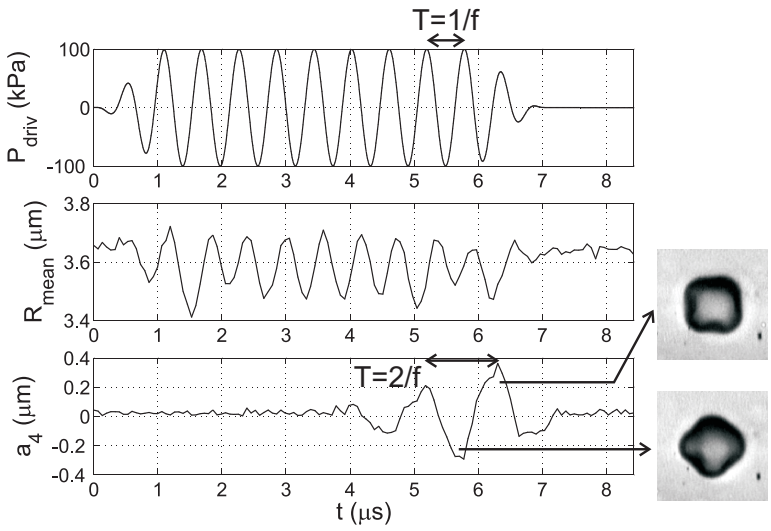

Figure 5.4: Example of experimental recording (bubble of initial radius 3.6 μm). Top: applied acoustic pressure (here, a 12-cycle burst of amplitude 100 kPa and frequency 1.7 MHz, tapered with a 2-cycle Gaussian envelope at the beginning and end). Middle: radius-time curve reconstructed from the movie of 128 images at frame rate 15 MHz. Bottom: evolution of mode 4, obtained as explained in Fig. 5.3. To show clearly the subharmonic behavior, we have unwrapped the $|a_4|(t)$ curve.

the radial oscillations are forced at the driving frequency (even though it displays the nonlinear "compression–only" behavior [35]), the nonspherical oscillations are at half the driving frequency. It was found that this is the case for all observed surface modes, irrespective of mode number, bubble radius, or applied pressure amplitude.

We also observe in Fig. 5.4 that the surface modes appear only after a few periods of radial oscillations and keep growing until the pulse ends. On the other hand, Fig. 5.5 shows another example of an experimental recording with a clear saturation, contrary to Fig. 5.4. It is interesting to know whether the surface modes keep growing along insonation, which could lead to controlled splitting of the bubbles, or whether they saturate. We address this question on the 17 recordings which show the highest surface mode amplitude, because they are the most likely to split. Among these 17 recordings, 13 showed mode saturation, and at a level insufficient for the bubbles to split (we always observed $a_n < 0.5$ μm and $a_n/R_0 <$ 25%, where R_0 is the equilibrium radius). The studied range of acoustic

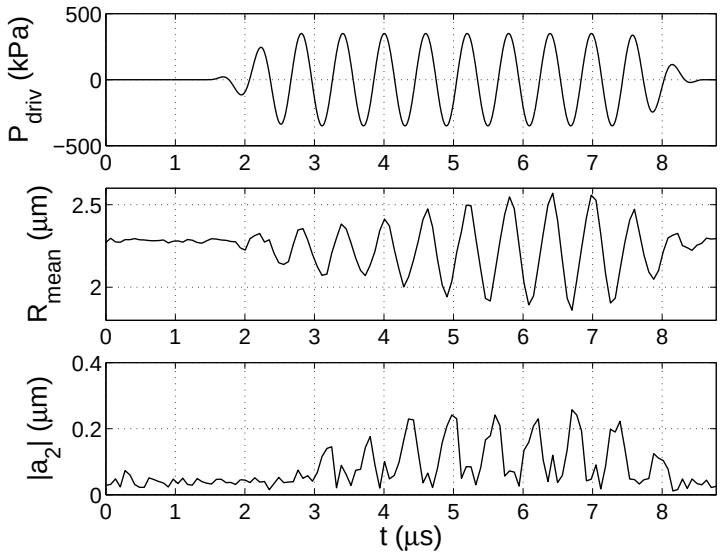

Figure 5.5: Illustration of the saturation of a surface mode. Top: applied acoustic pressure; middle: radius-time curve; bottom: evolution of mode 2, which saturates after about 4 cycles (here, the curve is not unwrapped, contrary to Fig. 5.4).

pressure ($\leq$ 400 kPa) seems therefore too low for bubble splitting to occur, whereas it has been observed at higher pressures [36]. However, we did observe breakage of bubbles through a different mechanism [37]: a loss of gas during insonation, followed by a slow deflation (on a timescale of a few tens of seconds) during which the bubble acquires a very distorted shape. We associate this behavior to the creation of defects (points or line) within the shell during insonation, through which gas escapes.

To conclude this Subsection, it is worth remarking that all existing theoretical studies describe the surface mode dynamics of uncoated bubbles [15–22] as a linear ODE for a_n. This is incompatible with a saturation behavior, which is intrinsically the signature of a nonlinear behavior of the shell. Modeling mode saturation is therefore an open challenge, which may help to understand more precisely the influence of the shell on the dynamics of UCA microbubbles.

5.3.3 Dependence on mode number, bubble radius and acoustic pressure

After the description of the salient features of surface modes for single bubbles, we now turn to a global study of the surface modes. In this Subsection, we study the relative amplitude of single modes: $|a_2|/R_0$, $|a_3|/R_0$ and $|a_3|/R_0$ in the diagram bubble radius *versus* applied acoustic pressure.

There are significant fluctuations between different bubbles, even if they are of nearly equal size and insonified with the same amplitude. Since we carefully define a reproducible protocol to insonify each bubble (see Sec. 5.2.2), we can attribute these fluctuations to small but intrinsic changes in shell composition or structure. In order to obtain less noisy trends, and since we have a big number of data points, we meshed the diagram by a regular grid of 7×7 rectangles, and ascribe to each rectangle the value $|a_n|/R_0$ obtained after averaging over the different data points present to the considered rectangle. We present the obtained results for the free-floating bubbles in Fig. 5.6 for the modes 2, 3 and 4.

These plots show a big similarity between the different modes: at a given bubble radius, the amplitude tends to increase with the applied acoustic amplitude, as expected. Moreover, all modes exhibit a maximum amplitude for a radius close to 2.5 μm and for pressures higher than 300 kPa, and a secondary maximum in amplitude for a radius close to 3.7 μm and a pressure close to 250 kPa, and have a comparable amplitude. This shows that for UCA microbubbles, contrary to uncoated bubbles [25], the different surface modes do not develop separately. To account for this, we now analyse the nonspherical oscillations through a single deformation parameter: such an analysis is simpler, and sufficient to localize the regions of maximal deformation in a diagram bubble radius *versus* acoustic pressure.

5.3.4 Deformation parameter

We define the deformation parameter α as the standard deviation of $\delta(\theta)$, rescaled by R_{mean} (see Sec. 5.3.1):

$$\alpha = \frac{1}{R_{\text{mean}}} \left[\frac{1}{2\pi} \int_0^{2\pi} \delta(\theta)^2 \mathrm{d}\theta \right]^{1/2}. \tag{5.1}$$

This parameter is dimensionless, equal to zero for a spherical bubble, and increases for increasing nonspherical deformation.

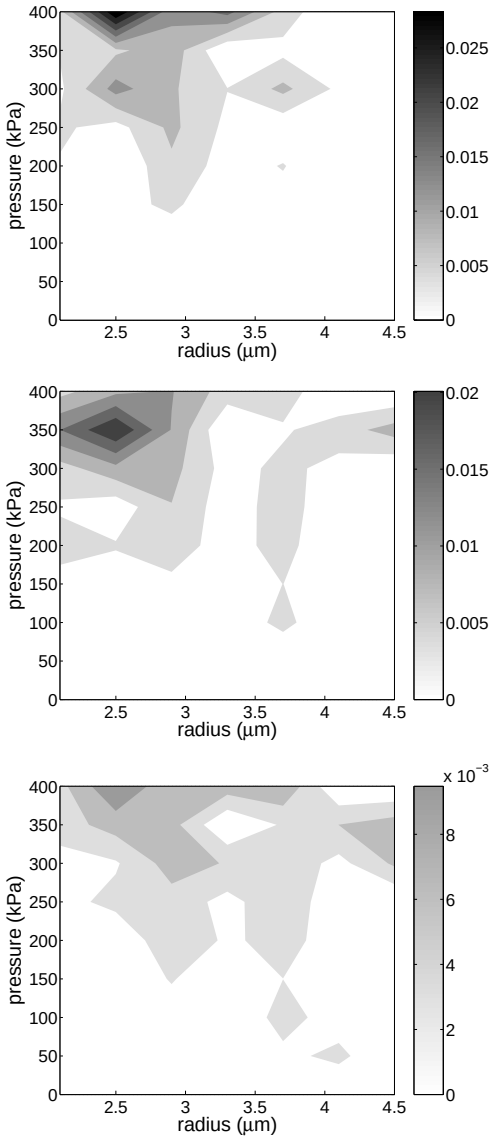

Figure 5.6: From top to bottom, amplitude of modes 2, 3 and 4, as functions of the bubble radius (horizontal scale), and of the acoustic pressure (vertical scale), for free-floating bubbles. The color code quantifies $|a_n|/R_0$: the bigger this quantity, the darker the color. The precise correspondence between grey levels and $|a_n|/R_0$ appears on the color bar at the right of each plot, and the absolute scale is the same for the three plots: notice that the amplitude of mode 4 is lower than modes 2 and 3.

Like the surface modes (Sec. 5.3.1), we perform time integration of the deformation parameter during the ultrasonic pulse to compare different bubbles, and we plot the deformation parameter as a function of the bubble radius and of the acoustic pressure, in Fig. 5.7. We recover the trends already observed on single modes (Fig. 5.6), with less noise: the deformation increases with increasing acoustic pressure, and the region of maximum deformation is centered around a radius of 2.5 to 3 μm, with a small secondary maximum at a radius of 3.7 μm. The maximum observed deformation remains lower than 3%; though this value slightly underestimates the real deformation because we subtracted the noise level, it shows again that the UCA microbubbles reach far too small deformation to undergo splitting.

5.4 Discussion

5.4.1 Nonspherical oscillations: a parametric instability

We showed in Sec. 5.3.2 that surface modes display a robust subharmonic behavior, and require a finite time to fully develop. These are generic features of a parametric instability: surface modes are not excited directly by the applied ultrasound, but are rather driven by the radial oscillations, whether the bubble is coated or not.

Francescutto and Nabergoj [18] have first analyzed theoretically the surface modes of bubbles as a parametric instability, expressing the amplitude threshold of the radial oscillations required for the instability to develop. They considered uncoated bubbles, for which the eigenfrequency of a given mode n is known [38]:

$$\omega_n^2 = \frac{(n-1)(n+1)(n+2)\sigma}{\rho R_0^3}, \tag{5.2}$$

with $\sigma = 72$ mN/m the surface tension, $\rho = 10^3$ kg/m^3 the volumetric mass of the liquid and R_0 the equilibrium radius. As a generic feature of parametric instabilities [39], the most unstable case, or parametric resonance, arises for :

$$\omega = 2\omega_n, \tag{5.3}$$

where $\omega = 2\pi f$ with f the frequency of the excitation, i.e. of the radial oscillations. In our range of applied pressures ($P_a \leq 400$ kPa), we observed that radial oscillations are still mainly at the applied acoustic frequency (see Figs. 5.4 and 5.5), which we thus identify as excitation frequency. The

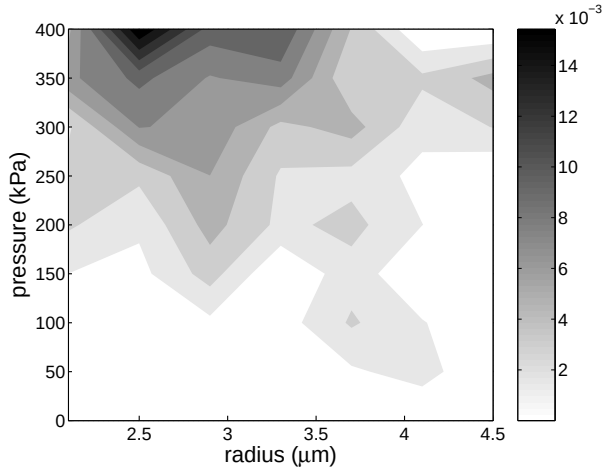

(A)

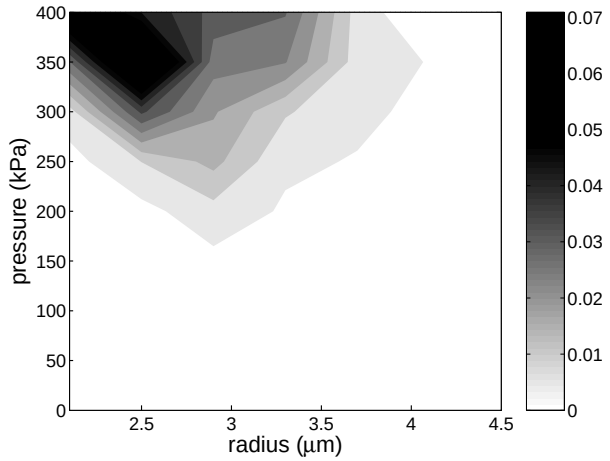

(B)

Figure 5.7: (A) Deformation parameter, as a function of the bubble radius (horizontal scale) and of the acoustic pressure (vertical scale), for free-floating bubbles. The color code quantifies the deformation parameter: the bigger this quantity, the darker the color. The precise correspondence between grey levels and the deformation parameter appears on the color bar at the right of the plot. (B) Relative radial amplitude as a function of the bubble radius (horizontal scale) and of the acoustic pressure (vertical scale), for free-floating bubbles.

condition (5.3) for parametric resonance also explains why surface modes display a strong subharmonic behavior. However, for our applied driving frequency, with the expression (5.2) of the eigenfrequency, the parametric resonance lies at a radius of 11 μm for the mode $n = 2$ and at even higher radii for modes $n \geq 3$, far out of our experimental range ($R_0 < 5$ μm).

This suggests that the expression (5.2) does not hold for the coated UCA microbubbles, for which the shell elasticity is expected to strongly affect the mode eigenfrequency, as was already shown for the eigenfrequency of radial resonance [40]. Moreover, surface modes involve not only dilatation, but also shear and bending of the membrane, and the eigenfrequency of the surface modes of coated bubbles should be a combination of the elastic parameters associated to these membrane deformations. On the other hand, we showed in Sec. 5.3.3 that the domain of instability does not vary significantly with the mode number. In other words, for UCA microbubbles, nonspherical deformations arise mainly as a mixing of modes (Fig. 5.3C and D), which is a marked difference with surface modes for uncoated bubbles [25]. In the latter case, there is a clear hierarchy of the different mode numbers in the same diagram, following closely the theoretical description of a parametric instability. These major differences between uncoated and coated bubbles call for a better theoretical description of the influence of the shell on nonspherical oscillations [41].

Up to now, we have shown that surface modes are a parametric instability, but that the domain of instability does not depend significantly on the mode number nor the bubble radius. Since a parametric instability is more likely for increasing excitation amplitude, we can expect the amplitude of nonspherical oscillations to be correlated with the amplitude of radial oscillations. To check this, we compare the average deformation parameter α, defined in Sec. 5.3.4, to the relative radial amplitude, defined in Sec. 5.3.1, and we present the diagram of this quantity calculated for the free-floating bubbles in Fig. 5.7B. It shows indeed an excellent correlation with the diagram of the deformation parameter (Fig. 5.7A), which fully supports our above argument: We therefore conclude that nonspherical oscillations develop preferentially when the bubble is at its radial resonance. Note that in a previous study [40], we measured for the frequency of 1.7 MHz a resonance radius of 3.1 μm in the regime of linear radial oscillations, at very low pressures (below 40 kPa). However, the resonance radius on Fig. 5.7B (hence for pressures higher than 300 kPa) is lower by about 20%; this difference is due to the fact that increasing the applied pressure amplitude decreases the resonance frequency, as is

already known for uncoated bubbles [42].

5.4.2 Influence of a wall

Up to now, we have studied the nonspherical oscillations of free-floating bubbles. We now plot the deformation of bubbles touching the top wall (Figs. 5.8A). As a first difference between Fig. 5.7A and 5.8A, the bubbles in contact with the wall which are most deformed are significantly smaller than free-floating ones: the maximal deformation is observed at around 2 μm. Moreover, this shift is not specific to nonspherical oscillations, but it is also observed on the spherical oscillations (compare Figs. 5.7B and 5.8B). This supports once more our view of surface modes as a parametric instability driven near the radial resonance (Sec. 5.4.1), because it is well known that the presence of a wall decreases the resonance frequency at a given radius [43] or, equivalently, decreases the resonance radius at a given frequency.

Furthermore, comparison of Figs. 5.7A and 5.8A shows that bubbles touching a wall deform much less in the imaging plane than free-floating bubbles. However, the imaging plane is parallel to the wall, hence we could not record deformations occurring in a plane perpendicular to the wall. Previous studies have shown that the presence of a wall induces strong asymmetry in bubble dynamics [27, 28], with much stronger deformations in the plane perpendicular to the wall. This asymmetry is well-known in the context of cavitation, where the collapse of bubbles in the vicinity of a wall can lead to the formation of a jet towards the wall [44–46]. Hence, our measurements underestimate the amplitude of deformation for bubbles in contact with the wall. There is no such underestimation for our trapped bubbles, which are brought far enough from the wall for its influence to be negligible. The only possible preferential direction for deformation could be the direction of ultrasonic propagation; since this direction makes an angle of 45° with respect to the imaging plane, we could track an asymmetry along the direction of propagation on our images. However, we did not observe any evidence of such an asymmetry for free-floating bubbles; hence, our method of visualization captures the relevant deformation, contrary to bubbles close to walls.

5.4.3 Acoustic emission of surface modes

We have shown that the surface modes exhibit a robust subharmonic character. They seem therefore natural candidates to explain the sub-

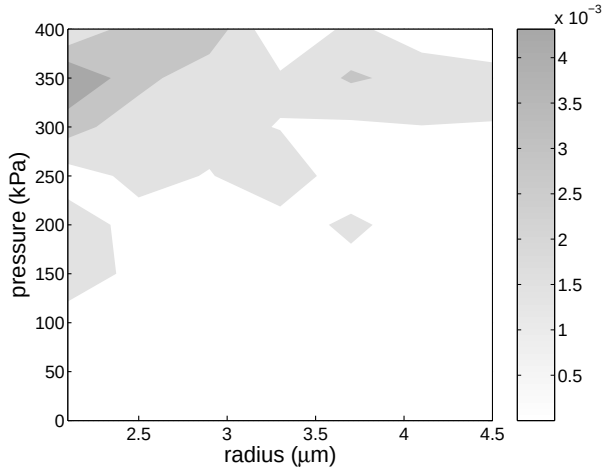

(A)

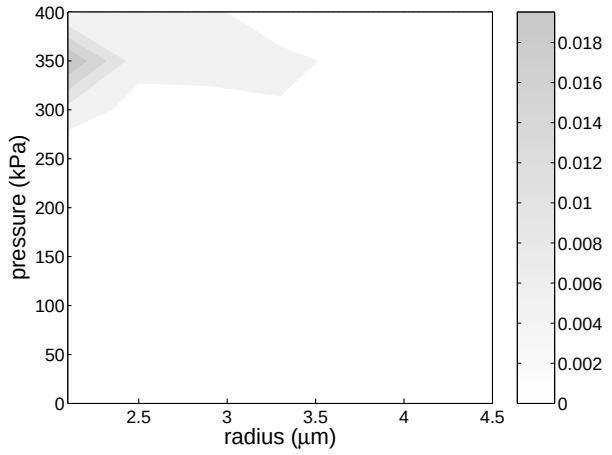

(B)

Figure 5.8: (A) Deformation parameter, as a function of the bubble radius (horizontal scale) and of the acoustic pressure (vertical scale), for bubbles touching a wall. The color code quantifies the deformation parameter: the bigger this quantity, the darker the color. The precise correspondence between grey levels and the deformation parameter appears on the color bar at the right of the plot. The absolute scale of the grey levels is the same as the diagram for free-floating bubbles (Fig. 5.7); this shows that the bubbles get less deformed when they are close to the wall. (B) Relative radial amplitude as a function of the bubble radius (horizontal scale) and of the acoustic pressure (vertical scale), for bubbles touching a wall.

harmonic sound emission from UCA microbubbles, and inducing surface modes on a controlled way could appear as a promising way to enhance subharmonic emission from UCA, which is of obvious interest for nonlinear imaging.

Longuet-Higgins predicted first the sound emission associated to nonspherical oscillations [47]. He showed that the relation between sound emission and surface modes is more subtle than for radial oscillations. Indeed, there is no bubble volume variation associated with surface modes, and since the pressure scattered in the far-field at a distance r by a bubble of volume V is related to its volume variation [34],

$$P_s(r,t) = \frac{\rho}{4\pi r}\frac{\mathrm{d}^2 V}{\mathrm{d}t^2} + \mathcal{O}\left(\frac{1}{r^2}\right),$$

there is, at first order, no sound emitted by surface modes in the far-field. However, Longuet-Higgins showed that surface modes induce a secondary volume variation, proportional to the square of the mode amplitude, and that this is related to a secondary sound emission in the far-field:

$$P_{s,n}(r,t) \propto \frac{a_n(t)^2}{r}.$$

This shows that the sound emission associated to surface modes is mainly at twice the main subharmonic frequency of a_n: hence, we expect that the main frequency contribution of this sound to be the fundamental, which would limit the interest of surface modes as a nonlinear source of sound. However, Longuet-Higgins considered the case of unforced surface modes, decoupled from radial motion and acoustic forcing, whereas in our case, surface modes are the result of a parametric forcing, and one needs to account for the coupling between acoustic forcing, radial oscillations, and surface modes to predict correctly the sound associated to surface modes (and especially its frequency content). This theoretical derivation, and its comparison to experimental sound measurements, will be described in a future study.

5.5 Conclusions

We have performed the first systematic study of nonspherical oscillations, or surface modes, of ultrasound contrast agent microbubbles, using ultra-high speed imaging. We have shown that they are significantly present in medically relevant ranges of bubble radii and applied acoustic pressures.

It was shown that nonspherical deformations are a parametric instability driven by radial oscillations: they oscillate subharmonically with respect to the applied driving frequency, they require a finite time to grow, and they develop preferentially at the resonance radius for the radial oscillations.

This study has strong implications in two directions of research. First, it motivates a deeper theoretical modeling of bubble coatings, accounting for membrane shear and bending, which in turn could be used to better understand and design UCA microbubbles. Second, the subharmonic character of nonspherical oscillations are interesting in the context of nonlinear imaging, but the outcome in terms of sound emission remains unclear at this stage: this requires further specific research.

References

[1] A. L. KLIBANOV, "Ultrasound contrast agents: Development of the field and current status", *Top. Curr. Chem.* **222**, 73–106 (2002).

[2] P. J. A. FRINKING, A. BOUAKAZ, J. KIRKHORN, F. J. TEN CATE, N. DE JONG, "Ultrasound contrast imaging: Current and new potential methods", Ultrasound Med. Biol. **26**, 965–975 (2000).

[3] W. T. SHI, F. FORSBERG, "Ultrasonic characterization of the nonlinear properties of contrast microbubbles", Ultrasound Med. Biol. **26**, 93–104 (2000).

[4] P. M. SHANKAR, P. D. KRISHNA, V. L. NEWHOUSE, "Advantages of subharmonic over second harmonic backscatter for contrast-to-tissue echo enhancement", Ultrasound Med. Biol. **24**, 395–399 (1998).

[5] P. D. KRISHNA, P. M. SHANKAR, V. L. NEWHOUSE, "Subharmonic generation from ultrasonic contrast agents", Phys. Med. Biol. **44**, 681–694 (1999).

[6] F. FORSBERG, W. T. SHI, B. B. GOLDBERG, "Subharmonic imaging of contrast agents", Ultrasonics **38**, 93–98 (2000).

[7] D. E. GOERTZ, M. E. FRIJLINK, N. DE JONG, A. F. W. VAN DER STEEN, "High frequency nonlinear scattering from a micrometer to submicrometer sized lipid encapsulated contrast agent", Ultrasound Med. Biol. **32**, 569–577 (2006).

[8] D. E. GOERTZ, M. E. FRIJLINK, N. DE JONG, A. F. W. VAN DER STEEN, "Nonlinear intravascular ultrasound contrast imaging", Ultrasound Med. Biol. **32**, 491–502 (2006).

[9] N. DE JONG, R. CORNET, C.T. LANCÉE, "Higher harmonics of vibrating gas-filled microspheres. Part one: simulations", Ultrasonics **32**, 447–453 (1994).

[10] C. C. CHURCH, "The effects of an elastic solid surface layer on the radial pulsarions of gas bubble", J. Acoust. Soc. Am., **97**, 1510–1521 (1995).

[11] L. HOFF, P. C. SONTUM, J. M. HOVEM, "Oscillations of polymeric microbubbles: Effect of the encapsulating shell", J. Acoust. Soc. Am. **107**, 2272–2280 (2000).

[12] D. B. KHISMATULLIN, A. NADIM, Radial oscillations of encapsulated microbubbles in viscoelastic liquids, Phys. Fluids **14**, 3534–3557 (2002).

[13] K. SARKAR, W. T. SHI, D. CHATTERJEE, F. FORSBERG, "Characterization of ultrasound contrast microbubbles using in vitro experiments and viscous and viscoelastic interface models for encapsulation", J. Acoust. Soc. Am. **118**, 539–550 (2005).

[14] P. MARMOTTANT, S. VAN DER MEER, M. EMMER, M. VERSLUIS, N. DE JONG, S. HILGENFELDT, D. LOHSE, "A model for large amplitude oscillations of coated bubbles accounting for buckling and rupture", J. Acoust. Soc. Am., **118**, 3499–3505 (2005).

[15] M. S. PLESSET, "On the stability of fluid flows with spherical symmetry", Appl Phys. Lett. **25**, 96–98 (1954).

[16] A. I. ELLER, L. A. CRUM, "Instability of the motion of a pulsating bubble in a sound field", J. Acoust. Soc. Am. **47**, 762–767 (1970).

[17] A. PROSPERETTI, "Viscous effects on perturbed spherical flows", Quart. Appl. Math. **35**, 339–352 (1977).

[18] A. FRANCESCUTTO, R. NABERGOJ, "Pulsation amplitude threshold for surface waves on oscillating bubbles", Acustica **41**, 215–220 (1978).

[19] M. P. BRENNER, D. LOHSE, T. F. DUPONT, "Bubble shape oscillations and the onset of sonoluminescence", Phys. Rev. Lett. **75**, 954–957 (1995).

[20] S. HILGENFELDT, D. LOHSE, M. P. BRENNER, "Phase diagrams for sonoluminescing bubbles", Phys. Fluids **8**, 2808–2826 (1996).

[21] S. GROSSMANN, S. HILGENFELDT, D. LOHSE, M. ZOMACK, "Sound radiation of 3-MHz driven gas bubbles", J. Acoust. Soc. Am. **102**, 1223–1230 (1997).

[22] M. P. BRENNER, S. HILGENFELDT, D. LOHSE, "Single-bubble sonoluminescence", Rev. Mod. Phys. **74**, 425–484 (2002).

[23] Y. TIAN, J. A. KETTERLING, R. E. APFEL, "Direct observation of microbubble oscillations", J. Acoust. Soc. Am. **100**, 3976–3978 (1996).

[24] E. H. TRINH, D. B. THIESSEN, R. G. HOLT, "Driven and freely decaying nonlinear shape oscillations of drops and bubbles immersed in a liquid: experimental results", J. Fluid Mech. **354**, 253–272 (1998).

[25] M. VERSLUIS, P. PALANCHON, D. E. GOERTZ, N. DE JONG, I. HEITMAN, S. M. VAN DER MEER, B. DOLLET, D. LOHSE, "Microbubble shape oscillations excited through an ultrasound-driven parametric instability", in preparation.

[26] M. VERSLUIS, S. M. VAN DER MEER, D. LOHSE, P. PALANCHON, D. E. GOERTZ, C. T. CHIN, N. DE JONG, "Microbubble surface modes", 2004 IEEE International Ultrasonics Symposium Proceedings.

[27] S. ZHAO, K. W. FERRARA, P. A. DAYTON, "Asymmetric oscillation of adherent targeted ultrasound contrast agents", Appl. Phys. Lett. **87**, 134103 (2005).

[28] H. J. VOS, B. DOLLET, J. G. BOSCH, M. VERSLUIS, N. DE JONG, "Non-spherical vibrations of microbubbles in contact with a wall — a pilot study at low mechanical index", submitted to Ultrasound Med. Biol.

[29] V. GARBIN, D. COJOC, E. FERRARI, E. DI FABRIZIO, M. L. J. OVERVELDE, S. M. VAN DER MEER, N. DE JONG, D. LOHSE, M. VERSLUIS, "Changes in microbubble dynamics near a boundary revealed by combined optical micromanipulation and high-speed imaging", Appl. Phys. Lett. **90**, 114103 (2007).

[30] V. GARBIN, D. COJOC, E. FERRARI, R. Z. PROIETTI, S. CABRINI, E. DI FABRIZIO , "Optical micro-manipulation using Laguerre-Gaussian beams", Japan. J. Appl. Phys. **44**, 5773-5776 (2005).

[31] P. A. PRENTICE, M. P. MACDONALD, T. G. FRANK, A. CUSCHIERI, G. C. SPALDING, W. SIBBETT, P. A. CAMPBELL, K. DHOLAKIA, "Manipulation and filtration of low index particles with holographic Laguerre-Gaussian optical trap arrays", Opt. Express **12**, 593 (2004).

[32] C. T. CHIN, C. LANCÉE, J. BORSBOOM, F. MASTIK, M. E. FRIJLINK, N. DE JONG, M. VERSLUIS, D. LOHSE, "Brandaris 128: A digital 25 million frames per second camera with 128 highly sensitive frames", Rev. Sci. Instrum. **74**, 5026–5034 (2003).

[33] M. EMMER, A. VAN WAMEL, D. E. GOERTZ, N. DE JONG, "The onset of microbubble vibration", Ultrasound Med. Biol. **33**, 941–949 (2007).

[34] T. G. LEIGHTON, *The Acoustic Bubble*, Academic Press (1994).

[35] N. DE JONG, M. EMMER, C. T. CHIN, A. BOUAKAZ, F. MASTIK, D. LOHSE, M. VERSLUIS, "'Compression-only' behavior of phospholipid-coated contrast bubbles", Ultrasound Med. Biol. **33**, 653–656 (2007).

[36] J. E. CHOMAS, P. A. DAYTON, D. MAY, J. ALLEN, A. KLIBANOV, K. W. FERRARA, "Optical observation of contrast agent destruction", Appl. Phys. Lett. **77**, 1056–1058 (2000).

[37] S. M. VAN DER MEER, B. DOLLET, D. E. GOERTZ, N. DE JONG, M. VERSLUIS, D. LOHSE, "Surface modes of ultrasound contrast agent microbubbles", 2006 IEEE International Ultrasonics Symposium Proceedings.

[38] H. LAMB, *Hydrodynamics*, 6th Edition, Cambridge University Press (1932).

[39] C. HAYASHI, *Nonlinear Oscillations in Physical Systems*, McGraw-Hill, New York (1964).

[40] S. M. VAN DER MEER, B. DOLLET, M. M. VOORMOLEN, C. T. CHIN, A. BOUAKAZ, N. DE JONG, M. VERSLUIS, D. LOHSE, "Microbubble spectroscopy of ultrasound contrast agents", J. Acoust. Soc. Am. **121**, 648–656 (2007).

[41] K. TSIGLIFIS, N. A. PELEKASIS, "Axisymmetric stability of an encapsulated micro-bubble subject to acoustic disturbances", submitted to J. Fluid Mech.

[42] W. LAUTERBORN, "Nonlinear oscillations of gas bubbles", J. Acoust. Soc. Am., **59**, 283–293 (1976).

[43] M. STRASBERG, "The pulsation frequency of nonspherical gas bubbles in liquids", J. Acoust. Soc. Am. **25**, 536–537 (1953).

[44] J. R. BLAKE, D. C. GIBSON, "Cavitation bubbles near boundaries", Ann. Rev. Fluid Mech. **19**, 99–123 (1987).

[45] E. KLASEBOER, K. C. HUNG, C. WANG, C. W. WANG, B. C. KHOO, P. BOYCE, S. DEBONO, H. CHARLIER, "Experimental and numerical investigation of the dynamics of an underwater explosion bubble near a resilient/rigid structure", J. Fluid Mech. **537**, 387–413 (2005).

[46] C. D. OHL, M. ARORA, R. IKINK, N. DE JONG, M. VERSLUIS, M. DELIUS, D. LOHSE, "Sonoporation from jetting cavitation bubbles", Biophys. J. **91**, 4285–4295 (2006).

[47] M. S. LONGUET-HIGGINS, "Monopole emission of sound by asymmetric bubble oscillations. Part 1. Normal modes", J. Fluid Mech. **201**, 525–541 (1989).

6

Bubble resonance using chirps[§]

The eigenfrequency of a contrast bubble can be determined optically with a high speed camera by insonifying a bubble with several bursts of a fixed frequency consecutively, and analyzing its response (see Ch. 3). However, analysis of a single bubble requires much recording memory capacity. Using a chirp as driving pressure decreases the amount of the recording memory needed significantly, while delivering the same information about the eigenfrequency. The method analyzes the power spectra and the phase difference of the driving pressure and the radial response to extract the eigenfrequency (the method extracts the frequency with the largest oscillation amplitude; for very nonlinear oscillations, we term this the peak frequency). Even though the methods are based on fitting with linear models, for very nonlinear radial oscillations, the peak frequency could be determined with high accuracy. The data extracted with the chirp resonance method complements the data recorded with the microbubble spectroscopy method. A decrease in peak frequency of a bubble with increasing radial oscillation amplitude was observed with the methods. Simulations using the Rayleigh–Plesset equation confirmed that the chirp resonance methods are able to determine the peak frequency. They are also in accordance with an analytical study. Finally, the difference between the bubble response on up sweep chirps and down sweep chirps was studied.

6.1 Introduction

Diagnostic ultrasound imaging is based on transmitting and receiving ultrasound waves. The waves are generated by a transducer consisting

[§]Based on: Sander van der Meer, Nico de Jong, Michel Versluis, "Bubble resonance using chirps", in preparation; Section 6.5 is based on: Ayache Bouakaz, Sander van der Meer, Michel Versluis, Anthony Novell, Nico de Jong, "Chirp reversal for contrast imaging: high speed optical verification", in preparation.

of piezo-electric crystals which convert electric signals into ultrasonic pulses [1]. The transmitted waves propagate through a medium until they hit reflecting or scattering objects, and the reflected waves are received by the same transducer.

The scattering of blood is low compared to the scattering of surrounding tissue. The scattering can be enhanced by introducing an ultrasound contrast agent into the blood. An ultrasound contrast agent is a liquid containing many microbubbles, which very effectively scatter the ultrasound [2–4]. In this way, it is possible to visualize and quantify the perfusion of tissue, like for instance the heart muscle, liver or kidney. Contrast agents are nowadays used in various medical investigations, e.g. in obtaining diagnostic information from the volume and shape of the heart ventricles, or to quantify the perfusion of various organs, like liver or kidney.

The development of ultrasound contrast agents lagged behind that of some of the other imaging modalities, even though ultrasound is used worldwide and is a technology that would benefit from an increased signal-to-noise ratio. Part of the lag in contrast agent development was due to the pharmaceutical challenge of creating a safe material that effectively scattered ultrasound. The challenge was further increased by the difficulty of reproducibly predicting and characterizing the properties of these materials with results that correlated with clinical data. Characterizing the properties of individual contrast bubbles is therefore of importance, and an important property of the microbubbles is their resonance frequency.

Previously, the analysis of the resonance frequency of contrast bubbles was based on the analysis of the radial response of the microbubbles on different bursts of a fixed frequency. With approximately 10 different interrogation waves of 8 cycles, the resonance frequency of the microbubbles was studied [5]. The technique was termed microbubble spectroscopy.

Since this method is very recording memory intensive, a new method was developed. Here, we replace the 10 interrogation waves of fixed frequency into one wave with a chirp, which is a frequency sweep. Chirps are also used in pulse sequences for imaging [6, 7]. The bubble response on a chirp is compared with the bubble response on microbubble spectroscopy. The method is faster in deriving the resonance frequency from a contrast agent microbubble, and less recording memory is needed. With chirps, the effect of the amplitude of the driving pressure is examined.

First, simulations are presented to illustrate the strength and the

stability of the chirp resonance method. Experiments with both the microbubble spectroscopy method and with the chirp resonance method are presented, and a dependence of the peak frequency on the amplitude of the driving pressure was found.

6.2 Resonance using chirps: Simulations

To gain insight in the oscillating behavior of bubbles as a response on chirp signals, simulations were performed. We use the following description of a linear chirp for the forcing term.

6.2.1 Theoretical description of a chirp

A chirp is a signal in which the frequency increases (up sweep chirp) or decreases (down sweep chirp) in time. In a linear chirp, the instantaneous frequency $f(t)$ varies linearly with time:

$$f(t) = f_{center} + kt. \tag{6.1}$$

Here, f_{center} is the center frequency of the chirp (at $t = 0$) and k is the rate of frequency increase (or chirp rate). The value of k is positive for up sweep chirps and negative for down sweep chirps.

The chirp itself is given by the following equation:

$$x(t) = \cos(2\pi \int_0^t f(\tilde{t})\mathrm{d}\tilde{t}) = \cos(2\pi(f_{center} + \frac{k}{2}t)t). \tag{6.2}$$

The chirp was modulated with a cosine tapering window or Tukey window, to minimize side lobes in the frequency spectrum. In this window, a fraction $(\alpha/2)$ of the total pulse duration (T) is tapered at each end with a cosine lobe of width $(1-\alpha)T/2$. This window attempts to bring the data to zero smoothly at both ends without significantly affecting the bulk of the data points. The window function in the time domain $w(t)$ is defined as:

$$w(t) = \begin{cases} 1 & \text{for } 0 \leq |t| \leq \alpha\frac{T}{2} \\ \frac{1}{2}\left[1 + \cos\left(\pi\frac{|t|-\alpha T/2}{(1-\alpha)T/2}\right)\right] & \text{for } \alpha\frac{T}{2} \leq |t| \leq \frac{T}{2} \end{cases} \tag{6.3}$$

The window evolves from a rectangle to a Hanning window as α varies from 0 to 1. We use an α of 0.5.

The bandwidth of the used chirps was 90%, allowing us to scan a large range of frequencies in a single wave.

6.2.2 Simulations with a harmonic oscillator

If a bubble is insonified with a small acoustic pressure, it is well known [8, 9] that a bubble behaves as a linear oscillator; its relative radial excursion x, defined as $R = R_0(1+x)$, obeys the equation:

$$\ddot{x} + \omega_0 \delta \dot{x} + \omega_0^2 x = F(t), \tag{6.4}$$

with $f_0 = \omega_0/2\pi$ the eigenfrequency of the system and δ its (linear) dimensionless damping coefficient (equivalently, one can define the quality factor $Q = 1/\delta$), and F is the driving force term.

The radial dynamics of the bubble depend on the driving frequency $f = \omega/2\pi$. Writing $F(t) = F_0 \sin \omega t$ and $x(t) = x_0 \sin(\omega t + \varphi)$, one gets from Eq. (6.4):

$$x_0(\omega) = \frac{F_0}{\sqrt{(\omega_0^2 - \omega^2)^2 + (\delta\omega\omega_0)^2}}. \tag{6.5}$$

This equation defines the resonance curve, displaying a maximum at the resonance frequency:

$$f_{\text{res}} = f_0 \sqrt{1 - \frac{\delta^2}{2}}, \tag{6.6}$$

which is lower than the eigenfrequency f_0 in the presence of damping. Strictly speaking, Eq. (6.6) holds only if the damping coefficient δ is independent of ω.

The response of a harmonic oscillator on a driving amplitude was numerically solved. The goal of the simulation was to verify the possibility to derive the properties of the harmonic oscillator such as the eigenfrequency from the response; by successfully doing so the chirp resonance method is proven a valid method.

The values for the eigenfrequency f_0 and the damping δ of the harmonic oscillator were fixed. Then, the response on a driving chirp signal was numerically solved using the ode45 solver in Matlab (The Mathworks).

6.2.3 Deriving the eigenfrequency

In Fig. 6.1 the result of a simulation is shown. There are two methods to derive the eigenfrequency and the damping from the numerical data. The first method focusses on the power spectra of the oscillations. We calculate power spectra both from the driving ($P(f)$, see Fig. 6.1B) and from the

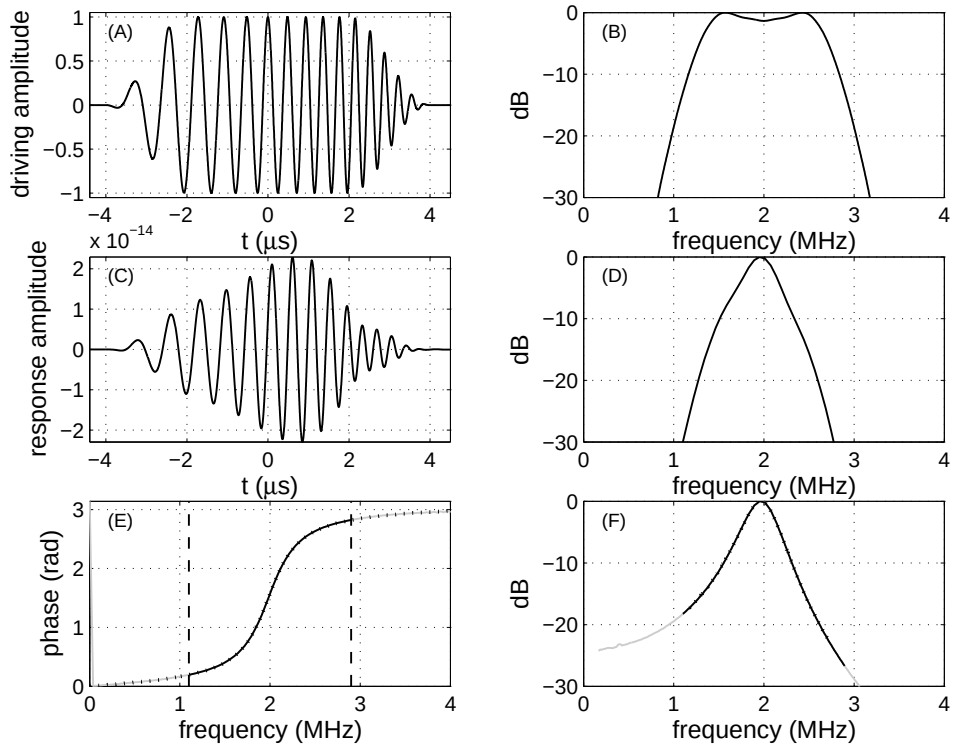

Figure 6.1: Demonstration of the chirp resonance methods, with the harmonic oscillator. The eigenfrequency was set to 2 MHz, and the damping was set to 0.25. In (A) the driving amplitude is shown. In (C) is the response amplitude of the harmonic oscillator is shown. The corresponding powerspectra $P(f)$ and $R(f)$ are displayed in (B) and (D). The phase difference between the driving amplitude and the response amplitude (solid line) and the best fit to it (dotted line) are shown in (E). The powerspectrum that shows the pure response of the harmonic oscillator $R_{result}(f)$ (solid line) and the best fit (dotted line) are shown in (F); this is obtained by normalizing (D) with (B). The fitting parameters of the power spectrum method: f_0=2.00 MHz, δ=0.25, and for the phase fitting: f_0=2.00 MHz, δ=0.25.

oscillator response ($R(f)$, see Fig. 6.1D). The response power spectrum is then normalized by the input frequencies ($R_{result}(f) = R(f)/P(f)$, see Fig. 6.1F). The resulting power spectrum then contains only the response of the harmonic oscillator system. The eigenfrequency and damping can be determined, by fitting the resulting power spectrum to the equation of a harmonic oscillator.

A second method of deriving the eigenfrequency and the damping, is by examining the phase difference between driving amplitude and response amplitude. According to theory, the phase lag φ is:

$$\tan\varphi = \frac{\delta_{\text{tot}}}{\frac{f_0}{f} - \frac{f}{f_0}}. \tag{6.7}$$

By calculating the phase difference between the driving amplitude and the response oscillation, and then fitting to Eq. (6.7), we can also derive the eigenfrequency and the damping. An example of this is shown in Fig. 6.1E.

The stability of the methods

The ode45 solver was used with a variable (time) step size. On average, around 20k simulation points were used for the harmonic response.

Both up sweep driving chirp signals and down sweep driving chirp signals were tested. The bandwidth of the chirp was chosen to be 90%, thus we investigate the oscillator response on a large range of frequencies.

Sensitivity to numerical noise The eigenfrequency of the harmonic oscillator, as well as the center frequency of the driving chirp were varied from 0.8 MHz to 5 MHz. The damping was varied from 0.1 to 1. The chirp duration was 8 μs, and the simulation duration was from 0.5 μs before, till 6 μs after the chirp. In all cases, using the power spectrum fitting, the eigenfrequency and the damping was retrieved from the fitting parameters.

For low damping, the error in eigenfrequency with the power spectrum method is smaller than with the phase difference method. For high damping, the phase difference method is more accurate. In all cases, the error in the found eigenfrequency was less than 1%.

The error in the damping with the power spectrum method was found to be 25%. The phase difference method gives slightly more accurate fitting values.

Sampling There were approximately 5k simulation points used for the harmonic response. Using the fast Fourier transform (FFT) function of Matlab, the frequency spectrum contains approximately 8k sample points. The frequency range of interest, which extends around the center frequency of the chirp in a 90% bandwidth, contains only 25 datapoints in

experiments. This is enough to get an accuracy of the fitting parameters within 2%.

We resample the response amplitude down to 100 sample points, to verify if the methods are still able to determine the eigenfrequency and the damping. Still, the accuracy of the eigenfrequency fit remains high, the error is smaller than 5%. This happens for high damping values, because the peak spans over a large part of the frequency content of the chirp sweep, and at high frequencies, because the high frequency content of the chirp sweep reaches the Nyquist-frequency.

In a few cases, there was no fit found. This only happened with the power spectrum method, when using an up sweep chirp. In the other cases, there was no difference observed between the power spectrum method and the phase difference method.

For damping, the error in the fitting parameter is after downsampling still approximately 25%. Again, the error is largest for high damping, and high frequencies.

Noise We introduce noise to the simulation data to test the stability of the methods. White noise with an amplitude of ± 10 % of the maximum response amplitude was added to the downsampled response amplitude.

The error in the eigenfrequency is, as expected, larger with noise. In 98% of the cases a fit with an error of 10% can be made. Both methods give similar results.

The error in the damping is also larger. In 90% of the cases, a fit with an error of 25% can be achieved.

Conclusion The method of deriving the eigenfrequency and the damping of a harmonic oscillator was simulated. Without noise added to the simulations, the methods are very stable in deriving the eigenfrequency. Even when the response amplitude curve is downsampled to 100 datapoints, the error is still only 5%.

The method also succeeds when noise is introduced. Adding noise to the simulation datapoints will increase the error in the eigenfrequency. However, even when noise with an amplitude of ± 10% of the maximum response amplitude is added, the eigenfrequency error will still be around 10%. In approximately 2% of the cases, a fit cannot be found.

The fit for the damping gives a much larger error. Especially oscillations with high damping give a broad peak in the power spectrum. Both the power spectrum method and the phase difference method fail to give

a good estimate of the damping. With noise, in 90% of the cases a fit with an error of 25% can be achieved. Because of this, in this article we focus mainly on deriving the eigenfrequency.

Our general experimental data falls within the limits described above. The methods are suitable to determine eigenfrequency from experimental data.

6.2.4 Simulations using a free bubble model

An oscillating bubble can behave as a harmonic oscillator. Properties like bubble radius, liquid density and surface tension, ambient pressure and shell elasticity cause the bubble to have a resonance frequency. Heating of the bubble, viscosity, sound radiation and the bubble shell account for damping of the system. For small amplitude oscillations, the bubbles behavior can be described by the equations of a harmonic oscillator. However, if we increase the oscillation amplitude, the bubble oscillations start to become nonlinear. This changes the frequency content in the power spectrum of the oscillation response. This section investigates the usability of the methods described in Sec. 6.2.2.

In order to determine if the methods to derive parameters like eigenfrequency or damping are also functioning for free bubbles, we perform simulations with a proven bubble model, the Rayleigh Plesset equation for free floating bubbles. A detailed explanation of the equation is given in [8, 10]. Linearization of the RP equation gives the Minnaert frequency f_M [11],

$$f_M = \frac{1}{2\pi}\sqrt{\frac{1}{\rho R_0^2}\left[3\gamma P_0 + \frac{2(3\gamma-1)\sigma}{R_0}\right]}. \tag{6.8}$$

This equation can be used to compare our simulations and experiments to. In Eq. (6.8), ρ is the density of the liquid, R_0 is the resting radius of the bubble, γ is the polytropic exponent, P_0 is the ambient pressure, and σ is the surface tension of the liquid.

In Fig. 6.2 we show a typical simulation example. A bubble with a resting radius $R_0 = 2$ μm is insonified with a driving chirp of 1 kPa (shown in Fig. 6.2A). The response was numerically solved, using the ode45-solver in Matlab (The Mathworks). It is displayed in Fig. 6.2C. The powerspectra of both signals are shown in Figs. 6.2B and D. Normalizing the response powerspectrum with the driving frequencies, leads to the powerspectrum in Fig. 6.2F. This normalized spectrum is then fitted to Eq. (6.5). The best fit to the simulation data, give an eigenfrequency f_0 = 2.02 MHz, and a

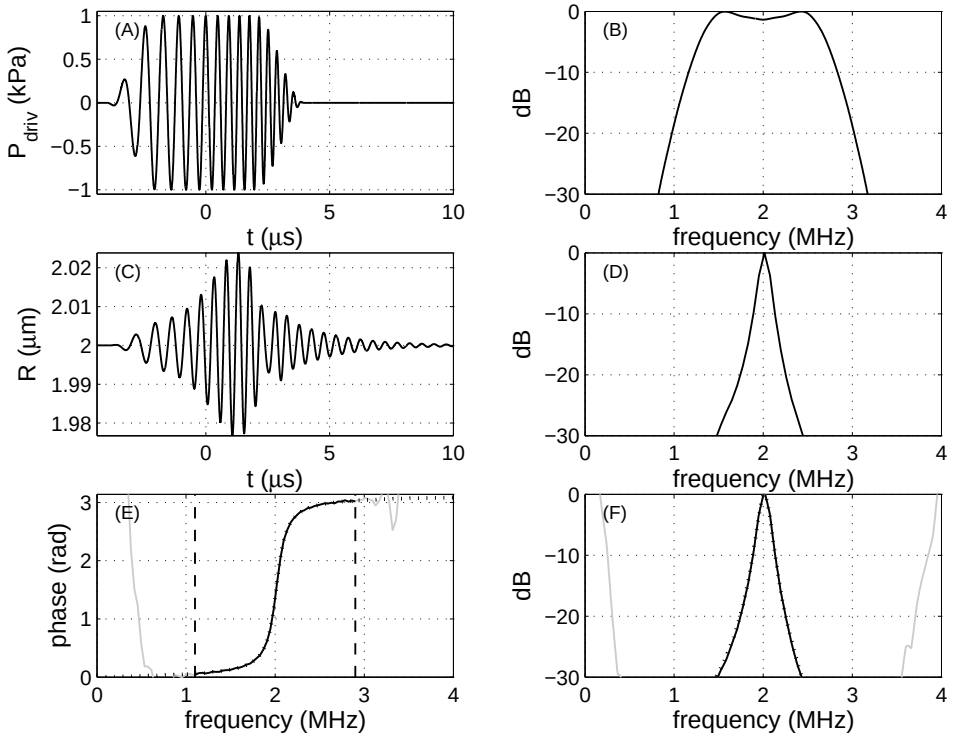

Figure 6.2: Simulation results using the RP equation. In (A) the driving pressure amplitude of a 1 kPa, 2 MHz chirp of 8 μs is shown. In (C) the radial response amplitude of a the bubble is shown. The corresponding powerspectra are displayed in (B) and (D). The phase difference between the driving amplitude and the response amplitude (solid line) and the best fit to it (dotted line) are shown in (E). The powerspectrum that shows the pure bubble response (solid line), and the best (dotted line) are shown in (F); this is obtained by normalizing (D) with (B). The fitting parameters of the power spectrum method: f_0=2.02 MHz, δ=0.084, and for the phase fitting: f_0=2.02 MHz, δ=0.079.

damping δ = 0.084. The eigenfrequency of a 2 μm bubble, according to Eq. (6.8), is 2.02 MHz indeed.

6.2.5 Comparison with microbubble spectroscopy

Harmonic oscillator We determined the fitting parameters f_0 and δ using both the chirp resonance method and the microbubble spectroscopy method. [5]. For a harmonic oscillator, and in the parameter space of

0.8 MHz < f_0 < 5 MHz and 0.01 < δ < 10 we found a perfect agreement between the fitting parameters, provided the duration of the chirp was longer than 2 μs. For shorter chirps, the bubble does not have time to follow the imposed oscillations, and the method will no longer work.

Free bubble model Both the chirp resonance method and the microbubble spectroscopy method are linear methods, i.e. the calculation of the fitting parameters f_0 and δ is based on fitting with Eq. (6.5), which is the amplitude of a harmonic oscillator, a linear system. Therefore, for simulations with the RP equation, we distinguish two cases.

For small driving amplitudes, or short chirps, the bubble oscillations are small, and can be considered linear. Both microbubble spectroscopy and the chirp resonance method give similar results for the fitting parameters.

If the bubble oscillations become large and nonlinear, either by a high driving amplitude or a long chirp length of medium amplitude, the value of the found eigenfrequency starts to deviate. The chirp resonance values (both by the power spectrum method and the phase method) are also deviating, and they are lower than the microbubble spectroscopy value. A more detailed analysis is given in Sec. 6.4.

6.3 Experiments using chirps

In the following Section, we describe the experiments that we have performed with contrast agent microbubbles. We insonified contrast agent microbubbles with a chirp driving pressure, and recorded the response of the bubble. In the following Sections, the experimental setup is described, followed by a Section about the experiments. Then, the data analysis is explained, and the results are presented. Finally, a comparison with the microbubble spectroscopy experiments is presented.

6.3.1 Experimental setup

The experimental setup is schematically drawn in Fig 6.3. A dilute solution of individual SonoVue® contrast bubbles (Bracco Research S.A., Geneva, Switzerland) is prepared and injected through a capillary fiber of diameter 200 μm immersed in water. The bubbles are illuminated from below with an optical fiber and an image is produced by a microscope (Olympus BXFM) with a 100$\times$ water-immersed objective and a 2$\times$

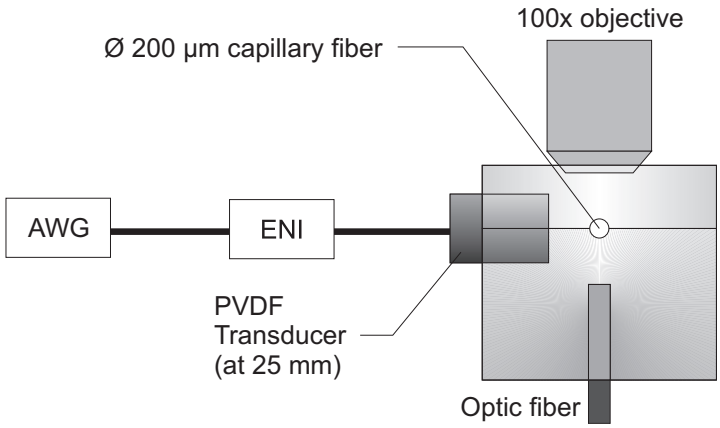

Figure 6.3: The experimental setup: an arbitrary waveform generator produces ultrasound signals that are amplified by an amplifier and led to a transducer. Contrast bubbles are injected through a 200 μm capillary fiber perpendicular to the plane of the figure. The contrast bubbles are imaged from the top through a 100$\times$ objective and illumination is provided from below.

magnifier. We carefully check that only single bubbles are present in the field of view of the microscope. The image is relayed onto a CCD camera (Watec, CCIR LCL 902K) for size estimation, and simultaneously onto the Brandaris high-speed camera [12]. The camera can record six movies of 128 frames at up to 25 million frames per second. Illumination to the microbubbles was provided with an optic fiber, connected to a Xenon flash light source (Perkin Elmer, MVS 7010). The contrast bubbles were insonified by a broadband single element transducer (Precision Acoustics, PA081) with a center frequency of 1.7 MHz and a calibrated range of frequencies from 0.7 to 6 MHz. An arbitrary waveform generator (AWG), a Tabor 8026, connected to a PC, was used to produce the required waveforms, which were then amplified by an ENI 350L amplifier.

6.3.2 Experimental method

The experiments described here were always performed within 6 hours after the preparation of the contrast bubbles. This assures that all bubbles are in a similar state, since, as described in Sec. 2.3.2, contrast bubbles can change over time. The setup was programmed to record the response of the individual contrast bubbles on up sweep and down sweep chirps.

The procedure was as follows. First we isolated a single contrast agent microbubble in the focus of the microscope. Then, using the image on the Watec CCD camera, we estimated its size. Using previous resonance experiments [5], we estimated the resonance frequency of the microbubble. This estimated resonance frequency was then taken to be the center frequency of the interrogation chirp, making sure the frequencies of the chirp remained in the calibrated regime. A bandwidth of 80% was used. Since the camera records the bubble oscillations at 15 Mfps, and the camera records 128 frames, a typical movie has a duration of 8.5 μs. We program the chirp to be roughly 8 μs in duration, so the whole time of chirp driving is recorded in the movie. The first and last μs of the chirp is tapered using a Tukey window. The amplitude of the driving pressure was determined by a tradeoff of oscillation response linearity (low pressure amplitude needed) and signal-to-noise ratio (high pressure amplitude needed). In general, an oscillation amplitude of 60 kPa was chosen. Lower and higher pressures have also been used here, to determine the effect of pressure on the resonance frequency.

The dynamics of the contrast bubbles were recorded at 15 Mfps. From the images, we extract the radius-time information. The radius-time curves of individual bubbles were measured using a so-called dynamic programming algorithm [13].

In Fig. 6.4A the applied pressure P_{driv} as a function of time t is displayed. Below, in Fig. 6.4B the radius-time curve of a typical bubble is shown. Also, the power spectra of both curves are shown, the driving chirp power spectrum is shown in Fig. 6.4C, and the power spectrum of the radial oscillation if shown in Fig. 6.4D.

6.3.3 Data analysis

If the power spectrum of the driving chirp (see Fig. 6.4A) was completely flat, i.e. if all the frequencies with which we insonify the bubble were equally represented, we could use this power spectrum to fit to the resonance of a harmonic oscillator, to derive the eigenfrequency and damping. In practice, due to the tapering of the chirp (see Eq. (6.3)), this power spectrum is not entirely flat. By normalizing the calculated spectrum by the driving frequencies, we make sure the power spectrum is purely describing the presence of the frequencies in the bubble oscillation. This is shown in Fig. 6.4F.

The normalized power spectrum can be used to fit to the resonance of a harmonic oscillator, to derive the eigenfrequency and damping of the

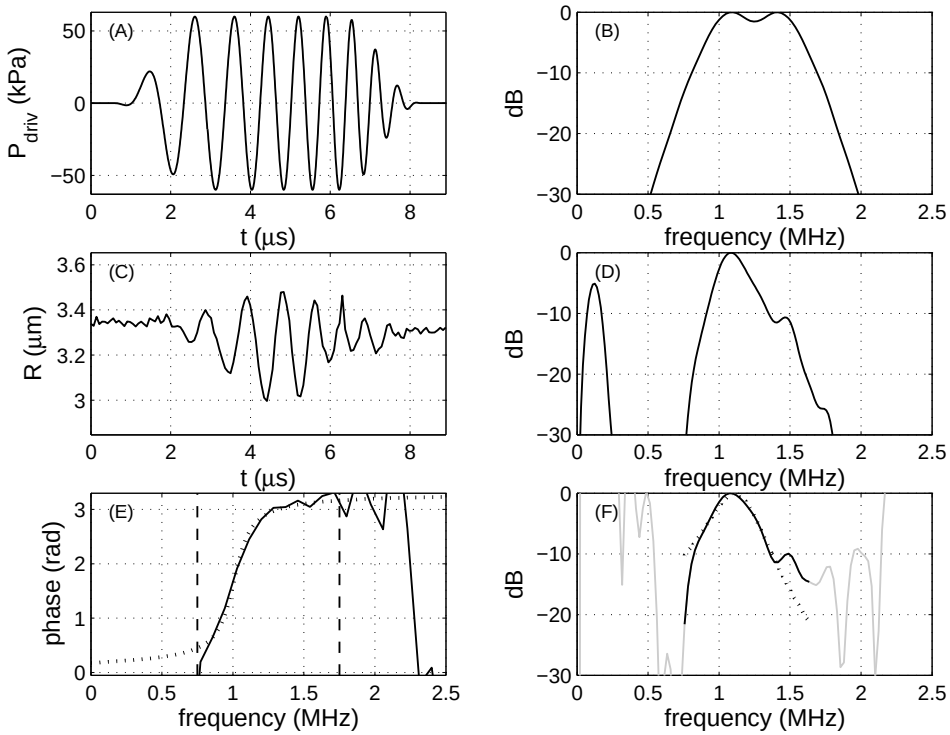

Figure 6.4: Experimental data showing the chirp resonance method. Compare this graph with Fig. 6.1. (A) shows the applied pressure, (C) shows the radius-time curve of a typical bubble. (B) and (D) display the corresponding powerspectra of the oscillations. (E) shows the phase difference between the driving pressure and the R(t) curve (solid line) and the best fit (dotted line), and (F) shows the normalized powerspectrum (solid line), also with best fit (dotted line). The fitting parameters of the power spectrum method: f_0=1.14 MHz, δ=0.34, and for the phase fitting: f_0=1.01 MHz, δ=0.17.

bubble oscillation. In Fig. 6.4F, the powerspectrum curve shows a black and a grey part. The grey part is unimportant, since this extends beyond the frequency content of the chirps. There, the difference between experimental response powerspectrum and theoretical insonation powerspectrum becomes large, because the experimental response powerspectrum contains noise, whereas the theoretical insonation powerspectrum is still quite smooth. Thus, only the black part of the curve is used for the fitting. The dotted curve in Fig. 6.4F is the best fit to the harmonic oscillator resonance.

Using the second method, by analyzing the phase difference between the driving chirp and the radial response, the resonance frequency can also be determined. In Fig. 6.4E, the experimental data (solid line) is fitted by Eq. (6.7) (dotted line). For the phase delay method, it is very important to know the exact time delay between the driving and the response signal. However, in experiments the exact time delay between driving pressure and response curve is accurate enough.

The used signals can be represented by $g(t) = P_a e^{i\omega t}$. If however we add a delay in time, $g(t) = P_a e^{i\omega(t+\Delta t)}$, which we also write as $P_a e^{i(\omega t+\varphi)}$, we add a phase shift $\varphi_t = \omega\Delta t = 2\pi f\Delta t$. The phase delay between the signals thus increases linearly with the chirp frequency. This complicates the fit to the phase delay. An extra fitting parameter Δt is introduced, and the total phase difference becomes:

$$\varphi = 2\pi f\Delta t + \arctan\left(\frac{\delta_{\text{tot}}}{\frac{f_0}{f} - \frac{f}{f_0}}\right). \tag{6.9}$$

However, with good initial estimates for the fit parameters, experimental data can also be analyzed with this method.

6.3.4 Results

In total 152 bubbles were analyzed with the power spectrum method. Most bubbles (122) were insonified with a pressure of 60 kPa. However, a total of 20 bubbles were insonified with a pressure lower than 60 kPa. 10 bubbles were insonified with a higher pressure.

The phase difference method is more susceptible to noise, therefore only 98 bubbles were analyzed with this method. 76 bubbles at a pressure of 60 kPa, 12 bubbles with a pressure lower than 60 kPa, and 10 bubbles with a higher pressure.

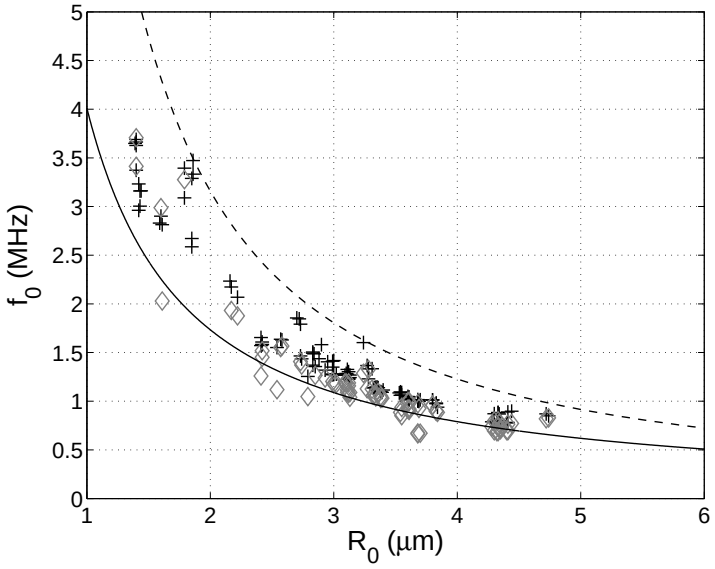

Figure 6.5: Experimentally determined eigenfrequency as function of bubble radius, all at a driving pressure of 60 kPa. The plus symbols (+) are determined with the power spectrum method, while the diamond shaped symbols (◇) are determined with the phase difference method. The solid line shows the Minnaert frequency (Eq. (6.8)). The dashed line shows the best fit through the microbubble spectroscopy data points of Ch. 3, see Fig. 3.6.

Here, the focus is on the bubbles that we measured with a driving pressure of 60 kPa. In Fig. 6.5 the experimentally determined eigenfrequency is reported as a function of bubble radius. As expected, the eigenfrequency decreases with increasing bubble radius. In the figure, both the datapoints recorded with the power spectrum method and the phase difference method are shown. It can be seen that on average, the datapoints recorded with the power spectrum method are slightly higher than the datapoints recorded with the phase difference method. In Sec. 6.4 an explanation is given for the difference.

6.3.5 Comparison with microbubble spectroscopy

We compare Fig. 6.5 to the data recorded with the microbubble spectroscopy data (see [5] or Fig. 3.6). The solid line in both graphs represents the Minnaert equation for free gas bubbles (Eq. (6.8)) with similar param-

eters.

For comparison, the best fit through the microbubble spectroscopy datapoints of Ch. 3, is also shown in Fig. 6.5 (see Fig. 3.6). We can see that the data recorded with both chirp resonance methods, lies below the data recorded with the microbubble spectroscopy. How is this possible?

There are a number of obvious differences between the experiments.

- The microbubble spectroscopy is done on BR-14 bubbles, while the chirp resonance experiments were done on SonoVue® bubbles. Both bubbles are manufactured by Bracco Research S.A., Geneva, Switzerland. The most important difference between the bubbles is the gas. BR-14 bubbles contain C_4F_{10} gas [14], while SonoVue® bubbles contain SF_6 gas. While C_4F_{10} gas is heavier than SF_6 gas, the mass is negligible compared to the mass of water, and therefore there should be no difference in the oscillating behavior of the bubble.

- The method itself is different. However, with the simulations (see Sec. 6.2) we proved both the values found by the microbubble spectroscopy method, and the chirp resonance methods should not differ from each other.

- The most probable reason is the fact the datapoints in the microbubble spectroscopy method were all recorded at driving pressures of 40 kPa and less. Due to a low signal-to-noise ratio at 40 kPa with the chirp resonance measurements, it was necessary to record the data at a higher pressure of 60 kPa. The following Section will go into more detail on pressure and oscillation amplitude effects.

6.4 Oscillation amplitude dependence

It is important to understand the frequency-amplitude relation of oscillating bubbles. It is known from nonlinear oscillating systems, that the resonance peak in an amplitude versus frequency plot bends over towards a lower or a higher frequency (depending on it being a system with a softening or hardening spring) for increasing oscillation amplitude. In the Appendix, Sec. 6.7, we perform an analytical analysis to determine the peak shift for an oscillating bubble system. As we can see from Figs. 6.18 and 6.19 in the Appendix, for an oscillating bubble the peak of the resonance frequency shifts towards lower frequencies for increasing pressure amplitude.

In order to get the maximum bubble response, it is important to know this peak frequency. Strictly speaking, as discussed in Ch. 3 and seen from Eq. (6.6), the frequency we derive is the eigenfrequency f_0 while the peak is found at the resonance frequency f_{res}. However, as discussed in Ch. 3, on average the total damping δ_{tot} of the contrast microbubbles was measured to be 0.26. Equation (6.6) predicts the resonance frequency to be only 3% lower than the eigenfrequency. Since the resonance frequency and the eigenfrequency are both linear concepts, in the following section we will use the term 'peak frequency'. In this section we will discuss our simulations and experiments to measure this peak frequency.

The shift of the peak is a nonlinear effect. Both the microbubble spectroscopy method and the chirp resonance methods however are based on fitting with linear equations. Also, normalizing the (radial) response power spectrum with the driving (pressure) power spectrum is only allowed when the system is linear. We therefore expect a deviation from the exact peak frequency value with the methods. In the following section we investigate the accuracy of both the microbubble spectroscopy method as well as the chirp resonance methods for nonlinear oscillations.

6.4.1 Simulations

We performed simulations using microbubble spectroscopy and both chirp resonance methods to determine the accuracy of both methods.

For our understanding, we discard shell effects and focus on pure bubble behavior. We therefore use the Rayleigh Plesset model for free floating bubbles, as described in Sec. 6.2.4. In the following sections the specific simulation methods are described.

Microbubble spectroscopy

From the Minnaert equation, one can calculate the eigenfrequency of a free bubble of $R = 3$ μm will be at $f_0 = 1.26$ MHz. We numerically calculated the radius-time curves of a bubble responding on 30-cycle bursts of a fixed frequency, from 0.5 to 1.5 MHz. This simulation was performed from 5 kPa to 35 kPa with intervals of 5 kPa, and also a simulation was performed at 1 Pa. From the $R(t)$-curves, a power spectrum is constructed and this is fitted to the equation of a harmonic oscillator, which gives in the best fit a value for the peak frequency.

In experiments, due to a limited recording window, an 8-cycle burst is normally used. An 8-cycle window is expected to give a slightly

higher estimate for the peak frequency, since the oscillation amplitude will not grow as much as with the 30-cycle window. Further, in the 8-cycle window, the bubble might still contain transient oscillations, which 'pollute' the power spectrum, which may lead to a less accurate value for the peak frequency. Here, a 30-cycle burst is examined, because there the bubble will have the best chance to reach an equilibrium oscillation, free of transient dynamics. This will give the most accurate value for the peak frequency.

Chirp resonance

Again, a 3 μm free bubble was considered. The driving pulses had a duration of 8 μs, a center frequency of 1.26 MHz and a bandwidth of 90%. The amplitude of the driving pressure was varied from 1 to 35 kPa in steps of 1 kPa. A normalized power spectrum was constructed, and the phase difference was calculated, as explained in Sec. 6.2. Both from the power spectrum and from the phase difference, in the best fit a value for the peak frequency was found.

Simulation results

In Fig. 6.6 the constructed powerspectra are shown.

Note that they are in a linear-linear plot, and the physical quantity on the y-axis is different for the microbubble spectroscopy plot and the chirp resonance plot. This is inherent to the methods. Since we only fit the shape, and since the peak frequency corresponds to the position of the peak on the x-axis, we are allowed to compare the methods.

The shape of the resonance curves changes with increasing oscillation amplitude. With the microbubble spectroscopy method, the curves become 'skewed' with increasing oscillation amplitude, as expected analytically [15, 16]. The shape of the peaks in the power spectrum of the chirp resonance method are different from the peaks in the power spectrum with the microbubble spectroscopy method. Their shapes remain similar, while their positions shift to lower frequencies.

From the calculations in the Appendix, it follows that the peak frequency decreases with the increasing radial oscillation amplitude. We therefore extract the peak frequencies from the powerspectra in Fig. 6.6, and plot them versus the normalized oscillation amplitude $A_{norm} = (R_+ - R_-)/R_0$ (R_+ is the maximum radial amplitude and R_- is the minimum radial amplitude during the simulation) in Fig. 6.7. From

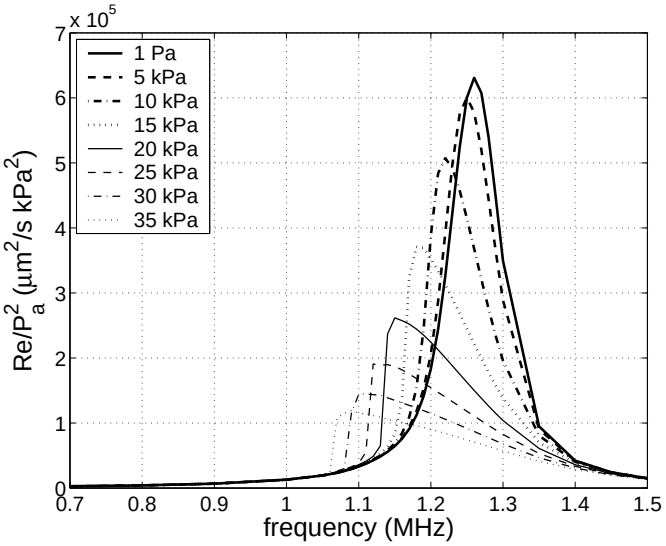

(A) Microbubble spectroscopy

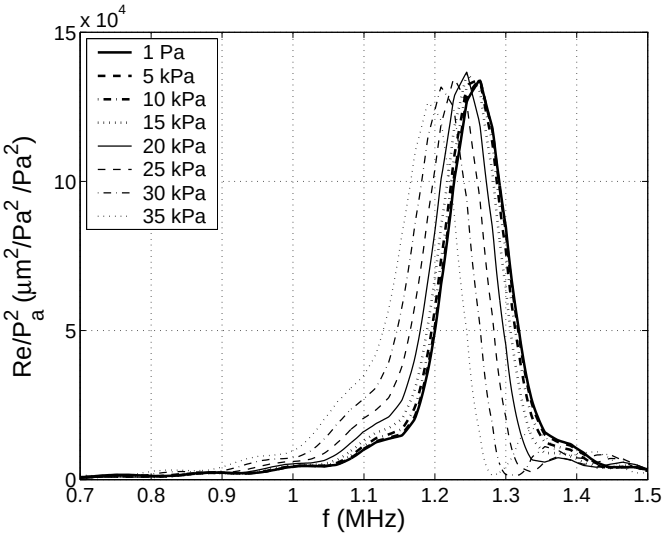

(B) Chirp resonance

Figure 6.6: Constructed power spectra by microbubble spectroscopy and chirp resonance for different driving pressure amplitudes.

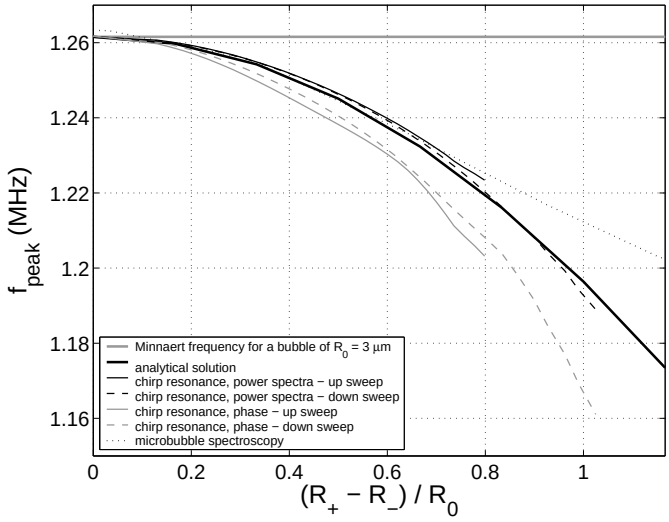

(A) Dependance of f_{peak} on oscillation amplitude

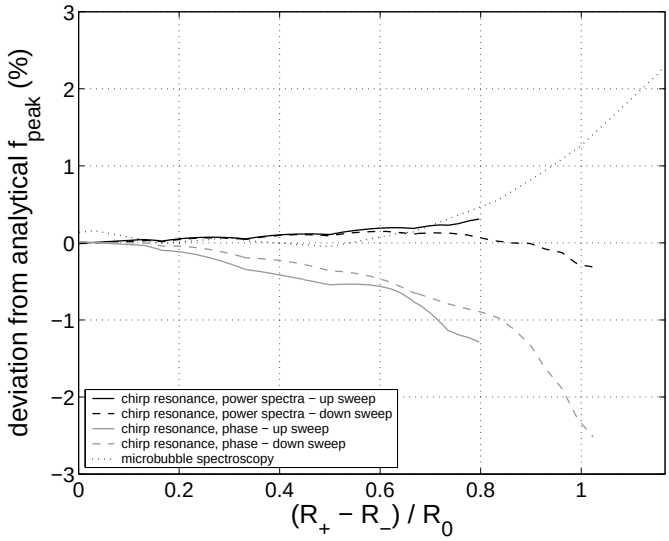

(B) Method accuracy

Figure 6.7: (A) The peak frequency as function of the normalized radial amplitude A_{norm}, extracted from the simulations with different methods. Note that in all cases, the curves collapse onto the Minnaert frequency at P_a=0 kPa. (B) The deviation from the analytically found peak frequency as numerically solved with the different methods.

this graph, we conclude that all methods predict a peak shift to lower frequencies with increasing oscillation amplitude. Only the phase difference method underestimates the peak frequency slightly (about 1% at an oscillation amplitude of 1). Furthermore, the peak frequency determination with the microbubble spectroscopy method is deviating from the 'real' peak frequency when the oscillation amplitudes become larger than approximately 0.7. In all cases, the curves collapse onto the Minnaert equation at $A_{norm} = 0$.

In Fig. 6.7B the deviation from the analytically found peak frequency is displayed. The deviation D of the numerically found values for the peak frequency from the analytical peak frequency was given by $D = (f_{peak,analytical} - f_{peak,numerical}) \,/\, f_{peak,analytical}$.

The power spectra method and the microbubble spectroscopy method are able to determine the peak frequency of a bubble with high precision (<1.5% error), even when a bubble is oscillating with very high amplitude of $A_{norm} = 1$. Analyzing the phase difference also leads to a good estimate, however in all cases the 'real' peak frequency is slightly underestimated (up to 2.5% at $A_{norm} = 1$). There is also a difference observed between up sweep chirp and down sweep chirps. This is discussed in Sec. 6.5.

6.4.2 Experiments

With the setup described in Sec. 6.3.1, both the microbubble spectroscopy experiments, as well as the chirp resonance experiments were performed. As described in [5] or in Ch. 3 the microbubble spectroscopy experiments were prepared and performed. The chirp resonance experiments were done as described in Sec. 6.3.

The driving pressures were varied between 30 and 150 kPa. Both in the microbubble spectroscopy experiments and in the chirp resonance experiments, the bubbles oscillated with a mean oscillation amplitude $A_{norm} = 0.16$ (For comparison, in the microbubble spectroscopy experiments in [5] or in Ch. 3 the mean oscillation amplitude was 0.07). Only 5 bubbles in chirp resonance and 1 bubble in microbubble spectroscopy were seen to oscillate with an amplitude larger than 0.5.

All the data is grouped into 3 categories:

I. $A_{norm} \leq 0.1$

II. $0.1 < A_{norm} \leq 0.2$

III. $A_{norm} > 0.2$

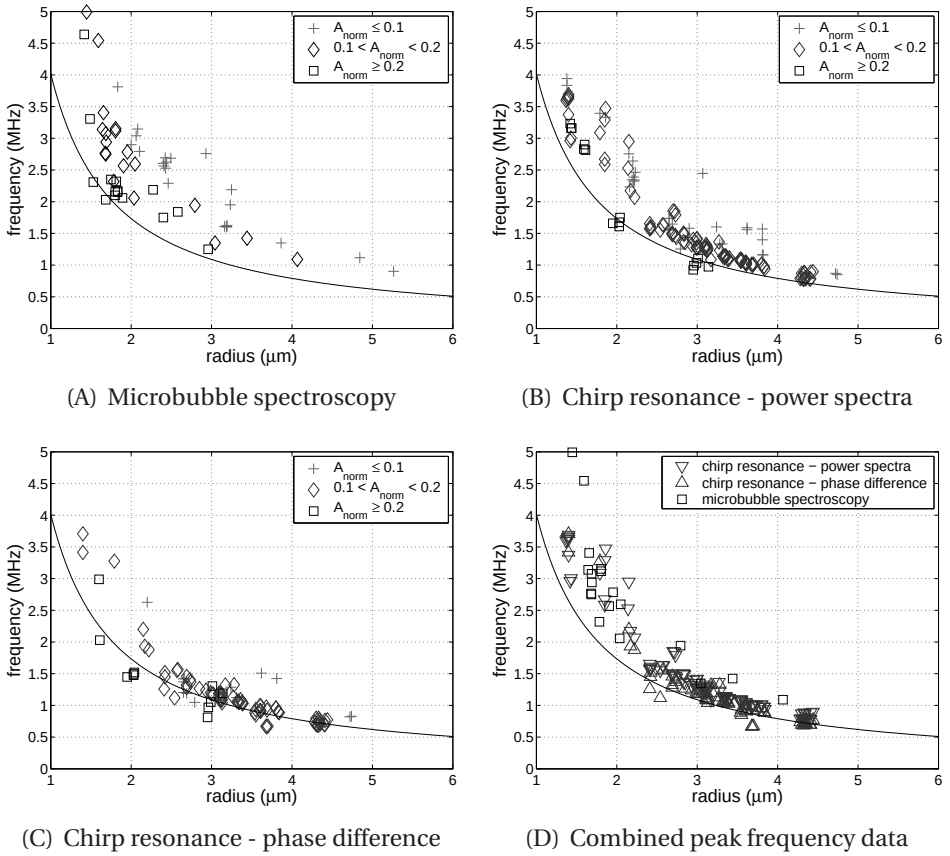

(A) Microbubble spectroscopy

(B) Chirp resonance - power spectra

(C) Chirp resonance - phase difference

(D) Combined peak frequency data

Figure 6.8: Experimentally determined peak frequency as function of bubble radius, for the microbubble spectroscopy method and both chirp resonance methods. In all graphs, the solid line represents the Minnaert frequency (Eq. (6.8)). In A, B and C the peak frequency decrease as function of oscillation amplitude is clearly visible. D combines the data of A, B and C with $0.1 < A_{norm} \leq 0.2$ (all $\diamond$ symbols); all this data collapses onto one curve.

The experiments were analyzed according to the analysis which is described in [5] or in Ch. 3 for the microbubble spectroscopy experiments, and in Sec. 6.3 for the chirp resonance experiments. In Fig. 6.8 the experimental data is shown. All graphs in Fig. 6.8 show the peak frequency as function of resting radius of the bubble. For comparison, the Minnaert frequency (Eq. (6.8)) is also drawn in the graphs. Fig. 6.8A shows the peak frequency which was determined using the microbubble spectroscopy

method. Fig. 6.8B is determined using the chirp resonance – power spectrum method, and Fig. 6.8C is also with chirp resonance with the phase difference method. In all three graphs, the three categories are displayed. It can be seen, in all three graphs, that the peak frequency decreases with increasing oscillation amplitude. Fig. 6.8D contains peak frequency data from category II, derived with the three methods (this corresponds with the diamond shaped symbols in Fig. 6.8A, B and C). All these datapoints collapse onto a single curve.

6.5 Difference between up sweep and down sweep chirps

So far, the difference between up sweep chirp and down sweep chirp has not been discussed. If we take a close look at Fig. 6.7, we see that an up sweep and a down sweep chirp do not lead to the exact same value for the peak frequency. If we study individual $R(t)$ curves, we see that in some cases the response is quite different, due to the nonlinear bubble response.

New imaging modes, including pulse inversion [17, 18], second or higher harmonic imaging [19, 20], and subharmonic imaging [21, 22], exploit the nonlinear properties of bubbles. In pulse inversion, an ultrasound wave followed by a delayed phase-inverted replica is transmitted into tissue. For a linear medium, the echo from the second wave is an inverted copy of the response from the first wave, and the sum of the two responses is zero. For a nonlinear microbubble system, the sum is not zero and the residue indicates the presence of microbubbles. Pulse inversion achieves substantial improvement of the image quality in echoscopy.

As a result of the nonlinear bubble behavior, the bubble responses on chirp driving signals are not time-reversed replicas [23–25]. The nonlinear bubble response on up sweep chirps and down sweep chirps, named chirp reversal, can be of potential interest in contrast imaging as well. In the following sections we will investigate the bubble response difference in greater detail, both in simulations and in experiments.

6.5.1 Simulations

The Rayleigh–Plesset equation was solved numerically for free gas microbubbles. In this section, we chose a different window function over

the chirps. In contrast imaging, there is a tradeoff between wave duration and axial resolution: increasing the wave duration decreases the axial resolution. We used a shorter wave duration, and to minimize sidelobes in the frequency spectrum even more than the Tukey window (see Eq. (6.3)) does, we therefore replaced the Tukey window with the following Gaussian window:

$$w(t) = \exp\left(-\frac{1}{2}\left(\alpha \frac{t}{T/2}\right)^2\right) \tag{6.10}$$

The α, which is the reciprocal of the standard deviation, a measure of the width of its Fourier transform, and the T which represents a time period, were tuned to get a linear frequency sweep magnitude of 850 kHz centered around the center frequency in the chirp transmit signals. This corresponds to a bandwidth of 50% for a center frequency of 1.7 MHz.

Up sweep and down sweep chirps of 1.7 MHz and 10 kPa were used in transmit. The corresponding resonance radius of the 1.7 MHz chirp center frequency is $R_{res} \approx 2.3$ μm. Here, we distinguish four different cases.

I. The bubble radius is below the resonance radius ($R_0 < R_{res}$ or $f_{center} > f_{res}$).

II. The bubble radius is at the resonance radius ($R_0 \approx R_{res}$ or $f_{center} \approx f_{res}$).

III. The bubble radius is above the resonance radius ($R_0 > R_{res}$ or $f_{center} < f_{res}$).

IV. The bubble radius is far away from the resonance radius ($R_0 \gg R_{res}$ and $R_0 \ll R_{res}$ or $f_{center} \ll f_{res}$ and $f_{center} \gg f_{res}$).

Microbubbles of 1.9 μm, 2.3 μm, 3.8 μm, and 1.0 μm were considered. The simulated radii correspond to bubbles below resonance size, at resonance, above and far away from resonance size.

Figure 6.9 shows the response of a 1.9 μm bubble to an up sweep chirp (Fig. 6.9B) and down sweep chirp (Fig. 6.9D). This is an example of case I, with $R_0 < R_{res}$. The curves show a longer bubble oscillation when frequencies sweep increasing compared to the decreasing frequency sweep.

This observation is reversed for the 3.8 μm radius bubble (Fig. 6.10) where the up sweep chirp signal produces shorter bubble oscillations compared to the down sweep chirp. This is an example of case III, with $R_0 > R_{res}$.

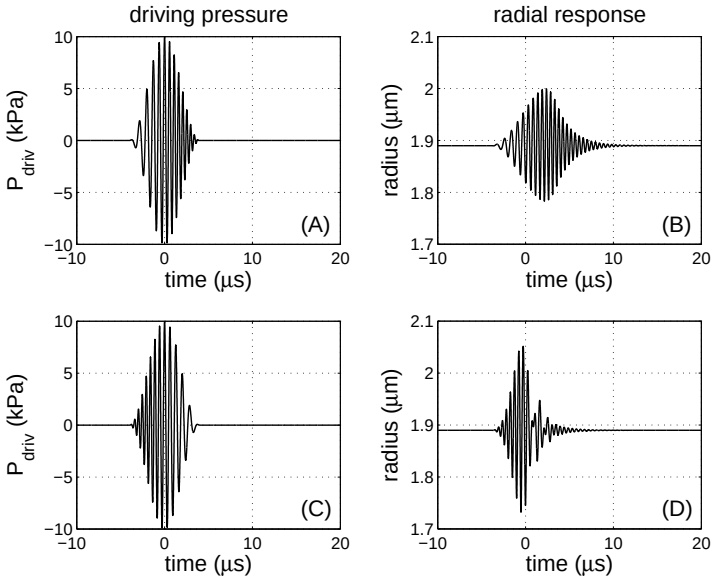

Figure 6.9: Simulated radius-time curves of a 1.9 μm free microbubble. (A) The driving pressure (1.7 MHz, 10 kPa) of an up sweep chirp, and (C) a down sweep chirp. The corresponding $R(t)$ curves are shown in (B) and (D). This is an example of case I.

The oscillations of a resonant bubble (case II, $R_0 = R_{res}$, radius of 2.3 μm) excited by an up sweep chirp and down sweep chirp are given in Fig. 6.11 and appear to be almost identical.

Bubbles that are far away from resonance give identical responses to both chirps as shown in Fig.6.12 for a microbubble of 1.0 μm radius. The results from these simple simulations indicate that bubbles at resonance or far away from resonance do not sense differences between up sweep and down sweep excitation signals. However bubbles close to resonance respond differently to chirps with up sweep and down sweep frequencies.

To quantitatively describe the response difference, we calculate the cross-correlation between the up sweep response and the down sweep response. Since a cross-correlation on two signals gives a value close to one if signals are similar, and a value close to zero if signals are not similar, we expect to see two dips in the cross-correlation signal: one dip just below, and one dip just above the resonance frequency. We calculate the response of a 2 μm bubble on up and down sweep chirps with a frequency

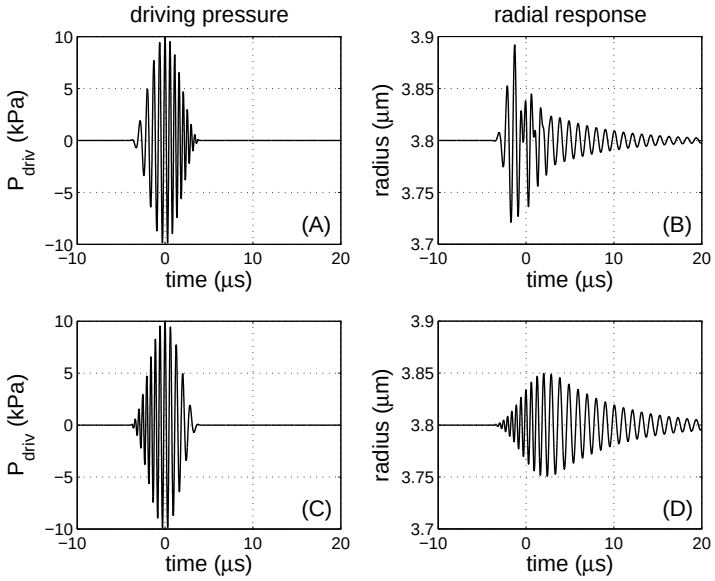

Figure 6.10: Simulated radius-time curves of a 3.8 μm free microbubble. (A) The driving pressure (1.7 MHz, 10 kPa) of an up sweep chirp, and (C) a down sweep chirp. The corresponding $R(t)$ curves are shown in (B) and (D). This is an example of case III.

between 500 kHz and 6 MHz, and with a driving pressure of 10 kPa.

We choose for cross-correlation over subtraction, which is also a measure of response difference, because this method is less dependent on timing. Using subtraction, the exact position of the responses in time is necessary for an accurate measure of response difference. In simulations, this is not a problem. However, in experiments, due to inhomogeneities, the response can be slightly delayed. This would be falsely seen as a response difference.

We name the up sweep response u, and the down sweep response d. Both signals have a length of N samples. The calculated cross-correlation is then given by

$$C_{ud}(m) = \begin{cases} \sum_{n=0}^{N-m-1} u_{n+m} d_n & m \geq 0 \\ C_{du}(-m) & m < 0 \end{cases} \tag{6.11}$$

Then, the sequence is normalized, so that autocorrelations at zero lag are

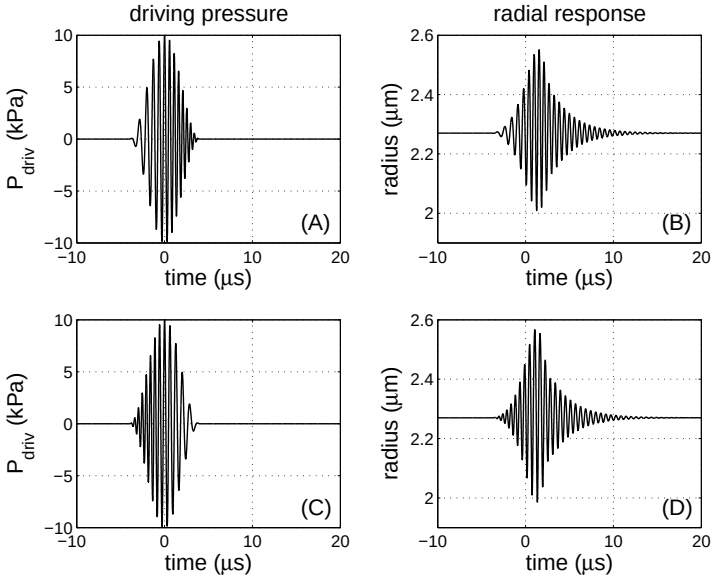

Figure 6.11: Simulated radius-time curves of a 2.3 μm free microbubble. (A) The driving pressure (1.7 MHz, 10 kPa) of an up sweep chirp, and (C) a down sweep chirp. The corresponding $R(t)$ curves are shown in (B) and (D). This is an example of case II.

identical to 1.

The cross-correlation of the up sweep response with the time-reversed down sweep response is shown in Fig. 6.13. A correlation of 1 corresponds to identical signals. As expected, there are two dips observed in the cross correlation signal, one dip just below the resonance frequency, and one dip just above the resonance frequency. For a bubble with a radius of 2 μm, the resonance frequency is 2.0 MHz. The dips correspond to the response differences in case I and case III. When the center frequency of the chirp is just below the resonance frequency ($f_{center} < f_{res}$), the cross-correlation amplitude decreases to 0.73 (case III). At resonance (case II), the cross-correlation amplitude is approximately 0.86. When the center frequency of the chirp is slightly bigger than the resonance frequency (case I), the cross-correlation amplitude decreases to 0.58. Far away from resonance (case IV), either above or below, the cross-correlation goes to 1.

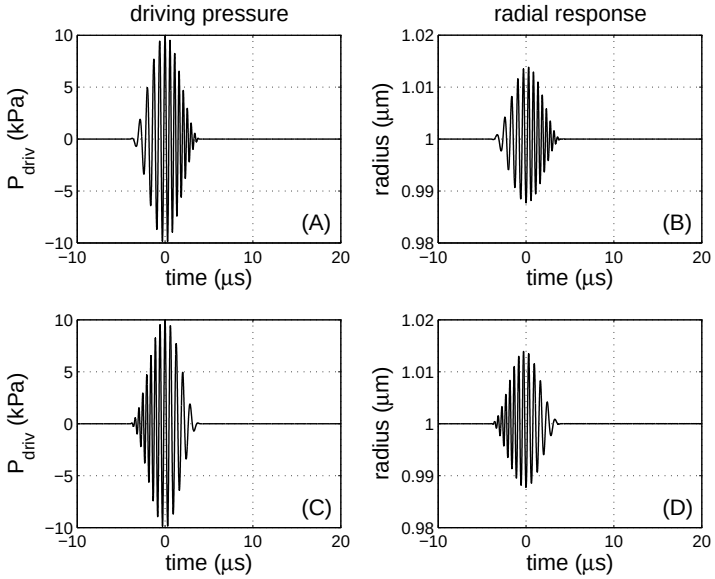

Figure 6.12: Simulated radius-time curves of a 1.0 μm free microbubble. (A) The driving pressure (1.7 MHz, 10 kPa) of an up sweep chirp, and (C) a down sweep chirp. The corresponding $R(t)$ curves are shown in (B) and (D). This is an example of case IV.

6.5.2 Experimental results

Hydrophone calibration

The chirp reversal experiments were performed with the setup described in Sec. 6.3.1. Using a needle hydrophone (Precision Acoustics, Dorset, UK), the transducer was calibrated from 0.7 MHz to 6 MHz, using bursts of fixed frequency. With the calibration, the chirp voltage signals were modified to give the chirp pressure signals the required shape. As a check, the chirp pressure signals were measured with the hydrophone again. Figure 6.14 shows examples of transmitted chirps, as measured in the focus of the transducer. Figure 6.14A displays a measured up sweep chirp with a center frequency of 1.7 MHz and 50% bandwidth at an amplitude of 60 kPa approximately. Figure 6.14B shows an identical chirp with frequencies sweeping down. The measurements demonstrates also that the single element transducer does not affect the transmitted chirp waveforms.

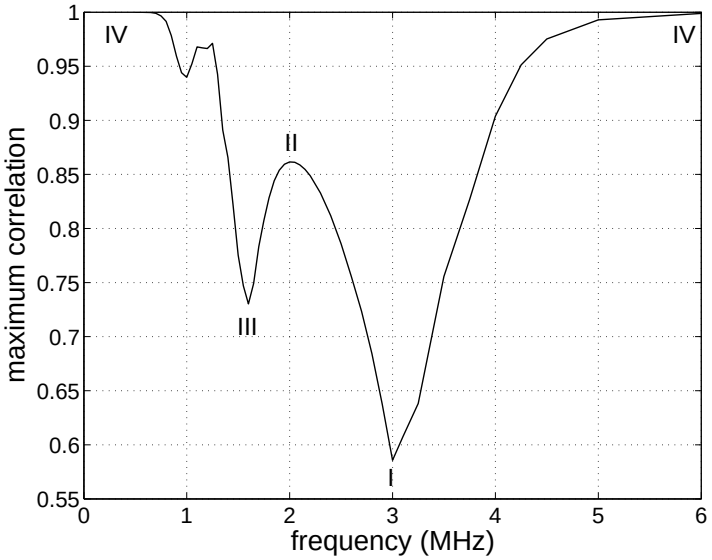

Figure 6.13: Simulation result: the cross-correlation between an up sweep chirp response and a down sweep chirp response, of a 2 μm bubble. The driving ultrasound consists of up and down sweep chirps with a frequency between 500 kHz and 6 MHz, and with a driving pressure of 10 kPa. Note two dips in the cross-correlation, just before resonance and just above resonance, indicating the two spots where the response signals are the most asymmetric. The 4 four different cases are in the figure indicated with labels.

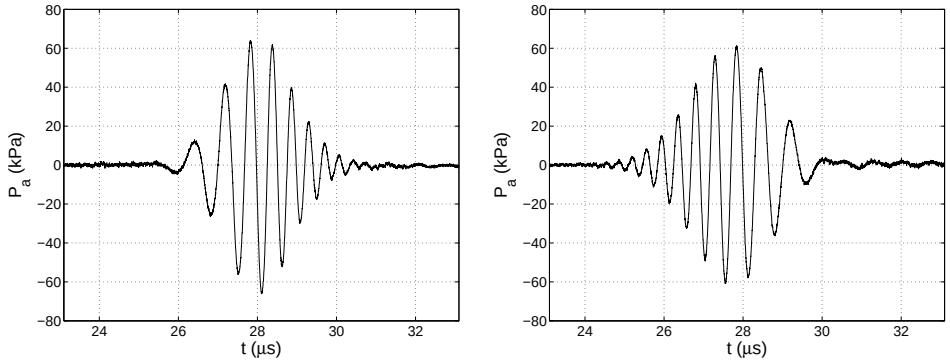

(A) Up sweep chirp (B) Down sweep chirp

Figure 6.14: Example hydrophone measurements of the actual transmitted up sweep (A) and down sweep (B) chirps with center frequency of 1.7 MHz and 50% bandwidth.

Chirp reversal experiments

In Fig. 6.15, we present the result obtained for a BR-14 microbubble with a radius of 2.55 μm. The resonance frequency of such a microbubble is around 2 MHz, according to microbubble spectroscopy experiments of Ch. 3 or [5]. The bubble is successively insonified with the following chirps: an up sweep chirp at 1.3 MHz, 120 kPa, a down sweep chirp at 1.3 MHz, 120 kPa, an up sweep chirp at 2.5 MHz, 120 kPa, a down sweep chirp at 2.5 MHz, 120 kPa and an up sweep chirp at 1.3 MHz, 120 kPa. The first pair of transmitted chirps have center frequencies below the resonance frequency of the bubble, the next pair of chirps have a center frequency above the resonance frequency of the microbubble, and the last chirp, as a control, is identical to the first chirp.

The first response curves (Fig. 6.15B & D) demonstrate a difference in the bubble response where the up sweep chirp generates a shorter oscillation of the bubble, whereas the down sweep chirp produces a much longer bubble response. They are an experimental example of case III. The initial frequencies of the transmitted up sweep chirp are close to the resonance frequency of the microbubble, while frequencies transmitted last are far away from the microbubble's resonance frequency. This causes the bubble oscillation to damp out, generating a short overall response. On the other hand, the down sweep chirp starts with frequencies further from resonance and ends with frequencies that are close to the microbubble's resonance frequency. It is responsible for generating different bubble responses for up sweep and down sweep chirps. This causes the bubble oscillation to sweep up into resonance oscillations, and translates into longer and larger radial excursions.

The second pair of response curves (Fig. 6.15F & H) show the reversed behavior. These are experimental examples of case I. The up sweep chirp causes a longer oscillation of the bubble, whereas the down sweep chirp generates a much shorter response. Here, the initial frequencies of the transmitted up sweep chirp are away from the resonance frequency of the bubble, which causes the oscillation to damp out. On the other hand, the down sweep chirp starts with frequencies close to the resonance frequency of the bubble, which causes the bubble oscillation to sweep up.

The bubble was successively insonified with a fifth and final chirp, which is a copy of the first chirp. The dashed line in Fig. 6.15B is the final up sweep chirp, which is used as a check. It is seen that the response is identical to the first up sweep chirp (solid line). This demonstrates that the microbubble's response has not been modified

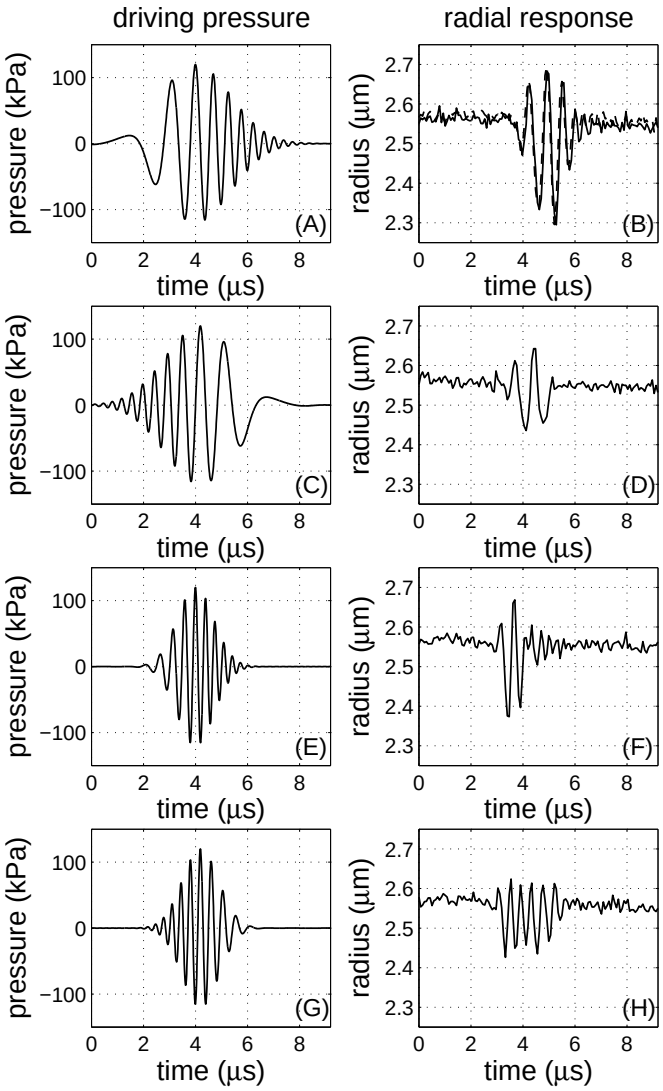

Figure 6.15: Experimental results: In the left column the driving chirps are shown, in the right column the corresponding measured $R(t)$-curves are displayed. The examined BR-14 microbubble had a radius of 2.55 μm. The bubble was excited with (A) an up sweep chirp of 1.3 MHz, 120 kPa, (C) a down sweep chirp of 1.3 MHz, 120 kPa, (E) an up sweep chirp of 2.5 MHz, 120 kPa and (G) a down sweep chirp of 2.5 MHz, 120 kPa. Furthermore, in (B) both the response on the first up sweep chirp (solid line) and the check up sweep chirp (dashed line) are shown. Note that (B) and (D) are an example of case III, while (F) and (H) are an example of case I.

during the experiment.

Similar results are obtained for a smaller microbubble with a radius of 1.9 μm, excited at chirps of 1.75 MHz and 2.8 MHz, both at 100 kPa. The responses are given in Fig. 6.16. The resonance frequency of such a bubble is 2.5 MHz. The transmitted chirps in Fig. 6.16A & C are thus below the resonance frequency (case III), and the chirps in Fig. 6.16E & G are above the resonance frequency (case I).

Figure 6.17 shows an example obtained with a much smaller microbubble excited with chirps of 1.7 MHz and 120 kPa. This is an experimental example of case IV. The resonance frequency of such a bubble is higher than 3.5 MHz, indicating that both up sweep and down sweep chirps contain a frequency bandwidth far away from the resonance of the microbubble. This is demonstrated in the radius-time curve where both chirps produce similar microbubble vibrations.

6.5.3 Conclusions on chirp reversal

The optical observations show that a contrast microbubble responds differently to a chirped signal depending whether the chirp contains up sweep or down sweep frequencies. The resonance frequency of the microbubble plays a major role.

When the transmitted center frequency is higher than the resonance frequency of the microbubble (case I), up sweep chirp generates a much shorter signal. This might be ascribed to the fact that in up sweep chirp signal, frequencies from the lower bandwidth are transmitted first and induce the bubble into resonance behavior. However, this resonance behavior is immediately damped and submerged by responses from frequency components of the upper bandwidth, which insonify the microbubble during the latest portion of the chirp signal. These high frequencies are away from the microbubble resonance. These features are shown in simulations in Fig. 6.9 and in experiments in Figs. 6.15F & H, and 6.16F & H.

When the resonance frequency of the microbubble is higher than the transmitted frequency (case III), the microbubble will also react differently to up sweep chirp and down sweep chirp. However in this situation, the oscillations will be longer for up sweep chirp than down sweep chirps. This is demonstrated in simulations in Fig. 6.10 and experimentally in Figs. 6.15B & D, and 6.16B & D, where the microbubbles with resonance frequencies higher than the transmitted frequency oscillate longer under a down sweep chirp excitation compared to an up sweep chirp.

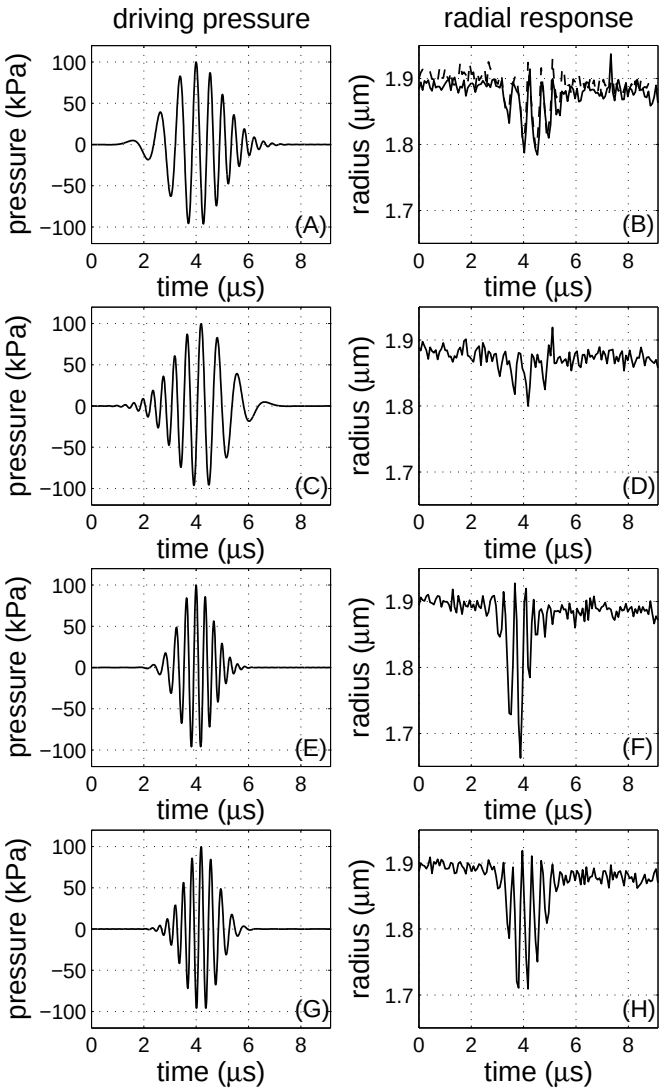

Figure 6.16: Experimental results: In the left column the driving chirps are shown, in the right column the corresponding measured $R(t)$-curves are displayed. The examined BR-14 microbubble had a radius of 1.9 μm. The bubble was excited with (A) an up sweep chirp of 1.75 MHz, 100 kPa, (C) a down sweep chirp of 1.75 MHz, 100 kPa, (E) an up sweep chirp of 2.8 MHz, 100 kPa and (G) a down sweep chirp of 2.8 MHz, 100 kPa. Furthermore, in (B) both the response on the first up sweep chirp (solid line) and the check up sweep chirp (dashed line) are shown. Note that (B) and (D) are an example of case III, while (F) and (H) are an example of case I.

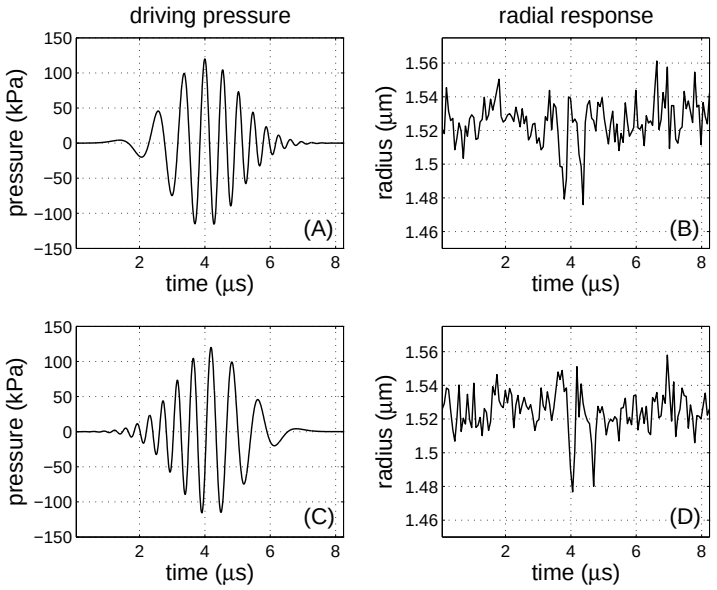

Figure 6.17: Experimental results: In the left column the driving chirps are shown, in the right column the corresponding measured $R(t)$-curves are displayed. The examined BR-14 microbubble had a radius of 1.5 μm. The bubble was excited with (A) an up sweep chirp of 1.7 MHz, 120 kPa, (C) a down sweep chirp of 1.7 MHz, 120 kPa. Note that (B) and (D) are an example of case IV.

For microbubbles with resonance frequencies far away from the center frequency of the excitation chirp, we do not observe differences in the bubble behavior for up sweep and down sweep chirps. In this case, the microbubble resonates far away from the applied frequency bandwidth and thus responds similarly to both chirps. This was shown in simulations in Fig. 6.12, and experimentally in Fig. 6.17.

Although the measurements and simulations were carried out on individual microbubbles, we believe that these results might be applied for contrast imaging in order to improve the contrast to tissue ratio since tissue scatterers do not resonate and thus are expected to provide the same response to both up sweep and down sweep chirps. This however needs more experimental verification using in-vitro setups and acoustic measurements. Exploitation of chirp reversal for contrast imaging provides other advantages. This method should operate in linear mode where low acoustic pressures are transmitted. Hence

microbubble destruction is avoided and the nonlinearity of tissue is reduced. Moreover, the full frequency bandwidth of the transducer can be exploited. Using chirps provides additional signal to noise ratio improvements since longer waveforms are used [26, 27]. In order to test our approach for contrast detection, we need to further explore the influence of microbubble size distribution on the obtained results since our current data are obtained on individual microbubbles.

6.6 Conclusions

Simulations were performed using the chirp resonance methods to derive the peak frequency of a contrast agent microbubble to determine the stability in experiments. Using a harmonic oscillator model, we concluded the method can derive the peak frequency of a bubble with an accuracy of 5%, even when the radius-time curve consists of 100 datapoints. The method is also stable to noise.

In experiments a difference between microbubble spectroscopy and the chirp resonance methods was observed using similar driving pressure amplitude. The peak frequency determined with the chirp resonance methods is lower than the data determined with the microbubble spectroscopy method. The difference was attributed to the difference in radial oscillation amplitude.

An amplitude oscillation dependence of the peak frequency was investigated. The eigenfrequency is a bubble property, which only depends on liquid density, ambient (and vapor) pressure, surface tension and a polytropic exponent. When a bubble oscillates with very high oscillation amplitude, the natural period of oscillation of the bubble increases. The frequency, with which the bubble is then oscillating, we name the peak frequency. Both in simulations and in experiments we see that the peak frequency of a bubble decreases with increasing oscillation amplitude.

Simulations were performed on a $R = 3$ μm bubble. With three methods, microbubble spectroscopy, chirp resonance power spectra analysis, and chirp resonance phase difference analysis the peak frequency was determined. All methods can determine the peak frequency within 2.5% of the analytically determined peak frequency, even up to very nonlinear oscillations with a normalized amplitude $A_{norm} = (R_+ - R_-)/R_0$ of 1.

Experiments were performed with all three methods. The decrease of the peak frequency as function of increasing oscillation amplitude is experimentally observed. All three methods report the same peak

frequency as function of oscillation amplitude.

And finally, we observed differences in the radial response on up sweep chirps and down sweep chirps. These differences, due to nonlinear behavior of the bubbles, can be exploited in contrast imaging. Simulations and experiments show that the asymmetry in bubble response is maximum just below and just above the resonance frequency of the bubble. At resonance, and far away from resonance, the bubble response on up sweep and down sweep chirps is similar.

6.7 Appendix: Analytical expression of the peak frequency

6.7.1 Introduction

The governing equations of oscillating gas bubble are highly nonlinear, and cause difficult mathematical problems. Therefore, many of the existing studies are based on linearized analysis [11] or on numerical computations [10].

In this appendix, we describe our calculations on the shift of the peak frequency from eigenfrequency to lower frequencies of a free gas bubble. From numerical simulations and from experiments, we see the peak frequency decrease with increasing pressure. Since the methods to derive the peak frequency from numerical data or experimental data (discussed in Ch. 3 and Ch. 6) are based on fitting with linear models, there arise deviations at higher pressures. So whether the measured peak frequency decrease is real, or an artifact of the fitting, can be determined by an analytical solution of the peak frequency of the bubbles.

6.7.2 Description of the calculations

First, we retain from the Rayleigh–Plesset equation the essential terms. With this equation, we will explain our calculations. We begin with:

$$\ddot{R}R + \frac{3}{2}\dot{R}^2 = \frac{P_g - P_0}{\rho} \tag{6.12}$$

Here P_g is the gas pressure in the bubble, and P_0 is the ambient pressure. They are related by the following relation: $P_g = P_0(R_0/R)^{3\gamma}$. If we now take $\gamma = 4/3$, the relation becomes $P_g = P_0(R_0/R)^4$. Different substitutions are possible now [28], yet we now write $\ddot{R} = \frac{\mathrm{d}}{\mathrm{d}t}\dot{R}$ and

since R is only a function of t we swap integration variable t for R. So $\frac{\mathrm{d}}{\mathrm{d}t}\dot{R} = \dot{R}\frac{\mathrm{d}}{\mathrm{d}R}\dot{R} = \frac{1}{2}\frac{\mathrm{d}}{\mathrm{d}R}\dot{R}^2$. The left hand side of the equation can then we rewritten as $\frac{1}{2}R\frac{\mathrm{d}}{\mathrm{d}R}\dot{R}^2 + \frac{3}{2}\dot{R}^2$, which equals $\frac{1}{2R^2}\frac{\mathrm{d}}{\mathrm{d}R}(R^3\dot{R}^2)$, and thus Eq. (6.12) becomes:

$$\frac{\mathrm{d}}{\mathrm{d}R}(R^3\dot{R}^2) = \frac{2P_0}{\rho}(\frac{R_0^4}{R^2} - R^2). \tag{6.13}$$

Now, we integrate Eq. (6.13) from the minimum radius the bubble will assume, R_-, to the bubble radius R. Equation (6.13) becomes:

$$R^3\dot{R}^2 = \frac{2P_0}{\rho}\int_{R_-}^{R}(\frac{R_0^4}{\tilde{R}^2} - \tilde{R}^2)\mathrm{d}\tilde{R}, \tag{6.14}$$

This equation can also be derived another way by considering the energy balance [29]. We start with the velocity potential Φ in the fluid around a bubble, which is given at any point in the fluid at distance r from the bubble center by:

$$\Phi = -R^2\frac{\dot{R}}{r} \tag{6.15}$$

The kinetic energy E_{kin} of the fluid is given by the well-known integral

$$E_{kin} = -\frac{\rho}{2}\int_A \Phi\frac{\partial\Phi}{\partial r}\mathrm{d}A \tag{6.16}$$

over the surface $A = 4\pi r^2$ of the bubble, where $\partial\Phi/\partial r$ is the derivative of Φ in the radial direction. The kinetic energy is thus:

$$E_{kin} = 2\pi\rho R^3\dot{R}^2 \tag{6.17}$$

With an instantaneous volume V, we consider the potential energy from the minimum bubble volume V_- is given by:

$$E_{pot} = \int_{V_-}^{V} P\mathrm{d}V \tag{6.18}$$

Rewriting the equation for the radial variable $\tilde{R}$, and using $P = P_g - P_0$, Eq. (6.18) becomes:

$$E_{pot} = \int_{V_-}^{V}(P_0(\frac{R_0}{R})^4 - P_0)\mathrm{d}V = 4\pi P_0\int_{R_-}^{R}(\frac{R_0^4}{\tilde{R}^2} - \tilde{R}^2)\mathrm{d}\tilde{R} \tag{6.19}$$

The total energy remains the same, so potential energy must be equal to the kinetic energy ($E_{kin} = E_{pot}$):

$$R^3\dot{R}^2 = \frac{2P_0}{\rho}\int_{R_-}^{R}(\frac{R_0^4}{\tilde{R}^2} - \tilde{R}^2)\mathrm{d}\tilde{R}, \tag{6.20}$$

and this equation is similar to Eq. (6.14).

We can rewrite this to:

$$R^3\dot{R}^2 = \frac{2P_0}{\rho}\left(R_0^4(\frac{1}{R_-}-\frac{1}{R})-\frac{1}{3}(R^3-R_-^3)\right). \tag{6.21}$$

The bubble wall velocity reaches zero again, when the bubble reaches it maximum size, R_+. Solving Eq. (6.21) for R_0^4 gives $R_0^4 = \frac{1}{3}(R_-^2+R_+R_-+R_+^2)R_+R_-$. Equation (6.21) then becomes:

$$\dot{R}^2 = \frac{2P_0}{\rho R^3}\left(\frac{1}{3}(R_-^2+R_+R_-+R_+^2)R_+R_-(\frac{1}{R_-}-\frac{1}{R})-\frac{1}{3}(R^3-R_-^3)\right), \tag{6.22}$$

or:

$$\dot{R}^2 = \frac{2P_0}{3\rho}\frac{1}{R^4}\big((R_+-R)(R-R_-)(R^2+RR_++RR_-+R_-^2+R_+R_-+R_+^2)\big). \tag{6.23}$$

As a check, we see that the bubble wall velocity reaches zero ($\dot{R}=0$) when the bubble reaches its minimum radius ($R=R_-$) or its maximum radius ($R=R_+$).

We now have an expression of $\dot{R}$ in terms of R, R_- and R_+. We integrate the bubble radius from R_- to R_+, and calculate the time this takes. This equals one half of an oscillation period. From that we can easily calculate the oscillation frequency. So we integrate this expression, and get:

$$\int_0^{T/2}\mathrm{d}t = \frac{T}{2} = \int_{R_-}^{R_+}\frac{AR^2\mathrm{d}R}{\sqrt{BR^4+CR+D}} \tag{6.24}$$

where A, B, C, and D are given by the following expressions:

$$A = \sqrt{\frac{3\rho}{2P_0}} \tag{6.25}$$

$$B = -1 \tag{6.26}$$

$$C = R_-^3+R_+R_-^2+R_+^2R_-+R_+^3 \tag{6.27}$$

$$D = -(R_+^2+R_+R_-+R_-^2)R_+R_- \tag{6.28}$$

This integral can be solved by the symbolic toolbox of Matlab or by Maple, and then be evaluated as a function of oscillation amplitude (R_+ and R_-). The evaluation of Eq. (6.24) is shown in Fig. 6.18. Note that for $R_0-R_- = R_+-R_0 = 0$, the oscillation frequency falls onto the eigenfrequency of the bubble.

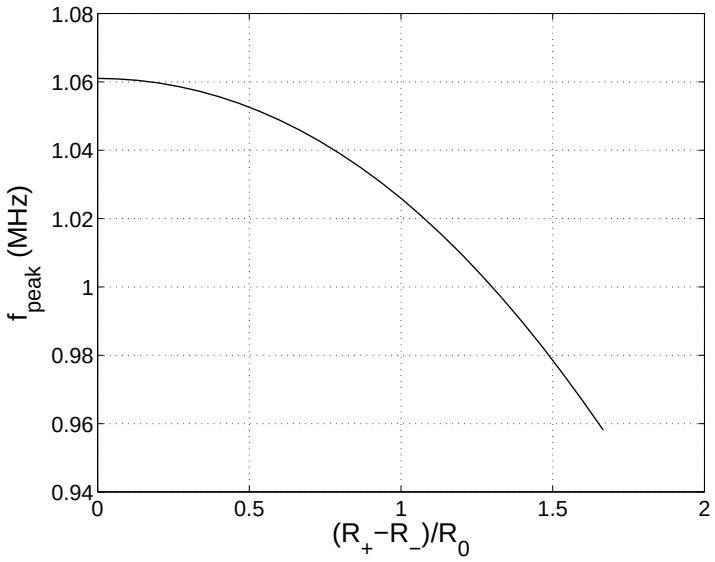

Figure 6.18: Evaluation of the solution of Eq. (6.24), evaluated at R_0=3 μm, versus the normalized amplitude $A_{norm} = (R_+ - R_-)/R_0$.

6.7.3 Coupling the oscillation amplitude to the driving pressure

To couple the oscillation amplitude with the driving pressure, numerical simulations are performed with Matlab's ode45-solver, which can solve Eq. (6.12) numerically. Finding the correct peak frequency at a certain driving pressure, is an iterative process. First, an estimation was made of the peak frequency. Then, at that frequency, with a certain driving pressure, Eq. (6.12) was solved for a burst of 100 cycles. When the initial transient effects have damped out, the maximum radius R_+ and the minimum radius R_- were taken from the $R(t)$-curve. With these values, the peak frequency can be calculated, by solving Eq. (6.24). Iteratively, a convergence can be found to the correct peak frequency.

6.7.4 Extending the basic RP equation

To improve our simulations with the RP equation, Eq. (6.12) can be extended with more terms without altering the methods and calculations described above. The value for κ can also be changed to an arbitrary value without analytical problems. Only the viscous damping term $(4\mu\dot{R}/R)$

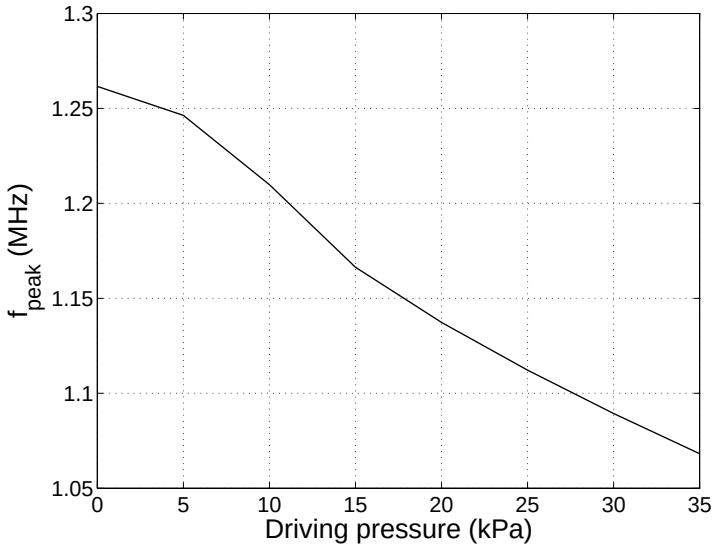

Figure 6.19: Evaluation of the solution of the half period integral, evaluated at R_0=3 μm, for driving pressure amplitudes from 0 to 35 kPa.

complicates the calculations extensively. We choose to neglect this term, since it will not change the peak frequency significantly.

Equation (6.12) will then change to

$$\ddot{R}R + \frac{3}{2}\dot{R}^2 = \frac{1}{\rho}\left\{\left(P_0 + \frac{2\sigma}{R_0} - P_v\right)\left(\frac{R_0}{R}\right)^{3\kappa} + P_v - \frac{2\sigma}{R} - P_0\right\} \qquad (6.29)$$

The integral of the half period (the more complex equivalent of Eq. 6.24), is too lengthy to display here. With Maple, this integral can be solved. The curve in Fig. 6.19 was constructed iteratively at each pressure, by successively estimating the peak frequency, numerically finding the radial amplitudes R_- and R_+, and calculating the corresponding peak frequency; thus converging to the correct peak frequency at that pressure. For a driving pressure amplitude of 0 kPa, the oscillation frequency becomes the Minnaert frequency (Eq. (6.8)).

References

[1] P.N.T. WELLS, *Biomedical Ultrasonics*. London: Academic Press, (1977).

[2] N. DE JONG, *Acoustic properties of ultrasound contrast agents*, Ph.D thesis, Erasmus University Rotterdam (1993).

[3] L. HOFF, *Acoustic Characterization of Contrast Agents for Medical Ultrasound Imaging*, Kluwer Academic Publishers, Dordrecht (2001).

[4] A. L. KLIBANOV, "Ultrasound contrast agents: Development of the field and current status", Top. Curr. Chem. **222**, 73–106 (2002).

[5] S.M. VAN DER MEER, B. DOLLET, M. VOORMOLEN, C.T. CHIN, A. BOUAKAZ, N. DE JONG, M. VERSLUIS, D. LOHSE, "Microbubble spectroscopy of ultrasound contrast agents", J. Acoust. Soc. Am. **121**(1), 648–656 (2007).

[6] J.M. BORSBOOM, C.T. CHIN, N. DE JONG, "Nonlinear coded excitation method for ultrasound contrast imaging", Ultrasound Med. Biol. **29**(2), 277–284 (2003).

[7] K. CHETTY, J.V. HAJNAL, R.J. ECKERSLEY, "Investigating the nonlinear microbubble response to chirp encoded, multipulse sequences.", Ultrasound Med. Biol. **32**(12), 1887–1895 (2006).

[8] T.G. LEIGHTON, *The Acoustic Bubble*. London: Academic Press, (1994).

[9] S. HILGENFELDT, D. LOHSE, AND M. ZOMACK, "Response of bubbles to diagnostic ultrasound: a unifying theoretical approach", Eur. Phys. J. B **4**, 247–255 (1998).

[10] W. LAUTERBORN, "Nonlinear oscillations of gas bubbles", J. Acoust. Soc. Am. **59**(2), 283–293 (1976).

[11] M. MINNAERT, "On musical air-bubbles and the sounds of running water." Phil. Mag. **16**, 235–248 (1933).

[12] C. T. CHIN, C. LANCÉE, J. BORSBOOM, F. MASTIK, M. E. FRIJLINK, N. DE JONG, M. VERSLUIS, D. LOHSE, "Brandaris 128: A digital 25 million frames per second camera with 128 highly sensitive frames", Rev. Sci. Instrum. **74**(12), 5026–5034 (2003).

[13] M. SONKA, V. HLAVAC, R. BOYLE, *Image processing, analysis, and machine vision*, 2nd ed. Pacific Grove, CA: PWS Pub., (1999).

[14] M. SCHNEIDER, A. BROILLET, P. BUSSAT, N. GIESSINGER, J. PUGINIER, R. VENTRONE, AND F. YAN, "Gray-scale liver enhancement in VX2 tumor-bearing rabbits using BR14, a new ultrasonographic contrast agent", Invest. Radiol. **32**(7), 410–417 (1997).

[15] A. PROSPERETTI, "Nonlinear oscillations of gas bubbles in liquids: steady-state solutions", J. Acoust. Soc. Am. **56**(3), 878–885 (1974).

[16] A. PROSPERETTI, "Nonlinear oscillations of gas bubbles in liquids: transient solutions and the connection between subharmonic signal and cavitation", J. Acoust. Soc. Am. **57**(4), 810–821 (1975).

[17] P. N. BURNS, S. R. WILSON, D. H. SIMPSON, "Pulse inversion imaging of liver blood flow: Improved method for characterizing focal masses with microbubble contrast", Invest Radiol. **35**, 58–71 (2000).

[18] K. E. MORGAN, M. AVERKIOU, K. FERRARA, "The effect of the phase of transmission on contrast agent echoes", IEEE Trans. Ultrason., Ferroelect., Freq. Contr. **45**, 872–875, (1998).

[19] F. FORSBERG, B. B. GOLDBERG, Y. Q. WU, J. B. LIU, D. A. MERTON, N. M. RAWOOL, "Harmonic imaging with gas-filled microspheres: Initial experiences", Int. J. Imaging Syst. Tech. **8**, 69–81 (1997).

[20] N. DE JONG, A. BOUAKAZ, F. J. TEN CATE, "Contrast harmonic imaging", Ultrasonics **40**, 567–573 (2002).

[21] O. LOTSBERG, J. M. HOVEM, B. AKSUM, "Experimental observation of subharmonic oscillations in Infoson bubbles", J. Acoust. Soc. Amer. **99**, 1366–1369 (1996).

[22] W. T. SHI, F. FORSBERG, A. L. HALL, R. Y. CHIAO, J. B. LIU, S. MILLER, K. E. THOMENIUS, M. A. WHEATLEY, B. B. GOLDBERG, "Subharmonic imaging with microbubble contrast agents: Initial results", Ultrason. Imag. **21**, 79–94 (1999).

[23] A. BOUAKAZ, "Chirp reversal ultrasound contrast imaging", Patent no. WO2007015176, France, Inserm, (2005).

[24] Y. SUN, S. ZHAO, P. A. DAYTON, K. W. FERRARA, "Observation of contrast agent response to chirp insonation with a simultaneous optical-acoustical system", IEEE Trans. Ultrason. Ferroelect. Freq. Contr. **53**(6), 1130–1137 (2006).

[25] Y. SUN, D. E. KRUSE, K. W. FERRARA, "Contrast Imaging with Chirped Excitation", IEEE Trans. Ultrason. Ferroelectr. Freq. Control **54**(3), 520–529 (2007).

[26] R. Y. CHIAO, X. HAO, "Coded excitation for diagnostic ultrasound: a system developer's perspective", IEEE Trans. Ultrason. Ferroelectr. Freq. Control **52**(2), 160–170 (2005).

[27] T. MISARIDIS, J. A. JENSEN, "Use of modulated excitation signals in medical ultrasound. Part I: Basic concepts and expected benefits", IEEE Trans. Ultrason. Ferroelectr. Freq. Control **52**(2), 177–191 (2005).

[28] D.R. CHILDS, "Exact solution of the non-linear differential equation $R\ddot{R} + 3/2\dot{R}^2 - AR^{-4} + B = 0$", Int. J. Non-Lin. Mech. **8**, 371–379 (1973).

[29] L. VAN WIJNGAARDEN, "One-dimensional flow of liquids containing small gas bubbles", Ann. Rev. Fluid Mech. **4**, 369–396 (1972).

7
Conclusions

In January 2003 the Brandaris 128 high speed camera became operational, opening up a whole new area of research in the diagnostic ultrasound field. With the camera it was possible to study the effect of ultrasound on single oscillating ultrasound contrast agent microbubbles.

So what have we learned from this? First of all, bubbles do not always oscillate symmetrically. Time-resolved bubble dynamics recorded with the camera revealed that nearly 40% of the coated bubbles show 'compression-only' behavior, a highly nonlinear behavior [1]. We attribute this phenomenon to the lipid coating of the bubble. Three additional parameters were introduced to the Rayleigh–Plesset equation to account for the physics of the lipid coating: a buckling surface radius, a shell compressibility and a break-up shell tension. The model predicts compression-only behavior, and the model can also account for aging of the bubble and shell rupture.

Furthermore, we tested a number of methods to determine the eigenfrequency and damping of an oscillating contrast microbubble. Probing microbubbles with different bursts of a fixed frequency, we learned that the shell elasticity increases the resonance frequency compared to the uncoated bubble case and the shell viscosity proves to be a significant source of damping. Moreover, we showed that the shell viscosity increases with the bubble radius and suggested an explanation in terms of surface rheology.

Probing the microbubbles with a chirp signal, we learned that we can determine the eigenfrequency of a bubble or the peak frequency for very large amplitudes and very nonlinear oscillations. This peak frequency was seen to lower with increasing oscillation amplitude.

We learned that bubbles do no always oscillate spherically. Both free floating micrometer sized gas bubbles as well as contrast microbubbles have been seen to oscillate with different surface modes.

In the free floating bubble case, the observed mode number n was found to be linearly related to the resting radius of the bubble. Above the critical threshold for shape oscillations, which is minimum at the resonance of the volumetric radial mode, the mode number n is independent of the forcing pressure amplitude. It was found that a parametric instability is responsible for the shape oscillations.

In the contrast microbubble case, we have learned that they are significantly present in medically relevant ranges of bubble radii and applied acoustic pressures. Several features prove that nonspherical deformations are a parametric instability driven by radial oscillations: they oscillate subharmonically with respect to the applied frequency, they require a finite time to grow, and they develop preferentially at the resonance radius for the radial oscillations.

Finally, we learned that a microbubble responds differently to a chirp signal depending whether the chirp contains up sweep or down sweep frequencies. Here, again the resonance frequency of the microbubble plays a major role: when the transmitted center frequency is higher than the resonance frequency of the microbubble, up sweep chirp generates a much shorter signal than the down sweep chirp. A chirp with a center frequency lower than the resonance frequency causes the reversed effect.

In this context, continued effort is made to understand the bubble dynamics. In all contrast agent microbubble experiments, the microbubbles are resting against the capillary fiber wall or a container wall. This changes the bubble behavior, as we also comment on in Secs. 3.5.2 and 5.4.2. A more detailed discussion is given in [2]. Using an optical tweezer, bubbles can now also be studied away from the wall. This tool allows studies of bubble-wall interaction, and also bubble-bubble interaction. In more detail, this is discussed in [3–5].

Contrast bubble specific behavior, such as a driving pressure amplitude threshold was observed: a bubble does not start to oscillate until a certain driving pressure amplitude is reached. This is discussed in more detail in [6, 7].

How contrast bubble specific behavior, such as an amplitude threshold, surface modes, and 'compression-only' behavior translate into an acoustic response is not known. Acoustic studies of individual microbubbles have until now always been hindered by the ability to isolate a single contrast bubble and by the transducer calibration and its corresponding sensitivity. Performing simultaneous acoustic and optical measurements [8] have revealed that depending on the initial bubble

radius, driving pressure amplitude and frequency, either optical or acoustical methods have a better sensitivity to detect the response of a single microbubble to ultrasound.

References

[1] N. DE JONG, M. EMMER, C. T. CHIN, A. BOUAKAZ, F. MASTIK, D. LOHSE, M. VERSLUIS, ""Compression-only" behavior of phospholipid-coated contrast bubbles", Ultrasound Med. Biol. **33**, 653–656 (2007).

[2] H.J. VOS, B. DOLLET, J.G. BOSCH, M. VERSLUIS, N. DE JONG, "Non-spherical vibrations of microbubbles in contact with a wall — a pilot study at low mechanical index", submitted to Ultrasound Med. Biol.

[3] V. GARBIN, E. FERRARI, D. COJOC, E. DI FABRIZIO, M.L.J. OVERVELDE, S.M. VAN DER MEER, M. VERSLUIS, N. DE JONG, D. LOHSE, "Optical Trapping of Ultrasound Contrast Agent Microbubbles", 2006 IEEE International Ultrasonics Symposium Proceedings.

[4] V. GARBIN, D. COJOC, E. FERRARI, E. DI FABRIZIO, M.L.J. OVERVELDE, S.M. VAN DER MEER, N. DE JONG, D. LOHSE, AND M. VERSLUIS, "Changes in microbubble dynamics near a boundary revealed by combined optical micromanipulation and high-speed imaging", Appl. Phys. Lett. **90**, 114103 (2007).

[5] M.L.J. OVERVELDE, V. GARBIN, B. DOLLET, D. COJOC, E. FERRARI, N. DE JONG, E. DI FABRIZIO, D. LOHSE, AND M. VERSLUIS, "3D optical micromanipulation of ultrasound contrast agents: bubble-wall and bubble-bubble interactions", 2007 International Congress on Acoustics Symposium Proceedings.

[6] M. EMMER, A. VAN WAMEL, D.E. GOERTZ, M. VERSLUIS, AND N. DE JONG, "Threshold behavior of vibrating microbubbles", 2006 IEEE International Ultrasonics Symposium Proceedings.

[7] M. EMMER, A. VAN WAMEL, D.E. GOERTZ, N. DE JONG, "The onset of microbubble vibration", Ultrasound Med. Biol. **33**, 941–949 (2007).

[8] J. SIJL, H.J. VOS, N. DE JONG, D. LOHSE, M. VERSLUIS, "Combined optical and acoustical characterization of individual US contrast microbubbles", 2007 International Congress on Acoustics Symposium Proceedings.

Summary

The Brandaris 128 high speed camera was designed and built in order to analyze the dynamics of single oscillating contrast agent microbubbles under influence of ultrasound. In this thesis we report on our findings.

First, in Ch. 2, a new model was introduced which takes into account the physical properties of a lipid monolayer coating on a gas microbubble. Three parameters describe the properties of the shell: a buckling radius, the compressibility of the shell, and a break-up shell tension. The model presents an original non-linear behavior at large amplitude oscillations, termed compression–only, induced by the buckling of the lipid monolayer. This prediction is validated by experimental recordings with the Brandaris camera, operated at several million frames per second. The effect of aging, or the resultant of repeated acoustic pressure pulses on bubbles, is predicted by the model. Further, the model corrects a flaw in the shell elasticity term previously used in the dynamical equation for coated bubbles. The break-up is modeled by a critical shell tension above which gas is directly exposed to water.

A new optical characterization of the behavior of single ultrasound contrast bubbles is presented in Ch. 3. The method consists of insonifying individual bubbles several times successively sweeping the applied frequency, and to record movies of the bubble response up to 25 million frames/s with the Brandaris camera operated in a segmented mode. The method, termed microbubble spectroscopy, enables to reconstruct a resonance curve in a single run. The data is analyzed through a linearized model for coated bubbles. The results confirm the significant influence of the shell on the bubble dynamics: shell elasticity increases the resonance frequency by about 50%, and shell viscosity is responsible for about 70% of the total damping. The obtained value for shell elasticity is in quantitative agreement with previously reported values. The shell viscosity increases significantly with the radius, revealing a new nonlinear behavior of the phospholipid coating.

Bubbles ultrasonically driven near its resonance frequency can become shape-unstable through a parametric instability. We report optical observations with the Brandaris camera of shape oscillations (mode n = 2 to 6) of single contrast agent microbubbles (in Ch. 5) and micron-sized air bubbles (in Ch. 4) for a range of acoustic pressures. For the air bubbles, the observed mode number n was found to be linearly related to the resting radius of the bubble. Above the critical threshold for shape oscillations, which is minimum at the resonance of the volumetric radial mode, the mode number n is independent of the forcing pressure

amplitude. The microbubble shape oscillations were also analyzed numerically by introducing a small non-spherical linear perturbation into a modified Rayleigh–Plesset model which includes a physical thermal damping mechanism describing heat and mass transport in the thin boundary layer at the bubble to water interface. It was found that a parametric instability is indeed responsible for the shape oscillations and that the new model captures the experimental observations in great detail.

For the contrast agent microbubbles, we define a single, dimensionless deformation parameter, and we quantify the amplitude of nonspherical deformation as a function of bubble radius (between 1.5 and 5 μm) and of acoustic pressure (up to 400 kPa). We notably show that surface modes preferentially develop for a bubble radius corresponding to resonance of radial oscillations. Using optical tweezers designed to fully trap and micromanipulate single bubbles in 3D, we compare the magnitude of nonspherical deformation for bubbles in contact with a wall and free-floating bubbles. We show that in the studied range of acoustic pressures, the growth of surface modes saturates at a level far below bubble breakage. We discuss the potential medical relevance of these nonspherical oscillations, in relation with possible subharmonic acoustic emission.

Another new optical characterization is discussed in Ch. 6. The method consists of insonifying individual bubbles with a chirp of increasing or decreasing frequency. The bubble response is analyzed in two ways: one method consists of power spectrum analysis, and the other method analyzes the phase difference between driving an response signals. The new methods are compared with the microbubble spectroscopy method, and give identical values for the eigenfrequency (or peak frequency for high amplitude oscillations). With all three methods, a decrease in peak frequency as function of increasing oscillation amplitude was reported, which agrees with an analytical analysis.

Furthermore, in Sec. 6.5, the bubble response difference on a chirp up sweep and a chirp down sweep was studied. It can be used as a new contrast imaging approach based on chirps, and it was termed chirp reversal contrast imaging. Simulations and optical observations with the Brandaris camera were carried out to explore the potential of the chirp reversal approach in detecting microbubbles. Simulations showed that for larger bubbles (> 2.3 μm), significant differences occur between upsweep chirp response and down sweep response around 1.7 MHz transmit frequency. Optical observations confirmed these results. From

the optical radius-time curves, the larger bubbles showed different dynamics when up sweep or down sweep frequencies were used in transmission. Up sweep excitation chirps produce highly damped responses with large amplitude excursions whereas the response to down sweep chirps showed pronounced resonance behavior with smaller amplitudes. Smaller bubbles ($< 2.3\ \mu$m) appear to be less sensitive to frequency sweep at 1.7 MHz transmit frequency. However, driven at a higher center frequency, smaller bubbles tend to be more sensitive. Experimental and theoretical data confirm that chirp reversal is feasible and can be used to detect contrast microbubbles and to improve the contrast to tissue ratio in imaging.

Samenvatting

De ‘Brandaris 128’ hogesnelheidscamera is ontworpen en gebouwd om de dynamica van individuele oscillerende contrastvloeistof–microbellen onder invloed van ultrageluid te bestuderen. In dit proefschrift rapporteren we onze bevindingen.

Allereerst wordt in hoofdstuk 2 een nieuw model geïntroduceerd dat rekening houdt met de fysische eigenschappen van een lipide coating van een contrastbel. Er zijn drie parameters die de eigenschappen van de schil beschrijven: een knik–straal, de compressibiliteit van de schil en een kritieke oppervlaktespanning van de schil. Het model laat niet–lineair gedrag zien bij oscillaties met grote amplitude, ‘compression–only’ genoemd, dat wordt veroorzaakt door het knikken van de lipide monolaag. Deze voorspelling wordt bevestigd door experimentele opnames met de Brandaris camera van veel miljoenen beeldjes per seconde. Het effect van veroudering, of het resultaat van herhaalde akoestische drukpulsen op bellen, wordt ook voorspeld door het model. Verder corrigeert het model een fout in de elasticiteitsterm van de schil die voorheen gebruikt werd in de dynamische vergelijking voor gecoate bellen. Het breken van de bel is gemodelleerd door een kritieke oppervlaktespanning van de schil, waarboven gas direct in contact komt met water.

Een nieuwe optische karakterisatie van het gedrag van individuele ultrageluid contrastbellen wordt gepresenteerd in hoofdstuk 3. De methode bestaat uit het opeenvolgend aanstralen van individuele bellen met verschillende frequenties en het opnemen van de reactie van de bel in filmpjes met opnamesnelheden tot 25 miljoen beeldjes per seconde met de Brandaris hogesnelheidscamera. De camera wordt gebruikt in een gesegmenteerde modus. De methode, die ‘microbubble spectroscopy’ genoemd is, maakt het mogelijk een resonantiecurve te maken in een enkele opname. De data worden geanalyseerd met een gelineariseerd model voor gecoate bellen. De resultaten bevestigen de significante invloed van de schil op de beldynamica: de elasticiteit van de schil verhoogt de resonantiefrequentie met ongeveer 50% en de viscositeit van de schil is verantwoordelijk voor ongeveer 70% van de totale demping. De verkregen waarde voor de elasticiteit van de schil komt kwantitatief overeen met eerder gerapporteerde waarden. De viscositeit van de schil neemt significant toe met de straal, wat een nieuw niet–lineair gedrag van de fosfolipide schil onthult.

Bellen die ultrasoon aangedreven worden in de buurt van hun resonantiefrequentie kunnen vorm–instabiel worden door een para-

metrische instabiliteit. We rapporteren optische opnames met de Brandaris camera van vormoscillaties (mode n = 2 tot en met 6) van individuele contrastbellen (in hoofdstuk 5) en van micrometerformaat luchtbellen (in hoofdstuk 4) voor een bereik van akoestische drukken. Voor de luchtbellen is gevonden dat het geobserveerde mode nummer n lineair gerelateerd is aan de ruststraal van de bel. Boven een kritieke drukamplitude, welke minimaal is op de volumetrische resonantie van de bel, is het mode nummer n onafhankelijk van de akoestische drukamplitude. De vormoscillaties van de microbellen zijn ook numeriek geanalyseerd door een kleine niet–sferische lineaire verstoring te introduceren in een aangepaste Rayleigh–Plesset vergelijking. Het model bevat een thermisch dempingsmechanisme, dat warmte– en massatransport in de dunne grenslaag tussen bel en water beschrijft. Een parametrische instabiliteit is inderdaad verantwoordelijk voor de vormoscillaties en het nieuwe model beschrijft de experimentele observaties zeer gedetailleerd.

Voor de contrastbellen definiëren we een enkele dimensieloze deformatieparameter en kwantificeren we de amplitude van de niet–sferische deformatie als een functie van de belstraal (tussen 1.5 en 5 μm) en van akoestische druk (tot en met 400 kPa). We laten zien dat de oppervlaktemodes zich bij voorkeur ontwikkelen bij een belstraal die correspondeert met de volumetrische resonantiestraal. Met behulp van een optisch pincet, ontworpen om individuele bellen in 3D te vangen en te manipuleren, vergelijken we de grootte van de niet–sferische deformatie voor bellen in contact met de wand en voor vrij zwevende bellen. We laten zien dat in het bestudeerde bereik van akoestische drukken de groei van oppervlaktemodes verzadigt op een niveau ver onder beldestructie. We bediscussiëren de potentiële medische relevantie van de niet–sferische oscillaties in relatie met de mogelijke subharmonische akoestische emissie.

Een andere optische karakterisatie wordt bediscussieerd in hoofdstuk 6. De methode bestaat uit het aanstralen van individuele bellen met een ‘chirp’ van oplopende of aflopende frequenties. De reactie van de bel wordt geanalyseerd op twee manieren: de ene methode bestaat uit de analyse van het vermogensspectrum en de andere manier analyseert het faseverschil tussen de aandrijvende en de resulterende signalen. De nieuwe methodes worden vergeleken met de ‘microbubble spectroscopy’–methode en geven identieke waardes voor de eigenfrequentie (of piekfrequentie voor oscillaties met grote amplitude). Met alle drie methodes is een afname in piekfrequentie als functie van oscillatieamplitude gerapporteerd, die overeenkomt met een

analytische afleiding.

Verder wordt in sectie 6.5 het verschil in belreactie op een oplopende en een aflopende ‘chirp’ bestudeerd. Deze ‘chirps’ kunnen gebruikt worden bij een nieuwe beeldvormingsmethode met behulp van contrastvloeistoffen en de methode is ‘chirp reversal contrast imaging’ genoemd. Simulaties en optische observaties met de Brandaris camera zijn uitgevoerd om het potentieel van de ‘chirp reversal’–methode te onderzoeken. Simulaties laten zien dat voor grotere bellen (> 2.3 μm) significante verschillen ontstaan tussen belreacties op oplopende en aflopende ‘chirps’ bij ultrageluid van 1.7 MHz. Optische observaties bevestigen deze resultaten. In de optische straal–tijd curves laten de grote bellen een andere reactie zien wanneer akoestisch oplopende of aflopende frequenties gebruikt worden. Oplopende akoestische ‘chirps’ produceren zeer gedempte belreacties met grote amplitude, terwijl de reactie op aflopende akoestische ‘chirps’ juist resonantiegedrag met kleine amplitudes laat zien. Kleinere bellen (< 2.3 μm) lijken minder gevoelig te zijn bij een akoestische ‘chirp’. Echter, bij een hogere centrumfrequentie zijn kleinere bellen gevoeliger. Experimentele en theoretische data bevestigen dat ‘chirp reversal’ uitvoerbaar is en gebruikt kan worden om contrastbellen te detecteren en om de verhouding van contrast tot weefsel in beeldvorming te vergroten.

Acknowledgements

The research described in this thesis is part of the research program of the “Stichting voor Fundamenteel Onderzoek der Materie” (FOM), which is financially supported by the “Nederlandse Organisatie voor Wetenschappelijk Onderzoek” (NWO). It was carried out at the Physics of Fluids research group of the faculty of Science and Technology at the University of Twente. I gratefully acknowledge the support of these institutions. I also acknowledge the Interuniversity Cardiology Institute of the Netherlands (ICIN) and the Senter Novem agency of the Dutch Ministry of Economic Affairs for their financial support, and Bracco Research S.A. (Geneva, Switzerland) for supplying contrast agents SonoVue® and BR-14.

In the last four years that I performed research as a PhD student, I worked together with many people. The contents of this thesis have been shaped by the work and input of these people. I want to thank all the people that have helped me during this period. I would like thank a few people in particular.

First of all, I would like to thank my promotor prof. dr. Detlef Lohse, my promotor prof. dr. ir. Nico de Jong, and my assistant promotor dr. Michel Versluis. Both during theory discussions in the office, as well as during experiments in the lab, I have learned many things from all of you.

The help of the technicians Gert-Wim Bruggert, Martin Bos, (late) Henni Scholten en Bas Benschop is gratefully acknowledged. I would like to thank Joanita Leferink for administrative help in the last years. From the Rotterdam group, I thank Leo Bekkering, Jan Honkoop and Cees Pakvis for their technical support, and Cees also for the many hours of support in operating the Brandaris camera in Rotterdam. Also from the Rotterdam group, I would like to thank Riekje Daane and Mieke Pruijsten for administrative work.

I would also like to thank the many co-authors of the articles for their contributions to this thesis. They are, in no particular order, Benjamin Dollet, Philippe Marmottant, Marcia Emmer, Sascha Hilgenfeldt, Marco Voormolen, Chien Ting Chin, Ayache Bouakaz, Michel Versluis, Detlef Lohse, Nico de Jong, Peggy Palanchon, Dave Goertz, Ivo Heitman, and Anthony Novell. Also thanks to Joris Timmermans, François Graner, Wouter den Otter, Jeroen Sijl, Marlies Overvelde, Rik Vos and Leen van Wijngaarden for involvement in the coming about of the articles.

Also many thanks go to the medical bubble people in the group for creative solutions for experimental or theoretical problems and for fruitful discussions. They are Jeroen Sijl, Benjamin Dollet, Marlies Overvelde, Wim van Hoeve, Valeria Garbin, Timo Rozendal, Tamara van Weperen, Erik Gelderblom and Jan van Veldhuizen, and from the Rotterdam group I would like to thank Marcia Emmer, Annemieke van Wamel, Dave Goertz, Martijn Frijlink and Rik Vos.

Then I would like to place some special words for my (former) office mates. They are Ramon van den Berg, Hanneke Bluemink, Henk Jan van Gerner en Marlies Overvelde. Not only did we have many scientific discussions, we helped each other with Matlab problems, and we also discussed personal issues, often with many laughs. Thank you for the good times!

I would like to thank all of my colleagues of the Physics of Fluids group. We had often nice discussions and fun during coffee breaks and other social events.

I also want to thank my friends, during berenburg evenings, pubquiz evenings, korfball activities, or other social events for the great fun and occasional relaxation.

I want to thank my paranimfs Ramon van den Berg and Sjoerd Ligthart for their support, both during the time as PhD students, as during my defense.

Special thanks go to my parents for the opportunities they have always given me. For this reason, this thesis is as much their effort as it is mine. I also thank my sister and her boyfriend Annerike and Richard, my parents-in-law Henk and Hannie, and my good friend Ramon for their support and involvement.

Finally, I would like to thank my girlfriend Hester for love and support. The last few years were demanding for you, with a job in Gouda and a home in Enschede. I cannot thank you enough for the exhausting weekly travels between both places. Hopefully this changes soon!

Sander van der Meer
July 2007

About the author

Sander Martijn van der Meer was born on January 11th, 1978 in Assen, The Netherlands. He graduated from high school 'Dr. Nassau College' in Assen in 1996, and started that same year studying Applied Physics at the University of Twente in Enschede. With interest in astrophysics, the focus of the study changed to biophysics, and later changed to fluid dynamics. During his study, he co-organized a study tour to Scandinavia, he was the vice chairman of the korfball union Vakgericht, and was teaching assistant in many experimental physics courses. In 2002 he went for a four month internship to the group of prof. Wolfgang Losert at the University of Maryland, USA. In 2003 he graduated on 'Mono-disperse microbubbling – Instabilities in coflowing gas-liquid jets' in the Physics of Fluids group of prof. dr. Detlef Lohse. He continued in the Physics of Fluids group to do his PhD research in collaboration with dr. Michel Versluis, prof. dr. ir. Nico de Jong and prof. dr. Detlef Lohse.